Machine diagnostics based on blind signal extraction and novelty detection using non-stationary vibration signals

Oscar Cardona Morales

Universidad Nacional de Colombia
Faculty of Engineering and Architecture
Department of Electrical, Electronic and Computing Engineering
Manizales, Colombia
2016

Machine diagnostics based on blind signal extraction and novelty detection using non-stationary vibration signals

Oscar Cardona Morales

Thesis presented as a partial request for the degree of:
Doctor of Engineering - Automatics

Advisor:
Ph.D. César Germán Castellanos Domínguez

Research subject:
Machine Diagnostics and Vibration Analysis
Research Group:
Signal Processing and Recognition Group

Universidad Nacional de Colombia
Faculty of Engineering and Architecture
Department of Electrical, Electronic and Computing Engineering
Manizales, Colombia
2016

Diagnóstico de máquina basado en extracción de señales ocultas y detección de atípicos usando señales de vibraciones no estacionarias

Oscar Cardona Morales

Tesis presentada como requisito parcial para el grado de:
Doctor en Ingeniería - Autnomática

Director:
Ph.D. César Germán Castellanos Domínguez

Tema de Investigación:
Diagnóstico de máquina y análisis de vibraciones
Grupo de Investigación:
Control y Procesamiento Digital de Señales

Universidad Nacional de Colombia
Facultad de Ingeniería y Arquitectura
Departamento de Ingeniería Eléctrica, Electrónica y Computación
Manizales, Colombia
2016

To my sweet children and my wife...

Acknowledgements

God, thanks by everything that You give me, the effort and dedication to complete this work. An special thanks goes out to my parents, my sister and my family (wife and sons) in general for the support and love that they give me in every moment of my life. I would like to express my gratitude to the Prof. Germán Castellanos-Domínguez for his orientation during this research. Besides, I would like to thank all the Signal Processing and Recognition Group (SPRG) of the Universidad Nacional de Colombia sede Manizales for their suggestions and hours of academic discussion.
Furthermore, thank all the members of the Vibration and Acoustic Laboratory (LVA) from INSA de Lyon, Lyon-France, for their hospitality and help, and specially to Professor Jérôme Antoni by the opportunity to visit and to learn in this great research group. Finally, I recognize that this research would not have been possible without the financial assistance of the Ph.D. studies scholarship: Programa Nacional de Formación de Investigadores - Estudio de Doctorado en Colombia - 2011, Promoción 528. Moreover, some of the results of this research were supported by the project: Sistema autónomo de monitoreo de vibraciones mecánicas para diagnóstico de fallas no estacionarias en máquinas rotativas.

Agradecimientos

Agradezco a Dios por todo lo que me ha dado, la esfuerzo y dedicación para completar este trabajo. Un agradecimiento muy especial a mis padres, mi hermana y mi familia (esposa e hijos) en general por el apoyo moral y afectivo que me dieron en cada momento de mi vida. Quiero expresar my gratitud al Profesor Germán Castellanos Domínguez por su orientación y apoyo durante la investigación. Asimismo, a mis compañeros del grupo de Control y Procesamiento Digital de Señales de la Universidad Nacional de Colombia sede Manizales por todas sus sugerencias y horas de discusión académica.
También, agradezco a todos los miembros del Laboratorio de Vibración y Acústica de INSA de Lyon (Francia), por su hospitalidad y ayuda, y en especial, al Profesor Jérôme Antoni por la oportunidad de compartir y aprender en ese gran grupo de investigación. Finalmente, esta tesis, y la investigación desarrollada en ella, no habría sido posible sin el apoyo financiero del Programa Nacional de Formación de Investigadores - Estudio de Doctorado en Colombia - 2011, Promoción 528 de Colciencias - Colfuturo. Asimismo, a la Universidad Nacional de Colombia sede Manizales por su programa de apoyo a tesis de posgrado (2014-2, 2015-1), y a los compañeros de la Universidad Católica de Manizales por su compresión y apoyo durante la terminación de mis estudios doctorales. Por último, quiero dejar claro

que parte de los resultados en ésta investigación fueron obtenidos en el marco del proyecto de investigación titulado “ *Sistema autónomo de monitoreo de vibraciones mecánicas para diagnóstico de fallas no estacionarias en máquinas rotativas*”.

Abstract

Nowadays, condition monitoring of rotating machinery is becoming increasingly important for the industry because it allows reducing accidental damages and improving the machine performance at the same time. This tool, also called *Condition-based Maintenance* relies on the adequate evaluation of the machine health or state, employing a set of measurements as mechanical vibration signals. Nevertheless, most of the real-world machinery operates unique pieces, which are not suitable for inducing faults, making unfeasible to collect useful data on damaged conditions. Furthermore, in many cases, the operating conditions of the machine are governed by speed or load changes, which makes difficult the traditional analysis based on the ISO standards, and hides relevant information of the machine health.

In that sense, this document present a machine diagnostic methodology, based on the analysis of non-stationary vibration signals, which includes the detection, isolation, and identification of the possible faults. Particularly, the proposed methodology has the same stages but in an order different. Firstly, an order tracking (OT) model is proposed to decomposes the signal into a set of narrow-band spectral components that capture information associated with the operating conditions. Besides, the OT model provides the possibility also to extract the reference shaft speed when that measure is unavailable. Secondly, a novel methodology for fault detection, called *frequency-located fault detection*, based on novelty detection techniques that use one-class classifiers (OCC) to describe the normal machine performance. Here, the obtained order components, obtained using the OT model, are used as pseudo-observations of the vibration signal and a classification scheme is applied to determine if any new instance corresponds with an outlier. Therefore, this step makes a decision for each order component, assigning to each one a label either target or outlier. The advantage in this step is centered in the fact that allow determining the frequency range where the fault arises, reducing the search time and giving useful information to the machine operator. Finally, the cyclostationary properties of the order components are analyzed and inspected to identify the type of faults, which in this case are related with bearing failures. With the proposed methodologies to machine diagnostic, it is possible detecting effectively that the fault exists, taking into complex account scenarios where the operating conditions are time-varying.

Several experiments are discussed, lasting from laboratory test rigs to case studies such as ship driveline, wind turbine, gearbox and diesel engine, where the proposed OT model was tested estimating the instantaneous speed. Another significant finding is defined by the cyclic properties that the order components present because the model may be used as a preprocessing tool that contributes to separate stationary and cyclostationary processes whenever the operating condition of the machine be constant. In conclusion, the proposed methodology for machine diagnostic based on the OT model to extract blind components and to detect outlier behaviors is a promising tool in condition monitoring.

Keywords: Order Tracking, Blind Signal Extraction, Novelty Detection, Non-stationary vibration Signals

Resumen

Hoy en día el monitoreo de condición de maquinaria rotativa ha comenzado a ser un tema importante para la industria porque permite al mismo tiempo reducir daños accidentales y mejorar el rendimiento de las máquinas. Ésta herramienta, conocida también como *Mantenimiento basado en condición* se basa en la evaluación adecuada de la salud de la maquinaria, empleando una serie de mediciones como vibraciones mecánicas. No obstante, la gran mayoría de máquinas en ambientes industriales reales utilizan piezas únicas, por lo cual no es posible inducir o simular fallas, haciendo infactible coleccionar datos útiles de la máquina bajo condiciones de daño. Además, en muchos casos, las condiciones de operación de la máquina se rigen depedendiendo de los cambios de la velocidad o carga, lo cual incrementa la dificultad del análisis tradicional basado en normas ISO, y oculta información relevante de la salud de máquina.

Bajo esa perspectiva, este documento presenta una metodología de diagnóstico de maquinaria basada en el análisis de señales de vibración no estacionarias, incluyendo las etapas de detección, separación e identificación de las posibles fallas. Particularmente, la metodología propuesta esta compuesta por las mismas etapas que cualquier procedimiento de diagnóstico de fallas pero en un orden diferente. Primero, se propone un modelo de seguimiento de orden (*Order Tracking - OT* en inglés) para descomponer la señal en un conjunto de componentes espectrales de banda angosta, los cuales capturan la información asociada con las condiciones de operación. En ese sentido, el modelo OT propuesto brinda la posibilidad de extraer tanto la velocidad del eje de referencia cuando ésta medida no es disponible. Segundo, se propone una novedosa metodología para detección de fallas, llamada *detección de fallas con localización en frecuencia*, la cual se basa en técnicas de detección de atípicos (*Novelty Detection* en inglés) y usa clasificadores de una clase para describir el rendimiento normal de la máquina. La metodología propuesta utiliza los componentes de orden, obtenidos usando el modelo OT, como nuevas pseudo-observaciones de la señal de vibración, y se emplea un esquema de clasificación, como etapa posterior, con el fin de determinar si cualquiera de los nuevas observaciones puede ser catalogada como un atípico. En consecuencia, a cada componente de orden se le asigna una etiqueta que puede tomar dos valores *normal* o *atípico*. La ventaja de esta metodología se centra en el hecho que permite determinar el rango de frecuencia donde se encuenta una falla, reduciendo el tiempo de búsqueda y brindando información útil al personal de mantenimiento, que en muchos casos no tiene conocimientos especializados para este tipo de análisis. Finalmente, se analizan las propiedades cicloestacionarias de los componentes de orden y, mediante inspección visual, se identifican distintos tipos de falla

relacionados con defectos en rodamientos. Con el uso de la metodología propuesta es posible detectar de una forma efectiva que y cuales fallas puede estar experimentado la máquina, considerando escenarios complejos donde las condiciones de operación son cambiantes en a través del tiempo.
Varios experimentos son discutidos, desde bancos de prueba de laboratorio hasta estudios de caso tales como la línea de propulsión de un barco, turbinas de viento, sistemas de engranajes y motores de combustión interna, donde el modelo OT propuesto fue probado para estimar la velocidad instantánea. Otro hallazgo significativo se basa en la definición de las propiedades cíclicas que tienen los componentes de orden, ya que ésto abre la posibilidad de emplear el modelo propuesto como una técnica de descomposición para separar componentes estacionarias y cicloestacionarios cuando las condiciones de operación de la máquina son constantes. En conclusión, la metodología propuesta es una herramienta prometedora en el área de monitoreo de condición de máquinas rotativas.

Palabras claves: Seguimiento de orden, Extracción de señales ocultas, Detección de atípicos, Señales de vibración no estacionarias

Contents

List of Figures

List of Tables

1 Introduction

1.1 Motivation

Technological developments had represented a challenge for the industry to improve the machinery and the productive systems, motivating an increment in their demand from community searching a stable economy and a reliable plant. Besides, to decrease the environment and human risks. Therefore, the importance of maintenance area has increased because it allows holding the system health and its availability. The continued progress in sensing capabilities together with the necessity of monitoring processes have changed the industry paradigm, where the companies are migrating from traditional preventive maintenance strategies to conservative maintenance tasks, and they are incorporating predictive maintenance concepts, which are carried out only when these are required.

In this context, speaking about machine fault diagnostic turns relevant, and it can be defined as the procedure of mapping the information obtained from a measurement space to a feature space. This mapping process is also called *Feature extraction*. Traditionally, feature extraction oriented to pattern recognition is done manually with statistic indicators as root mean square value, or auxiliary graphical tools such as power and phase spectrum graphs, cepstrum graph, AR spectrum graph, spectrogram, wavelet scalogram, wavelet phase graph, etc. However, manual pattern recognition requires expertise in the particular area of the diagnostic application. Thus, highly trained and skilled personnel is needed. Therefore, automatic pattern recognition is highly desirable, and can be achieved by classification of signals based on the information or features extracted from mechanical vibration signals. It is worth noting that vibration analysis is attractive in the industry due to its low cost and the acceptable precision that it can reach using this technical tool, in comparison with techniques as acoustic emission and thermography. In consequence, this work covers only the issue related to the digital processing of vibration signals.

In Colombia, the industrial sector had seen the necessity of implementing predictive maintenance programs, aiming to optimize the performance and the useful lifetime of their machines. Hence, the vibration analysis as a tool for machine diagnostics has generated all kind of expectations, because it has a high profitability w.r.t the cost/benefit relationship. Therefore, the development of a methodology in machine diagnostics allows increasing the predictive and preventive maintenance in Colombian industry, entailing a major competitively in their products and processes. Furthermore, the Signal Processing and Recognition

Group focuses its activity on the research and development of stochastic characterization, training, and recognition systems, which are applied to machine diagnostics using the vibration analysis. Additionally, this doctoral work is framed into the research project titled "*Sistema autónomo de monitoreo de vibraciones mecánicas para diagnóstico de fallas no estacionarias en máquinas rotativas*", which was endorsed by Colciencias.

1.2 Problem statement

Condition-based monitoring recommends maintenance decisions grounded on the information collected from the machine, also called *Diagnostics*, which deals with fault detection, isolation, and identification whenever it occurs. Fault detection is a task to indicate whether something is going wrong in the monitored system; fault isolation locates the component that is faulty; fault identification determines the nature of the damage whenever it is detected (Jardine et al., 2006). The most used technique in diagnostics is vibration analysis because it allows to find the different sources, either internal or external, which excite the machine. Thereby, it is possible to identify the fault source that generates the abnormal state of the machine. However, several problems involve the identification of the source, especially, when the machine behavior is dynamic, i.e. there are changes of load and/or speed in the system, causing non-stationary vibration signals.

Those non-stationary sources are then analyzed by several methods to detect a possible change in their dynamics, which is reflected in the original measurements, yet it is tough to identify that change (Popescu, 2010). For this reason, it is necessary to estimate or measure the fundamental frequency that governs the dynamic behavior of the machine, giving a detailed identification of speed changes, and analyzing the impact of those changes on the vibration signals (Barszcz and Randall, 2009). Those effects are known as *transients*, and its analysis has always been a crucial problem for localized fault detection. In that sense, the principal aim of transient feature analysis is to identify its model and parameters (frequency, damping ratio and time index), as well as the time interval or frequency band (i.e. the period between transients) (Wang et al., 2011a). In practical applications, however, the transient model and frequency parameter may not be so entirely accurate for identifying the period. Therefore, the frequency band selection problem is understood as the selection of optimal center frequency or cyclic frequency and its bandwidth dyad. The practical concern in machine diagnostics is that any of these two parameters is hardly known a priori. Furthermore, in many cases, the sought impulses are masked by a sharp noise or other signal components excited during normal operation (Barszcz and JabŁoński, 2011).

If there exists a priori knowledge about the cyclic frequency, a set of blind sources could be separated into cyclostationary, periodic and random sources. However, conventional blind source separation (BSS) algorithms rely on assumptions, which often do not fit into observations in reality. Hence, there is an urge to address the robustness issues such as separation

of sources when the number of sources is not known a priori, the sources are not statistically independent, the mixing system is time varying or non-stationary, and the mixture is nonlinear or convolutive (Antoni, 2005, 2009). For instance, most of the BSS models developed are based on the assumption of a stationary mixing system. But in practice, there are many circumstances where this assumption is violated, due to non-stationary behavior caused by load and speed changes (Das et al., 2009, 2010). Thereby, it is necessary to alleviate some of the difficulties of BSS, such as convolutive mixtures, an insufficient number of collected mixtures and an unknown number of sources. Therefore, the problem is focused to blind source extraction, where a blind component is sought assuming the knowledge of the part of the machine that is going to fail (Jing and Meng, 2009). Nonetheless, those assumptions cannot be applied to real applications because they require expertise in the particular area of the diagnostic application. Moreover, a single machine component may represent multiple signal sources, reflected by multiple faults of different characteristics. Then, using a dedicated sensor and an algorithm for each and every such failure is of course not viable both technically and economically. It is, therefore, highly desirable to develop an efficient method for simultaneous detection of multiple transient faults and blind signals of a single or multiple neighboring machine components based on a single- or multi-channel signals (Wang and Liang, 2012).

It is worth noting that distinguishing the different blind signals only gives a partial solution to the diagnostic problem, because it allows identifying where may be the fault, but it does not say if the defect exists, especially, in actual environments, where the faulty cases are not available. Therefore, it is necessary to render an additional stage for fault detection, known as *novelty detection*. In most of the cases, the input dataset holds unbalance of the faulty/undamaged classes (states of the machine), since the recordings of the damaged machine are not available and the amount of available data characterizing the different states of the machine are very low. In consequence, the application of conventional classification techniques can not be considered (McBain and Timusk, 2009; Xiao et al., 2013). Likewise, to reflect practical constraints; usually, there is only a small available dataset for the learning task, at the constant regime and with no mechanical model. Indeed, in the field of large and complex rotating machines such as turbofans, many defects can not be modeled nor anticipated, and recordings of faults are unavailable (Hazan et al., 2012). In the event, however, that the distribution of available data among classes is unbalanced, the ability of conventional classification techniques to distinguish undamaged from any damage is limited. So, in machinery monitoring, this unbalance is particularly potent since the data that describe the fault conditions are often non-existent, and their measurement would require damage equipment, a costly or wholly unacceptable operational consideration (McBain and Timusk, 2011).

1.3 A brief literature review

In the field of machine diagnostic problem, several authors had studied different points of view such as the non-stationary behavior identification of the machine governed by variable speed and/or load and its associated individual components, usually so called *order tracking*). The extraction of blind components from the vibration signal that characterizes fault conditions, and the machine health state description when just undamaged recordings are available (*novelty detection*). Although each issue looks like separated tasks, every technique is driven to the same problem, and the works related here were the motivation at the beginning of this doctoral work.

1.3.1 Order tracking

In this regard, techniques grounded on order tracking (OT) have been devoted to obtaining the fundamental component features of the reference shaft speed (called *basic order*) and capturing the dynamics of the measured vibration signals. The OT technique has shown to be useful in the analysis of non-stationary vibration signals, condition monitoring, and fault diagnosis (Bai et al., 2005). Moreover, it allows to identify the rotation speed and their spectral/order components, being both fundamental to describe the machine state as well as its conforming mechanisms under changing load and speed regimes, for instance, start-up and coast-down of the machine (Guo et al., 2006; Pan and Lin, 2006).

OT is used in the literature for two specific tasks, on one hand there are the techniques related with the estimation of the instantaneous angular speed (IAS), where the pattern that governs the machine dynamic is extracted from the vibration signal. This fact is specially useful when the speed is not measured by tachometer or speed sensors. In that regard, the IAS could be estimated from non-parametric or parametric representations. In the former case, it could be found approaches based on time-frequency representations such as Gabor transform (Zhao et al., 2008) and Short-Time Fourier Transform (Guo et al., 2006; Gao et al., 2006; Zimroz et al., 2011; Leclère et al., 2016), which in many cases fitting the extracted IAS by a least squares method. Another approaches are based on time-scale transformations such as scale transform (Combet and Zimroz, 2009) and wavelet transform (Gryllias and Antoniadis, 2013). In the case of parametric representations are found approaches based on state space models that are mainly solved by recursive algorithms such as the Extended Kalman Filtering (EKF) (Scala and Bitmead, 1994; Bittanti and Saravesi, 2000; Zhang et al., 2008), and the eigenvalue parametric computation (Rodopoulos et al., 2014). In spite of these methods achieve satisfactory results, the fitting of a parametric model of the vibration signal could provide more information about the spectral components in the signal, and hence, similar approaches use the EKF to extract both IAS and order/spectral components (Alves and Coelho, 2010; Hajimolahoseini et al., 2012).

On the other hand, there are the approaches that use the speed information to extract a sin-

gular or multiple order components. In that sense, based on a suggested estimation strategy using Kalman filtering in Bai et al. (2005), its improved version with increased precision, termed *Vold-Kalman filtering* (VKF_OT), is employed in Pan and Lin (2006); Pan and Wu (2007); Stephens and Vold (2014). However, either parametric estimation approach requires for measuring the shaft speed, which makes the order analysis still complicated since tracking performance is subject to the synchronization process between the vibration signal and its reference speed. Also, the shaft speed measurement implies installing additional equipment near the machine, which in not all situations may be feasible. Other approaches proposed in Cardona-Morales et al. (2011) and Wang and Heyns (2011), use a combined model for OT. In the former case, an oscillatory model is employed together to Extended Kalman Filter and the latter case uses the VKF-OT together to Empirical Mode Decomposition for separating the non-stationary and stationary components. However, the estimation of the number of order components is still an open issue, because it requires a huge a priori knowledge about the machine, moreover, it is sensible enough to the noise environment. Nonetheless, if a priori information about the machine is available, it is possible to carry out an order-angle transformation that compensates the speed fluctuations, obtaining a signal map where the majority of components governed by the reference shaft speed are stationary. The most commonly used techniques is called computed order tracking (COT) (Fyfe and Munck, 1997), which performs a resampling of the signal according with the angle information. Nonetheless, another techniques based on resampling are synchronous averaging used in Renaudin et al. (2010); Borghesani et al. (2012, 2013), and a improved version termed moving synchronous averaging approach is presented in Leclère and Hamzaoui (2014). Those approaches have showed interesting results identifying rolling element bering faults, and its application to other mechanisms is increasing.

1.3.2 Novelty detection

One-class classification (OCC) techniques have been used, to determine when the state of machine ceases to be normal and when the first symptoms of damage appear. For instance, Tax and Duin (2004) shows a comparison between several standard one-class classifiers such as the normal distribution classifier, the k-nearest neighbor (k-NN) classifier and an algorithm called support-vector data description (SVDD). Those one-class classifiers are trained and tested employing vibration signals at different constant speeds using the set of features extracted with the statistical methods. However, the data description performance is low. Therefore, several authors have proposed different methodologies oriented to improve the performance of OCC; for instance, Zhang et al. (2009) suggested the use of weighted SVDD, McBain and Timusk (2009) employed a characterization using average-moving model, Pan et al. (2010) used a wavelet packet transform and McBain and Timusk (2011) reduced the subspace on classification using principal component analysis. Those methodologies seg-

ment the non-stationary vibration signal piecewise and estimate statistical features of each part. Those approaches reach a high classification performance but, in some practical cases, the signal segmentation entails loss of information either in time or frequency (Bartkowiak and Zimroz, 2011).

Also, for some data set, if the parameters are set inappropriately, the fault positive rates of SVDD models will be too large (Tax and Juszczak, 2002). Hoffmann (2007) introduced the conventional Kernel Principal Component Analysis (KPCA) into novelty detection. This method performs well and involves only the linear algebra. But it is not robust to outliers in the normal samples due to the inherent properties of L2 norm. When non-uniform distributed outliers contaminate the undamaged instances, the loading vectors found by the conventional KPCA will deviate a lot from the real loading vectors, leading to the downgrade of the performance. Xiao et al. (2013) introduced the L1 norm into KPCA problem, taking the advantage of the robustness of L1 norm to outliers, to strengthen the immunity of the model to outliers, and therefore to improve the detection performance. Nonetheless, the L1-KPCA algorithm requires to reach the global maximum point and then enable the detection model to be more accurate. Furthermore, the way of choosing decision thresholds is still an open issue.

1.3.3 Blind signal extraction - BSE

In this field the issue of inferring the nature of unknown endogenous sources from exogenous measurements has always been a major concern. The works in this domain have already proved that BSS provides new solutions for vibration and noise analysis.

Regarding the BSS problem, several methods for instantaneous and convolutive mixtures are used. In the former case, the most popular method is independent component analysis (ICA), which assumes a statistical independence between the sources (Hyvärinen and Oja, 2000) and it is commonly employed in communication and biomedical applications. Especially for mechanical systems, Yang and Nagarajaiah (2014) and Wang et al. (2011b) have been used ICA for separating an output that is statistically independent of other sources, both structural and rolling element bearing damages, respectively. On the contrary, the algorithm Nguyen Thi-Jutten allows the separation of the contributions of two coupled machine assuming a convolutive mixture (Gelle et al., 2000; Ypma et al., 2002). Another method is presented in Peled et al. (2005), where a kurtosis-based blind deconvolution separation method is used to bearing diagnostics. Since the machine environment is noisy, in Servière and Fabry (2004) is presented a “robust-to-noise” technique for the separation of rotating machine signals, in the context of spatially correlated noise. In the concrete case, they use a whitening matrix computed either by Principal Component Analysis (PCA) or spectral arrays of delayed observations, to improve the signal-to-noise rate, and then applying the BSS algorithm termed JADE (Joint Approximate Diagonalization of Eigen-matrices) as also presented in Servière

and Fabry (2005). This algorithm is also used in Popescu (2010) to separate the sources and detect the change in the vibration level for each one, yet the results are not consistent in the sense that the method depends on an appropriate whitening process.

Nonetheless, when BSS is used in mechanical signals, which are typically characterized by an excessive complexity, it faces some difficulties which severely hinder its feasibility, such as a mixture of vibrations of the convolutive type, an unknown number of the individual sources in the mixture, among others (Antoni, 2005). Therefore, a new concept so-called *Blind Component Extraction* or *Blind Signal Extraction* (BSE) was introduced by the same author to compensate the BSS drawbacks. The major difference between BSE and BSS is that the former identifies the different system responses (components) excited by the different sources rather than seeking the sources themselves, whereas the latter blindly deconvolutes the collected signals and identifies the sources. In that sense, the BSE is focused on separating the distinct processes present in the vibration signal that exhibits a behavior either periodic, periodically correlated (cyclostationary) or random. The method proposed by Bonnardot et al. (2005) addresses the issue of extracting the pure second-order cyclostationary part of a signal, exploiting its spectral redundancy. Randall and Antoni (2011) summarizes some methods, such as an autoregressive model, adaptive noise cancellation, self-adaptive noise cancellation, discrete separation and time synchronous averaging, that could remove the periodic components prior to spectral kurtosis analysis (Antoni, 2006) and cyclic spectral analysis (Antoni, 2009), for the non-stationary transient components. In the case of a simulated signal, Tan et al. (2006) illustrates the effectiveness of using an eigenvector algorithm (EVA) to extract bearing-fault signals from periodic sinusoidal noises. To further explore the performance of the EVA and its application to a real industrial case, Tse et al. (2007) uses the EVA and a generalized EVA to recover the bearing fault signal from a signal mixture containing an eccentric rotor fault and a bearing fault. The same author includes in Wang and Tse (2012) a second strategy based on Averaged Regression filtering to remove the influence of the periodic components before implementing EVA. Finally, the cyclic spectral analysis is performed to identify the cyclic frequency (the modulating frequency or bearing fault characteristic frequency) to diagnose the bearing failure.

1.4 Objectives

1.4.1 General objective

Develop a methodology for machine diagnostics that allows identify, isolate and detect different kind of faults, based on time-varying blind signal extraction and novelty detection using non-stationary vibration signals.

1.4.2 Specific objectives

- Develop an algorithm to estimate the instantaneous angular speed and the order components correctly, describing the system dynamic behavior and considering the time-varying operational conditions of the rotary machines.
- Develop a methodology for fault detection using novelty detection techniques taking into account the insufficient amount of vibration signals, the lack of labeled data and the unbalance of the faulty/undamaged classes.
- Design and implement a methodology that allows extracting the blind components in the vibration signal, involving correctly the characteristics of the fault processes that are embedded in the data.

1.5 Contributions of this work

The present work is done within the framework of data-driven machine diagnostics, including the detection, isolation and identification of different types of faults. In particular, the analysis of vibration signals that exhibit non-stationary processes generated either by rotational speed changes or non-stationary faults like rolling element bearing failures. In that sense, we aim to provide some approaches and methodologies to diagnose damages in machines under non-stationary operating conditions, which are focused on the industry scenario where the maintenance operators do not have specialized knowledge in condition-based monitoring. With this in mind, the main contributions of the work are described:

- An order tracking approach (Cardona-Morales et al., 2014), named *square root cubature Kalman filtering - order tracking* (SRCKF_OT), is proposed aiming to estimate simultaneously the instantaneous frequency (IF) associated to the shaft speed, and the order components related with that IF. The proposed SRCKF_OT introduces an oscillatory model the may describe the machine operating conditions and provides a set of narrow-band spectral components that are governed by the shaft speed. Those components could be stationary and cyclostationary giving useful information that allows identifying the faulty processes generated in the machine. An important characteristic of the proposed approach is that it may be implemented on-line because the estimation of the IF and the order components is based on the Kalman recursion. As a consequence, SRCKF_OT can characterize the vibration signal taking into account that each spectral component describes the performance of the mechanisms present inside the machine, therefore, this approach contributes in the fault isolation stage.
- We propose a novel methodology for fault detection, called *frequency-located fault detection*, based on novelty detection techniques that use one-class classifiers (OCC)

to describe the normal machine performance. The methodology includes two different OCC schemes oriented to provide to the machine operator information about the machine in two senses: detecting if any fault exists or not (traditional scheme), and detecting the spectral band where the fault arise (novel scheme). This information allows to inferring the type of the fault that it is starting into the machine and to give the needed elements of judgment to deciding the possible machine repairs. To this end, the methodology comprises a classical framework of pattern recognition, where it is performed the vibration signal characterization and the machine health condition classification. The contribution consists of utilizing as dynamic features of the machine condition, the order components obtained with the proposed SRCKF_OT approach. Then, the features are fed into the classification algorithms under both OCC schemes, but in the first scheme statistical and similarity characteristics are computed from the order components, yet in the novel scheme those narrow-band components comprise a new set of pseudo-observations. This fact allows identifying the order component that is an outlier and may be considered a potential fault in a specific part of the machine.

- Regarding the fault identification, we proposed a methodology based on the SRCKF_OT approach, taking advantage of the cyclostationary properties that the order components could exhibit. In the concrete case, the methodology consists of to compute the envelope of the narrow-band components and to verify if the rolling element bearing faults arise. The proposed methodology is focused on the field of blind signal extraction, so, the obtained order components are filtered versions of the raw signal that inherit the stationary and cyclostationary properties.

2 Instantaneous frequency estimation based on order tracking

Vibration analysis of rotating machines is one of the most used techniques for fault diagnosis and condition monitoring due to its high performance and low implementation cost. Nowadays, one of the main challenges in vibration analysis is to track and reduce influence of changes during time–varying operating conditions and loads. In this regard, techniques grounded on order tracking (OT) had been proposed, which are devoted to obtaining fundamental component features of the shaft reference speed (called *basic order*) and capture dynamics of measured vibration signals. The OT technique has shown to be useful mostly within the analysis of non–stationary vibration signals, condition monitoring, and fault diagnosis (Bai et al., 2005). OT allows identifying the rotation speed and the spectral/order components, being both fundamental to describe the machine state as well as its conforming mechanisms during changing loads and speed regimes (e.g. start and stop of the machine) (Guo et al., 2006; Pan and Lin, 2006).

Mostly, OT is based on estimation of the instantaneous frequency (IF) that in turn can be extracted from a given time–frequency representation (Guo et al., 2006; Gao et al., 2006). For instance, the Gabor transform is employed in Zhao et al. (2008), where the shaft speed reference signal is not required allowing to analyze rotating machines with less quantity of sensors or when the reference signal is not available at all. Nevertheless, the windowed Fourier–based transforms have limited resolution in both, time and frequency, axes and they suffer from increased computational burden (Pan and Wu, 2007). To overcome this issue, OT technique is carried out grounded on parametric modeling including adequate estimation of spectral/order components.

Particularly, an OT approach based on Kalman filtering is suggested in Bai et al. (2005). Its improved version with increased precision, termed *Vold-Kalman filtering* (VKF-OT), is proposed in Pan and Lin (2006); Pan and Wu (2007). Yet, either of them needs for measuring the shaft speed, which makes the order analysis more complex since tracking performance must rely on the synchronization process between vibration signal and its reference speed. Furthermore, shaft speed measurement implies installing additional equipment close to the machine, which in not all situations may be feasible. To cope with this trouble, indirect measurement of shaft speed, based just on the instantaneous frequency, is also discussed in Scala and Bitmead (1994); Bittanti and Saravesi (2000), where a frequency tracker is in-

troduced using the oscillatory model. Parameters of the model are calculated employing the Extended Kalman Filtering (EKF), which supplies amplitude, phase, and mainly frequency of harmonic signal, for de-noising in non-stationary environments. Nonetheless, tuning of the above approach is heuristic and relies to some degree on expertise. In this regard, better estimation of amplitude and frequency using a non–linear least minimum square algorithm is suggested in Avendano-Valencia et al. (2007).

On the other and, an improved version of the EKF frequency tracker for non-stationary harmonic signals is presented in Hajimolahoseini et al. (2008), where the time-varying amplitude is another state variable included in the oscillatory model, i.e., the standard state space model of a measured signal takes into consideration amplitude variations of harmonic data, which can be assumed as time–variant or even corrupted. In many real applications, however, the number of harmonic signals to track can increase remarkably, and consequently the needed amount of state variables implies more computational cost affecting the on–line tracking task implementation.

This chapter discusses a nonlinear model-based OT approach for condition monitoring of non-stationary vibration signals that reduces the computational burden by decreasing the model order. Particularly, time-varying amplitude is estimated assuming the state variables as the in-phase and quadrature components from the input signal, and then computing the quadratic mean between those components. As a result, the amount of state variables required to track the signal becomes lower and hence the model order itself also decreases. Besides, to avoid numerical precision errors that are implicit during derivative calculation within the EKF framework (Cardona-Morales et al., 2011), the use of Square-Root Cubature Kalman Filter is considered (Arasaratnam et al., 2010; Arasaratnam and Haykin, 2011). The proposed scheme, presented in Cardona-Morales et al. (2014) is tested over several experiments: first, a synthetic signal is used aiming to distinguish between closed-order components; second, a test rig is employed under two different regimes, steady-state and non-stationary, to track main order components and extract them; and finally, real-world case studies are used to validate the approach, including vibration signals acquired on ship driveline, internal combustion engine, and two international contest using signals from a wind turbine and gearbox.

2.1 Order tracking and instantaneous angular speed model

Given a machine vibration signal, OT provides estimation of oscillatory modes and corresponding amplitudes. The machine shaft speed is assumed as *basic order*, while superior orders are related as *shaft speed harmonics*. So, shaft speed, $\eta = 60\,f_r$, is assumed as the machine shaft fundamental frequency, where η is the speed, expressed in revolutions per minute

(*rpm*), while f_r is given in *Hz*.
As a rule, a vibration signal, $y(n) \in \mathbb{R}$, that is acquired from a rotating machine can be represented along the discrete-time axis, n, as a superposition of K sinusoidal functions (termed *order components*), as follows:

$$y(n) = \sum_{k=1}^{K} a_k(n) \cos(k\omega(n)n + \varphi_k(n)) \tag{2.1}$$

where notations $a_k(n)$ and $\varphi_k(n)$ stand for the amplitude and phase of k-th order component, respectively; $\omega(n) = 2\pi f_r(n)$ is the angular frequency of a rotational frequency $f_r(n)$. Variables $a_k(n)$, $\varphi_k(n)$, and $\omega(n)$ are time-varying.
So, based on a representative mono-component model that is delayed in one time instant, a version of lagged signal, $y(n+1)$, can be expressed as (Hajimolahoseini et al., 2012):

$$\begin{aligned} y(n+1) =& a(n+1)\cos(\omega(n+1)n + \varphi(n+1))\cos(\omega(n+1)) \\ & - a(n+1)\sin(\omega(n+1)n + \varphi(n+1))\sin(\omega(n+1)). \end{aligned} \tag{2.2}$$

Under the assumption that the amplitude, phase, and frequency have smooth transitions (i.e., their speed does not change strongly enough to have discontinue behavior) (Borghesani et al., 2012), the next approximations hold: $a(n+1) \cong a(n)$, $\varphi(n+1) \cong \varphi(n)$, and $\omega(n+1) \cong \omega(n)$. Therefore, Eq. (2.2) can be rewritten to get the following simpler decomposition that is given in terms of sine and cosine components as:

$$\begin{aligned} y(n+1) =& a(n)\cos(\omega(n)n + \varphi(n))\cos(\omega(n)) \\ & - a(n)\sin(\omega(n)n + \varphi(n))\sin(\omega(n)). \end{aligned} \tag{2.3}$$

On–line processing that appraises both, order component estimation and inference of machine dynamic behavior can be accomplished if Eq. (2.3) is now expressed through the following state space model:

$$\boldsymbol{x}(n+1) = \begin{bmatrix} \cos\omega(n) & -\sin\omega(n) \\ \sin\omega(n) & \cos\omega(n) \end{bmatrix} \boldsymbol{x}(n) + \begin{bmatrix} 1 \\ 0 \end{bmatrix} \boldsymbol{\xi}(n) \tag{2.4a}$$

$$y(n) = \begin{bmatrix} 1 & 0 \end{bmatrix} \boldsymbol{x}(n) + v(n) \tag{2.4b}$$

where variables $\boldsymbol{\xi}(n) \in \mathbb{R}^{2\times 1}$ and $v(n) \in \mathbb{R}$ are the process and measurement noise, respectively; $\boldsymbol{x}(n) = [x_1(n)\ x_2(n)]^\top \in \mathbb{R}^{2\times 1}$ is the state variable vector, with vector elements defined as $x_1(n) = a(n)\cos(\omega(n)n + \varphi(n))$ and $x_2(n) = a(n)\sin(\omega(n)n + \varphi(n))$. In this work, amplitude of signal $y(n)$ is computed assuming that state variables, $x_1(n)$ and $x_2(n)$, are provided, respectively, as in-phase and quadrature components of the signal. Afterwards, it holds for amplitude that $a(n) = \sqrt{x_1(n)^2 + x_2(n)^2}$.

Generally, the singular–state space model of Eq. (2.4a) can be extended to the multiple sinusoidal component model as:

$$\begin{bmatrix} \boldsymbol{x}_1(n+1) \\ \vdots \\ \boldsymbol{x}_K(n+1) \end{bmatrix} = \begin{bmatrix} \boldsymbol{M}(\omega_1) & \mathbf{0} & \cdots & \mathbf{0} \\ \vdots & \vdots & \ddots & \vdots \\ \mathbf{0} & \mathbf{0} & \cdots & \boldsymbol{M}(\omega_K) \end{bmatrix} \begin{bmatrix} \boldsymbol{x}_1(n) \\ \vdots \\ \boldsymbol{x}_K(n) \end{bmatrix} + \begin{bmatrix} \boldsymbol{\xi}_1(n) \\ \vdots \\ \boldsymbol{\xi}_K(n) \end{bmatrix} \tag{2.5}$$

where $\boldsymbol{M}(\omega_k) \in \mathbb{R}^{2\times 2}$ is the *state transition matrix*, defined as follows:

$$\boldsymbol{M}(\omega_k) = \begin{bmatrix} \cos\omega_k(n) & -\sin\omega_k(n) \\ \sin\omega_k(n) & \cos\omega_k(n) \end{bmatrix} \tag{2.6}$$

Besides, the model in Eq. (2.5) can be described also in vectorial form as:

$$\boldsymbol{X}(n+1) = \boldsymbol{F}(n+1,n)\boldsymbol{X}(n) + \boldsymbol{\xi}(n) \tag{2.7}$$

where $\boldsymbol{X}(n) \in \mathbb{R}^{2K\times 1}$ is the state variable vector comprising in-phase and quadrature component for each order k, vector $\boldsymbol{x}_k(n)$ represents the k-th state variable corresponding to k-th order component; term $\boldsymbol{F}(n+1,n) \in \mathbb{R}^{2K\times 2K}$ denotes the state transition matrix defining the changes of state variable vector through the time; $\boldsymbol{\xi}(n) \sim \mathcal{N}(\mathbf{0}, \boldsymbol{Q}(n)) \in \mathbb{R}^{2K\times 1}$ is the process noise, where $\boldsymbol{Q}(n) \in \mathbb{R}^{2K\times 2K}$ is the covariance matrix of process noise; and diagonal of $\boldsymbol{Q}(n)$ is defined as $\text{diag}\{\boldsymbol{Q}(n)\} = [q_1^a\ q_1^a\ \cdots\ q_K^a\ q_K^a\ q_{K+1}^f]$, where $q_i^a (i = 1,\ldots,K)$ denotes amplitude variance of the order component and q_{K+1}^f denotes frequency variance describing the system dynamics.

At the same time, measurement $y(n)$ in Eq. (2.4a) can be written in a short form as

$$\begin{aligned} y(n) &= \begin{bmatrix} \boldsymbol{h} & \boldsymbol{h} & \cdots & \boldsymbol{h} \end{bmatrix} \begin{bmatrix} \boldsymbol{x}_1(n) \\ \vdots \\ \boldsymbol{x}_k(n) \end{bmatrix} + v(n) \\ &= \boldsymbol{H}\boldsymbol{X}(n) + v(n) \end{aligned} \tag{2.8}$$

where $\boldsymbol{h} = [1\ 0]$ appraises the measurement matrix $\boldsymbol{H} \in \mathbb{R}^{1\times 2K}$, $v(n) \sim \mathcal{N}(0, r(n)) \in \mathbb{R}$ is the measured noise, and $r(n) \in \mathbb{R}$ is the measured variance.

To estimate the IF that is associated to $y(n)$, an additional state variable should be introduced at $(K+1)$-th position. In this regard, state variable is set based on described oscillatory model (see Eqs. (2.7) and (2.8)), as discussed in Hajimolahoseini et al. (2012). Thus one can assume that $\omega_k(n) = x_{K+1}(n)$, and therefore the needed state space model takes the form:

$$\begin{bmatrix} \boldsymbol{x}_1(n+1) \\ \vdots \\ \boldsymbol{x}_K(n+1) \\ \boldsymbol{x}_{K+1}(n+1) \end{bmatrix} = \begin{bmatrix} \boldsymbol{M}(x_{K+1}) & & & \\ & \ddots & & \\ & & \boldsymbol{M}(Kx_{K+1}) & \\ & & & 1 \end{bmatrix} \begin{bmatrix} \boldsymbol{x}_1(n) \\ \vdots \\ \boldsymbol{x}_K(n) \\ \boldsymbol{x}_{K+1}(n) \end{bmatrix} + \begin{bmatrix} \boldsymbol{\xi}_1(n) \\ \vdots \\ \boldsymbol{\xi}_K(n) \\ \boldsymbol{\xi}_{K+1}(n) \end{bmatrix} \tag{2.9}$$

$$y(n) = \begin{bmatrix} \boldsymbol{h} & \cdots & \boldsymbol{h} & 0 \end{bmatrix} \begin{bmatrix} \boldsymbol{x}_1(n) \\ \vdots \\ \boldsymbol{x}_K(n) \\ \boldsymbol{x}_{K+1}(n) \end{bmatrix} + \begin{bmatrix} v_1(n) \\ \vdots \\ v_K(n) \\ v_{K+1}(n) \end{bmatrix} \tag{2.10}$$

where the remaining terms of the state transition matrix are zero filled.
Lastly, the process equation in Eq. (2.9) can be written in short form as

$$\boldsymbol{X}(n+1) = \boldsymbol{\vartheta}(n, \boldsymbol{X}(n)) + \boldsymbol{\xi}(n) \tag{2.11}$$

where $\boldsymbol{\vartheta}(n, \boldsymbol{X}(n))$ is a state transition nonlinear vectorial function, such that estimation of $\boldsymbol{X}$ implies a set of nonlinear equations, which can be implemented by using the widely known nonlinear Kalman filtering.

2.2 Estimation of Model Parameters

2.2.1 K-orders based on maxima frequencies

As regards the value K denoting the order components, it can be defined using two different approaches: firstly, the *physics-based* calculation that requires exact knowledge about machine mechanisms to choice the interest components (Pan and Lin, 2006). This choice includes maintenance crew having available information of geometric and physical characteristics of every single machine mechanism; secondly, the *data-driven* estimation based on the analysis of measured vibration signal power. Estimation of order components, yielding high amplitude level extracted from time-frequency signal representation, includes the following steps:

– Given a signal signal $y(n)$, compute its time-frequency representation, $\boldsymbol{\Omega}_y(i, j)$, that is a 2-dimensional plane with positions (i, j), being $i = 1, \ldots, n;\ j = 1, \ldots, l$, where i and j are the bins located at the time and frequency domains, respectively.

Table 2.1: SRCKF algorithm (Part 1).

Initialization:

1. Define the input values
   $y_{1:N}$, $\widehat{\boldsymbol{x}}_0$, $\boldsymbol{P}_{0|0} = \boldsymbol{S}_{0|0}\boldsymbol{S}_{0|0}^{\top}$, $\boldsymbol{Q}_0$, $\boldsymbol{R}_0$
2. Define the cubature points
   $\phi_i = \sqrt{m/2}\left\{\left[\boldsymbol{I}_{m\times m} \quad -\boldsymbol{I}_{m\times m}\right]\right\}$

Tracking:

3. **for** $n = 1$ to N **do**

Time update

4. Evaluate the cubature points ($i = 1, 2, \ldots, m$), where $m = 2K + 1$,
   $\boldsymbol{\chi}_{i,n-1|n-1} = \boldsymbol{S}_{n-1|n-1}\phi_i + \widehat{\boldsymbol{x}}_{n-1|n-1}$
5. Evaluate the propagated cubature points ($i = 1, 2, \ldots, m$)
   $\boldsymbol{\chi}^*_{i,n|n-1} = \boldsymbol{\vartheta}\left(\boldsymbol{\chi}_{i,n-1|n-1}\right)$
6. Estimate the predicted state
   $\widehat{\boldsymbol{x}}_{n|n-1} = \frac{1}{m}\sum_{i=1}^{m}\boldsymbol{\chi}^*_{i,n|n-1}$
7. Estimate the square-root factor of prediction error covariance
   $\boldsymbol{S}_{n|n-1} = \text{tria}\left\{\left[\widehat{\boldsymbol{\chi}}_{n|n-1} \quad \boldsymbol{S}_{\boldsymbol{Q}|n}\right]\right\}$
   where $\widehat{\boldsymbol{\chi}}_{n|n-1} = \frac{1}{\sqrt{m}}\left[\boldsymbol{\chi}^*_{1,n|n-1} - \widehat{\boldsymbol{x}}_{n|n-1} \quad \boldsymbol{\chi}^*_{2,n|n-1} - \widehat{\boldsymbol{x}}_{n|n-1} \cdots \boldsymbol{\chi}^*_{m,n|n-1} - \widehat{\boldsymbol{x}}_{n|n-1}\right]$
   and $\boldsymbol{S}_{\boldsymbol{Q}|n}$ denotes a square-root factor of $\boldsymbol{Q}_{n-1}$

– Find magnitude value, $\alpha = \arg\max_{\forall i}\{\Omega_y(i, j)\}$, preserving positions (i_α, j_α), where i_α and j_α denote time and frequency indexes, respectively, where α takes place. Then, the local maxima are extracted from frequency vector $\{\Omega_y(i_\alpha, j)\}$. It allows to build a set of k frequencies with the greatest vibration power, $z(k)$.

– Compute the rate between the first component of $z(k)$ and the $(k-1)$ remainder components, to obtain the different harmonics or spectral components $\Gamma(k)$, where $\Gamma(k) = \{z(k)/z(1) : k = 2, \ldots, K\}$.

2.2.2 IAS-OT model parameters

As seen in Eqs. (2.9) and (2.10), parameter computation implies a recursive nonlinear analysis allowing to get an approximated solution when Gaussian noise is assumed, but avoiding calculation of corresponding Jacobians of state variables. To this end, the Square-Root Cubature Kalman Filter (SRCKF), which is based on recursive propagation of state variable

Table 2.1: SRCKF algorithm - (Part 2).

	Measurement Update
8.	Evaluate the cubature points ($i = 1, 2, \ldots, m$) $\boldsymbol{\chi}_{i,n\|n-1} = \boldsymbol{S}_{n\|n-1}\boldsymbol{\phi}_i + \widehat{\boldsymbol{x}}_{n\|n-1}$
9.	Evaluate the propagated cubature points ($i = 1, 2, \ldots, m$) $\boldsymbol{\psi}_{i,n\|n-1} = \boldsymbol{h}\left(\boldsymbol{\chi}_{i,n\|n-1}\right)$
10.	Estimate the predicted state $\widehat{\boldsymbol{y}}_{n\|n-1} = \frac{1}{m}\sum_{i=1}^{m}\boldsymbol{\psi}_{i,n\|n-1}$
11.	Estimate the square-root of the innovation covariance matrix $\boldsymbol{S}_{yy,n\|n-1} = \text{tria}\left\{\left[\mathcal{Y}_{n\|n-1} \quad \boldsymbol{S}_{\boldsymbol{R}\|n}\right]\right\}$ where $\mathcal{Y}_{n\|n-1} = \frac{1}{\sqrt{m}}\left[\boldsymbol{\psi}_{1,n\|n-1} - \widehat{\boldsymbol{y}}_{n\|n-1} \quad \boldsymbol{\psi}_{2,n\|n-1} - \widehat{\boldsymbol{y}}_{n\|n-1} \ldots \boldsymbol{\psi}_{m,n\|n-1} - \widehat{\boldsymbol{y}}_{n\|n-1}\right]$ and $\boldsymbol{S}_{\boldsymbol{R}\|n}$ denotes a square-root factor of $\boldsymbol{R}_n$
12.	Estimate the cross-covariance matrix $\boldsymbol{P}_{xy,n\|n-1} = \mathcal{X}_{n\|n-1}\mathcal{Y}^{\top}_{n\|n-1}$ where $\mathcal{X}_{n\|n-1} = \frac{1}{\sqrt{m}}\left[\boldsymbol{\chi}_{1,n\|n-1} - \widehat{\boldsymbol{x}}_{n\|n-1} \quad \boldsymbol{\chi}_{2,n\|n-1} - \widehat{\boldsymbol{x}}_{n\|n-1} \ldots \boldsymbol{\chi}_{m,n\|n-1} - \widehat{\boldsymbol{x}}_{n\|n-1}\right]$
13.	Estimate the Kalman gain $W_n = \left(\boldsymbol{P}_{xy,n\|n-1} / \boldsymbol{S}^{\top}_{yy,n\|n-1}\right) / \boldsymbol{S}_{yy,n\|n-1}$
14.	Estimate the updated state $\widehat{\boldsymbol{x}}_{n\|n} = \widehat{\boldsymbol{x}}_{n\|n-1} + W_n\left(y_n - \widehat{\boldsymbol{y}}_{n\|n-1}\right)$
15.	Estimate the square-root factor of the corresponding error covariance $\boldsymbol{S}_{n\|n} = \text{tria}\left\{\left[\mathcal{X}_{n\|n-1} - W_n\mathcal{Y}_{n\|n-1} \quad W_n\boldsymbol{S}_{\boldsymbol{R}\|n}\right]\right\}$
16.	**end**

moments (mean and variance), is suggested in Arasaratnam et al. (2010), under assumption that implicated nonlinear function, $\boldsymbol{\vartheta}$, should be reasonably smooth. In this case, a quadratic function near the prior mean is used assuming that it could properly approximating the given nonlinear function. To this end, the error covariance matrix should be symmetric and positive definiteness to preserve the filter properties on each update cycle, and hence, SRCKF uses a forced symmetry on the solution of the matrix Ricatti equation improving the numerical stability of the Kalman filter (Grewal and Andrews, 2001), whereas the underlying meaning of the covariance is embedded in the positive definiteness (Arasaratnam et al., 2010).

The SRCKF algorithm that is described in Table 2.1 carries out the QR decomposition (termed triangularization procedure, $\boldsymbol{S} = \text{tria}\{\cdot\}$), where the $\boldsymbol{S}$ is a lower triangular matrix

and denotes a square-root factor (Arasaratnam et al., 2010).

2.2.3 Constrained model state variables

Constraints on states $\boldsymbol{x}(n)$ to be estimated are important model information that is often not used in state estimation. Typically, such constraints are due to physical limitations on the states. In Kalman filter theory, there is no general way of incorporating these constraints into estimation problem. However, the constraints can be incorporated in the filter by projecting the unconstrained Kalman filter estimates onto the boundary of the feasible region at each time step (Simon and Chia, 2002; Ungarala et al., 2007). The numerical optimization at each time step may be a challenge in time-critical applications. In this section, a simple method introduced in Kandepu et al. (2008) is applied to handle state constraints in the SRCKF. Assume that the constraints of state variables are represented by box constraints as follow:

$$\boldsymbol{x}_L(n) \leq \boldsymbol{x}(n) \leq \boldsymbol{x}_H(n) \tag{2.12}$$

where subindexes L and H denote the lower and upper boundaries, respectively. The method is illustrated for $\boldsymbol{x}(n) \in \mathbb{R}^2$. In case of a second order system, the feasible region by the box constraints can be represented by a rectangle as in Fig. 2.1. It is showed the illustration of the steps of constraint handling of the SRCKF algorithm from one time step to the next. At $t = n-1$, the true state $\boldsymbol{x}_n$, its estimate $\widehat{\boldsymbol{x}}_{n-1}$ and state covariance are selected. The constraints information can be incorporated in the SRCKF algorithm in a simple way during the time-update step (Table 2.1-Part 1). After the propagation of the sigma points (step 5.), the (unconstrained) transformed sigma points which are outside the feasible region can be projected onto the boundary of the feasible region and continue the further steps. In Fig. 2.1, at $t = n$ two sigma points which are out-side the feasible region are projected onto the boundary (right plot in the figure). The mean and covariance with the constrained sigma points now represents the a priori state variable (x_n^{-SRCKF}) and covariance, and they are further updated in the measurement-update step (Table 2.1-Part 2). The advantage here is that the new a priori covariance includes information on the constraints, which should make the SRCKF estimate more efficient (accurate) compared to the SRCKF estimate without constraints. Extension of the proposed method to higher dimension, d, is straightforward. Alternative linear constraints, e.g., $C\boldsymbol{x} \leq d$ are easily included by projecting the sigma point violating the inequality normally onto the boundary of feasible region. It is observed that the new (constrained) covariance obtained at a time step is lower in size compared to the unconstrained covariance. If, in case, the estimate after the measurement-update (Table 2.1-Part 2) is outside the feasible region, the same projection technique can be extended. In a practical point of view, the boundaries are fixed according to maximum and minimum values that could take the state variables, it means, in case of the order components $L^a = \min y(n)$ and $H^a = \max y(m)$, whereas the IF constraints depend on the approximated knowledge of

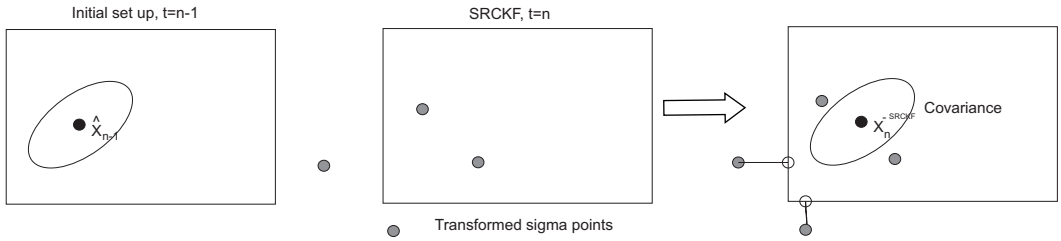

Figure 2.1: Illustration of sigma constrained points.

the machine speed range, where L^f and H^f are normally fixed as zero or idle speed and maximum speed, respectively.

2.3 Simulation Study

As recommended in Pan and Wu (2007), a testing signal is synthesized to validate performance of considered OT schemes in closed-order component identification. Particularly, the synthetic signal comprises the following three order components: 1*st*, 4*th*, and 4.2*th*, for each one the amplitude is linearly increased from $0-10$, $0-3$, and $0-2.5$, respectively. Order amplitude level is set as time-varying since it is assumed that most of the machine mechanisms have different vibration levels. The assumed reference shaft speed has an increment ranging from 0 to 1800 *rpm* (that is, 30 *Hz*) to reproduce a start-up machine process. Besides, the synthetic signal lasts 5 seconds going from initial steady state to final maximum speed. A sample frequency of 1 *kHz* is used through this simulation.

Generally, methods based on Fourier transform face limitations in distinguishing closed-order components, as seen in Figure 2.2 that shows time-frequency representation of synthetic signal and its corresponding time series. Also, it is worth noting that the amplitude differences between the first order and its harmonics make almost insignificant the low frequency information. If using OT techniques instead, it is possible to capture properly information about each order component. This work uses OT two approaches based on parametric models: VKF_OT and the introduced SRCKF_OT scheme. Both schemes have computation parameters that are fixed as suggested in Pan and Wu (2007); Alves and Coelho (2010). Parameters that influence tracking performance the most are the initial values of process covariance matrix, $\boldsymbol{Q}$, and measurement noise, r. In the proposed SRCKF_OT scheme, filter response bandwidth depends on the signal error covariance, q_i^a, and in a less extent to the frequency error covariance, q^f, that is, the following condition should hold: $q^f < q_i^a$. For this reason, when choosing initialization parameters, two aspects should account: the maximum range of machine speed and the maximum variance of measured vibration signal to preserve a needed convergence region of estimation (Ungarala et al., 2007).

Aforementioned parameter tuning is carried out for each testing. In the case of the synthetic

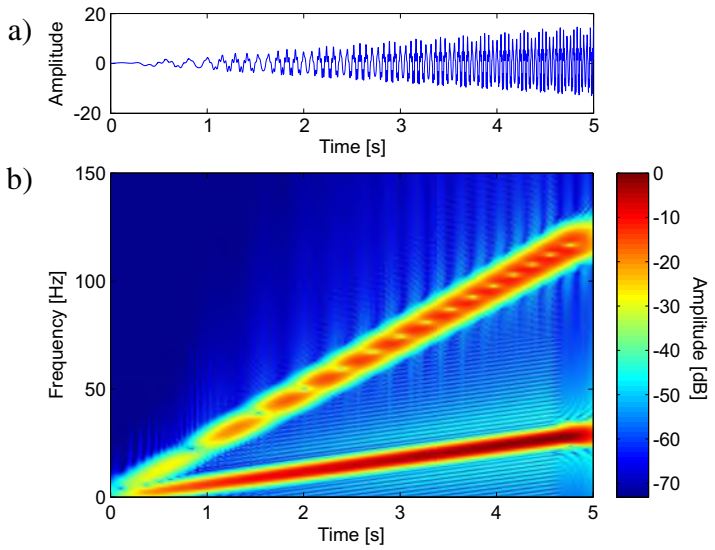

Figure 2.2: Simulated synthetic signal with closed-order components: a) in time domain, and b) the time-frequency representation obtained by STFT (hamming window, 512 frequency samples and 50% overlap).

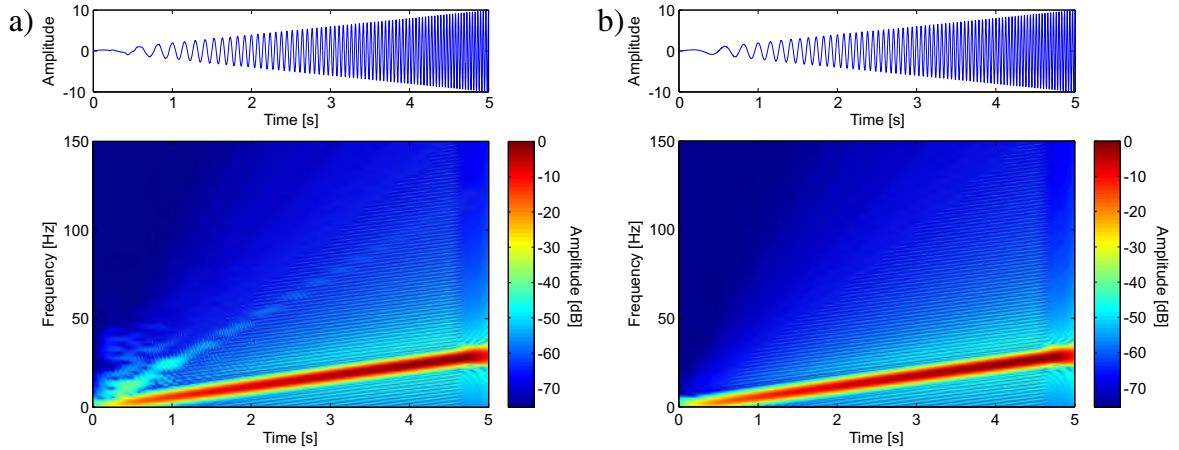

Figure 2.3: 1*st* order component tracked from the synthetic signal, in time domain (top) and the time-frequency representation using STFT (bottom), which is calculated using the approaches: a) SRCKF_OT, b) VKF_OT.

signal, therefore, the following values of initialization parameters are fixed for SRCKF_OT scheme: $q_i^a = 10^{-11}$, $q^f = 10^{-12}$, and $r = 10^{-9}$; while for VKF_OT scheme: $q = 10^{-10}$, and $r = 10^{-3}$.

Figures 2.3, 2.4, and 2.5 show accomplished order components (i.e., 1*st*, 4*th*, and 4.2*th*, respectively) that are estimated from the synthetic signal using the above described models. As seen in Figure 2.3, the VKF_OT scheme accomplishes better energy concentration of the 1*st* order component. Proposed scheme achieves energy concentration of the 1*st* order com-

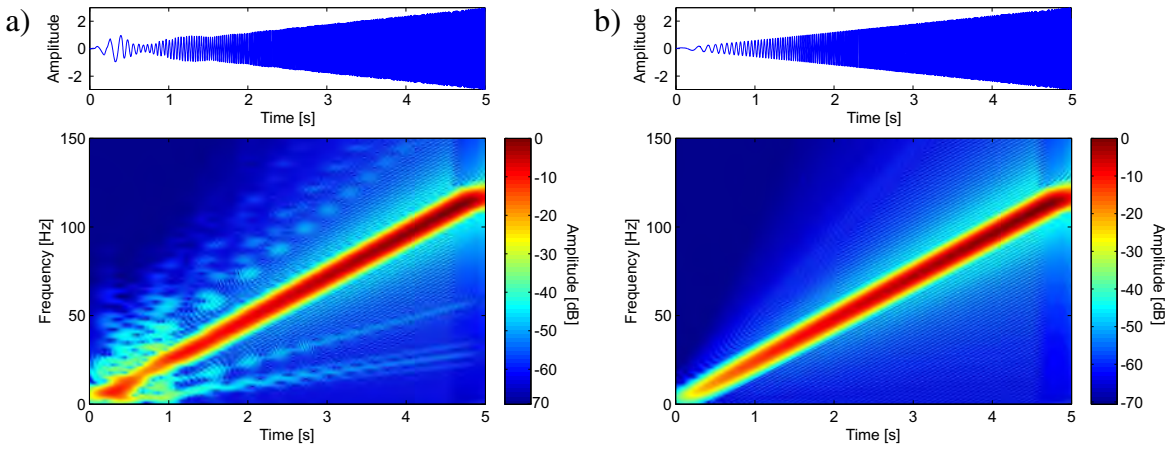

Figure 2.4: 4*th* order component tracked from the synthetic signal, in time domain (top) and the time-frequency representation using STFT (bottom), which is calculated using the approaches: a) SRCKF_OT, b) VKF_OT.

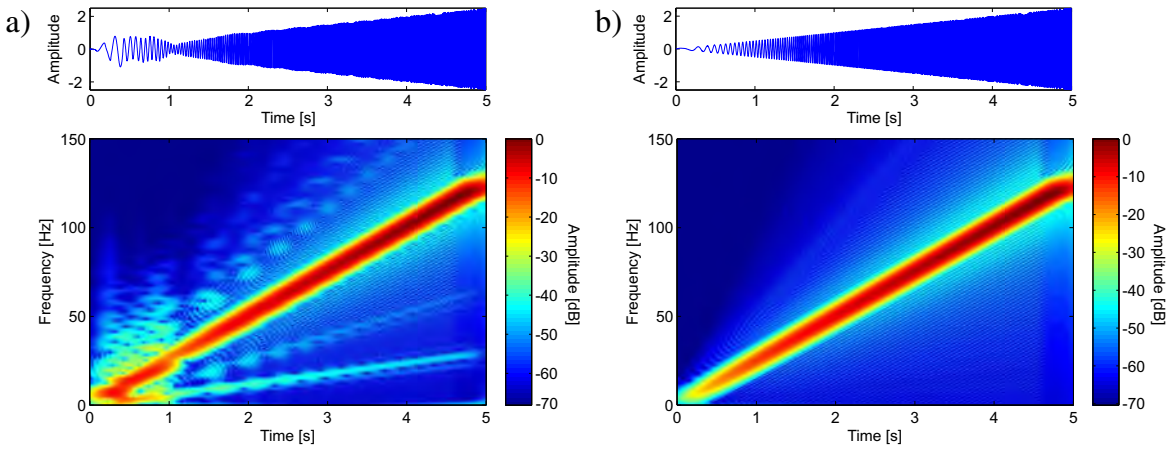

Figure 2.5: 4.2*th* order component tracked from the synthetic signal, in time domain (top) and the time-frequency representation using STFT (bottom), which is calculated using the approaches: a) SRCKF_OT, b) VKF_OT.

ponent, but also preserves spectral information associated with other spectral components. This degradation happens just within the first second until the Kalman recursion converges. A similar situation takes place during tracking of 4*th* and 4.2*th* order components (see Figures 2.4 and 2.5). But in this situation, spectral contamination becomes higher since the order components are closer. Once the Kalman recursion converges, however, order tracking improves remarkably. At this point, two aspects must be highlighted: a) both OT schemes estimate correctly closed-order components (either waveform or amplitude); b) SRCKF_OT scheme gets higher convergence time, especially, when estimating 4*th* and 4.2*th* order components.

To determine the estimation accuracy of tracked closed-order components, Table 2.2 shows

Table 2.2: Estimated RMSE for synthetic signal

	Parameters	1*st* order	4*th* order	4.2*th* order
VKF_OT	A	0.01	0.01	0.01
	WR	0.54	0.64	0.56
SRCKF_OT	A	0.09	0.16	0.24
	WR	0.07	0.23	0.24
	IF	0.29	-	-

the root mean squared error (RMSE) of estimated model parameters, namely, amplitude (noted A), waveform reconstruction (WR), and instantaneous frequency (IF). For IF estimation, only SRCKF_OT is applied since VKF_OT requires a reference pattern to track distinct order components. So, VKF_OT scheme gets the same estimated amplitude error for all considered order components. While using SRCKF_OT, the higher the order – the higher the amplitude error. But in the case of WR estimation, the error increases using VKF_OT. This error augmentation, which is due to a shift-phase between estimated and original components, is not perceptible in the Figures 2.3, 2.4, and 2.5. In contrast, SRCKF_OT gets the lower RMSE for estimated WR and IF. Thus, proposed approach allows to capture signal dynamics of the basic order, but it preserves the phase of each component. As a result, provided above detailed analysis shows that SRCKF_OT scheme gets better performance than VKF_OT.

2.4 Experiments on Test Rig: Universidad Nacional de Colombia data 1

Evaluation is rendered on test rig over fixed machine operating regimes: steady-state and non-stationary. In the former regime, performance is relevant because of importance of machine working analysis under normal operational conditions at given constant speed. In the latter regime, speed becomes time-varying (i.e., during coast-down maneuvers of the machine), and it is important to track order components for identifying machine dynamic behavior.

As shown in Figure 2.6, experimental test rig includes a 2*HP* electromotor `Siemens` with 1800*rpm* maximum speed. The motor is connected to shaft by a rigid coupling and has two supports, each one holding a ball bearing `SKF-6005NR` and two wheels. Drilling wells are designed to create either static or dynamic unbalance problems. To measure machine mechanical vibration, accelerometers are also included, which are located perpendicularly to the shaft horizontal plane (labeled as *accelerometer location*). In this experiment, just the `ACC102` accelerometer placed near the machine is employed, which has a measurement

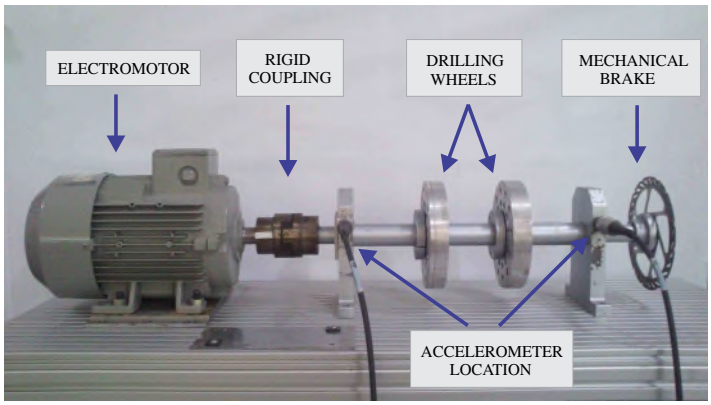

Figure 2.6: Experimental set-up for test rig.

range of $0-10$ *kHz* and 100 *mV/g* of sensibility. The `National Instruments USB-6009` data acquisition card acquires vibration recordings at 20 *kHz* sampling frequency.

2.4.1 Steady-state regime analysis

In this regime, the main goal of provided testing is to compare achieved performance of amplitude and waveform estimation of both considered OT schemes under different machine states: bearing fault and undamaged. Used data set are acquired on described above test rig at fixed 1800 *rpm* speed. 20 vibration recordings are obtained from aforementioned measurement locations. Besides, according to bearing mechanical characteristics, inner and outer race frequencies are fixed as $6.3th$ and $3.7th$ order of shaft rotation frequency, respectively. Afterwards, input signal is filtered by low-pass filter with 2500 *Hz* cut frequency to preserve most of information.

Figure 2.7 shows an example of vibration signal that is acquired on test rig. As seen in subplot of Figure 2.7(a) for undamaged state, there are several salient spectral components, namely: $1st$ order (30 *Hz*) component showing the highest constant amplitude and having a periodic behavior; time-varying $6.3th$ order component (180 *Hz*) with amplitude ranging from -20 *dB* till -10 *dB*; and both, $13th$ order (390 *Hz*) and $14th$ order (420 *Hz*), components having meaningfulness amplitude. For bearing fault case, although $1st$ order component behaves similarly as in undamaged state, amplitude of higher order components changes differently (see Figure 2.7(b)), as follows: in case of $6.3th$ order component, amplitude span increases in 10 *dB* and shows an impact at 0.2 *seconds*; for $13th$ and $14th$ order components, bearing fault frequency harmonics are cyclo-stationary meaning that there are some hidden changes in the waveform that must be estimated.

So, the proposed procedure in Section 2.2 is carried out supplying the following order component set $\Gamma = \{1, 4, 5, 6.3, 8, 10, 11, 13, 14\}$, which regards bearing and shaft frequencies to be tracked by compared OT schemes. In addition, for this concrete experimental set-up, the

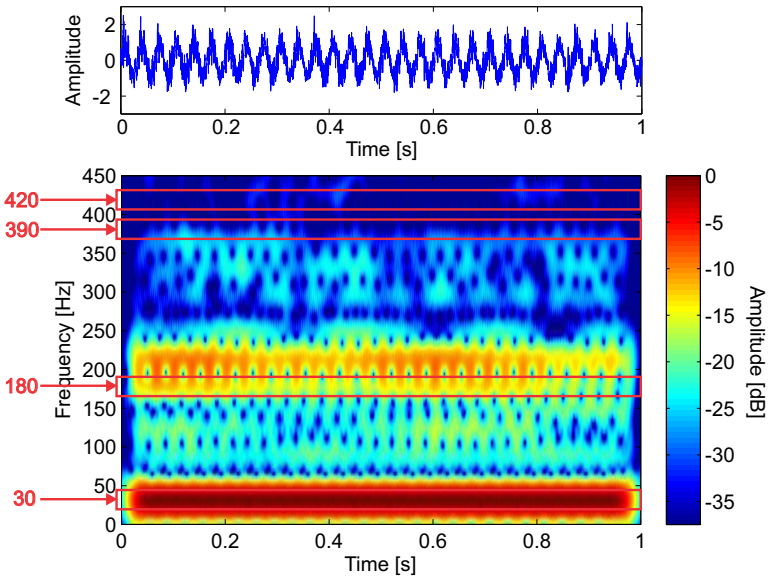

(a) Undamaged machine state in time domain (top) and its time-frequency representation using STFT (bottom).

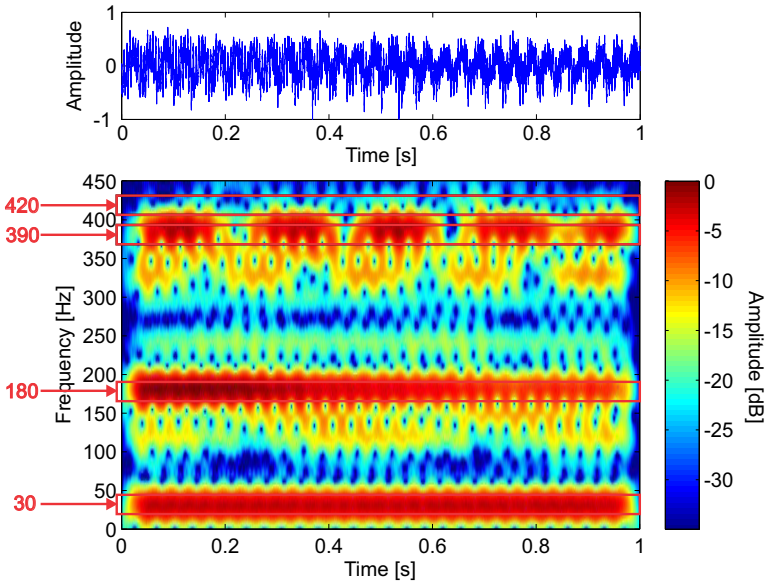

(b) Bearing inner race fault state in time domain (top) and its time-frequency representation using STFT (bottom).

Figure 2.7: Exemplary of acquired recordings on the test rig at 1800 *rpm*. (a) Undamaged machine state, (b) bearing fault, where displayed recording representations are: time-domain (top) and time-frequency (bottom). Red rectangles denote regions where a bearing inner race fault is expected.

initial parameters are heuristically set as: $q_i^a = 10^{-6}$, $q^f = 10^{-10}$, $r = 10^{-11}$ for SRCKF_OT, and $q = 10^{-10}$ and $r = 1$ for VKF_OT. Selected parameter values remain the same for whole database to test stability and tracking performance of compared OT estimation approaches.

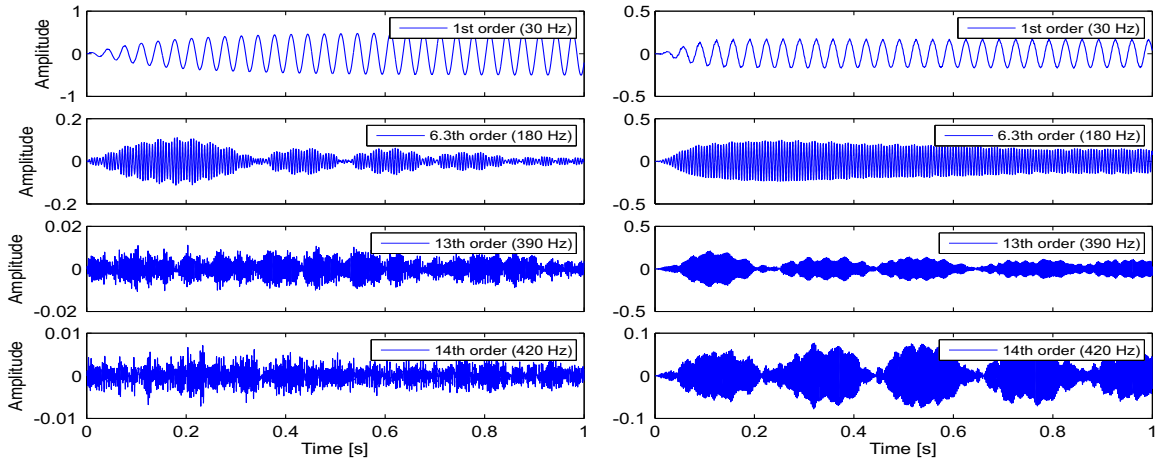

(a) SRCKF_OT

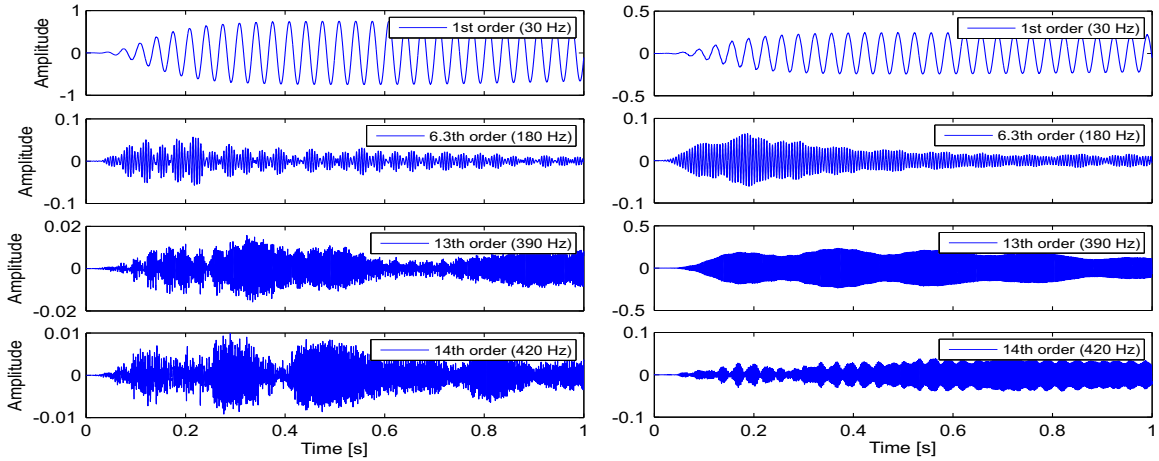

(b) VKF_OT

Figure 2.8: Waveform reconstruction of order component tracked from undamaged (left) and bearing fault (right) recordings at 1800 *rpm*

Under assumption that the higher the amplitude – the relevant the component, the following order Γ set is selected: 1*st*, 6.3*th*, 13*th*, and 14*th*. As seen in the Figure 2.8, either OT scheme reaches enough accuracy in all estimated component amplitudes. This fact means that frequency associated with each component keeps proportionally to corresponding harmonic, i.e., 1*st* order relates to 30 *Hz*, 6.3*th* to 180 *Hz*, and so on. Nonetheless, each OT scheme performs differently amplitude and waveform reconstruction, specifically, in case of 6.3*th*, 13*th*, and 14*th* order components.

In case of fault identification, Figure 2.8 shows that 6.3*th* order amplitude, estimated by SRCKF_OT scheme, clearly increases from 0.2 to 0.5, while VKF_OT based estimation does not capture any amplitude change. But that change should be fixed whenever a bearing fault appears. Also, SRCKF_OT based waveform reconstruction of 13*th* and 14*th* order

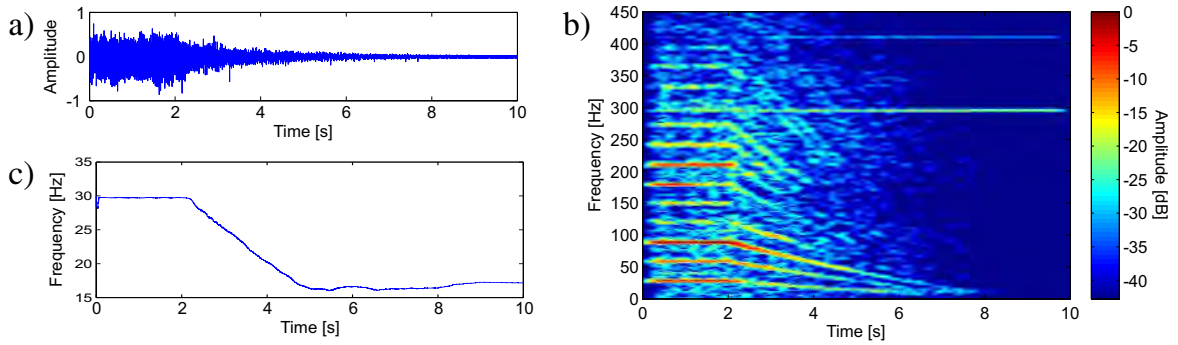

Figure 2.9: Example of an acquired signal in the test rig under coast-down operating condition: (a) in time domain, (b) time-frequency representation using STFT, and (c) estimated instantaneous frequency using SRCKF_OT.

components shows remarkable cyclo-stationary behavior as a result of short impacts, instead, the VKF_OT scheme does not show any information on that regard.

2.4.2 Non-stationary Regime Analysis

A set of signals is acquired to analyze order component estimation under non-stationary regime induced by speed changes, particularly, in the case of coast-down operating conditions. The dataset comprises 20 recordings that are acquired under coast-down operating condition in the test rig displayed in Figure 2.6. The data are measured within 10-seconds interval; this time interval is enough to register three different operating moments: *i*) maximum speed (1800 *rpm*), *ii*) once again, 5-*seconds* deceleration, and *iii*) total stop. In all 20 recordings, the beginning of the deceleration is not synchronized, i.e., the time instant when the machine is turned-off is different in each recording. Figure 2.9 displays an exemplary of an acquired signal during machine coast-down operation.

It must be noted that the order components present constant amplitude while the machine is working at maximum speed. But when deceleration occurs, the amplitude of each component monotonically decays until reaching the frequency minimum value, as seen in Figure 2.9(b). The frequency minimum value is the estimated IF by SRCKF_OT (see Figure 2.9(c)) as the base frequency that does not reach the zero level, yet preserving a frequency minimum with such a value that can be attributed to the structural resonance of the test rig. Nonetheless, the estimated IF allows identifying machine dynamic behavior, which is associated to the first order component. The IF supplies useful information about mechanical functionality in the proximity of the shaft.

For order component estimation, the set of initial parameters is the same as in the steady-state regime analysis (Section 2.4.1). However, the order components to be tracked, Γ, are only the first ten, since they contain most of information about machine behavior, including the main bearing frequencies. Particularly, Figures 2.10, 2.11, and 2.12 show first three or-

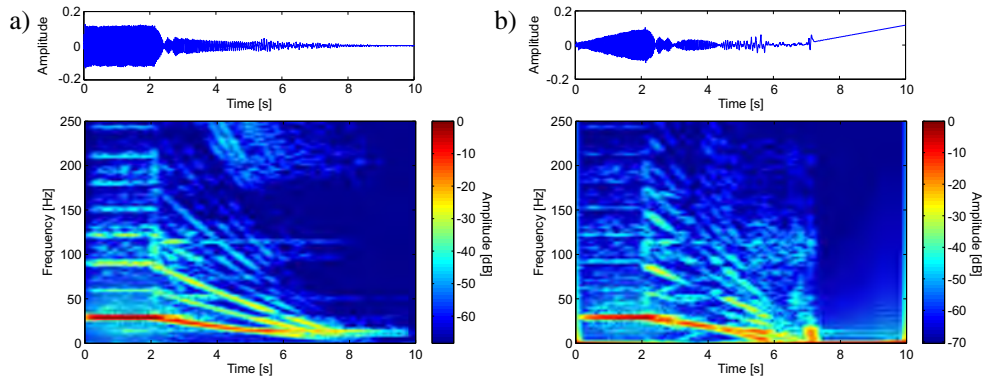

Figure 2.10: 1*st* order component tracked from the coast-down signal, in time domain (top) and the time-frequency representation using STFT (bottom), which is calculated using the approaches: a) SRCKF_OT, b) VKF_OT.

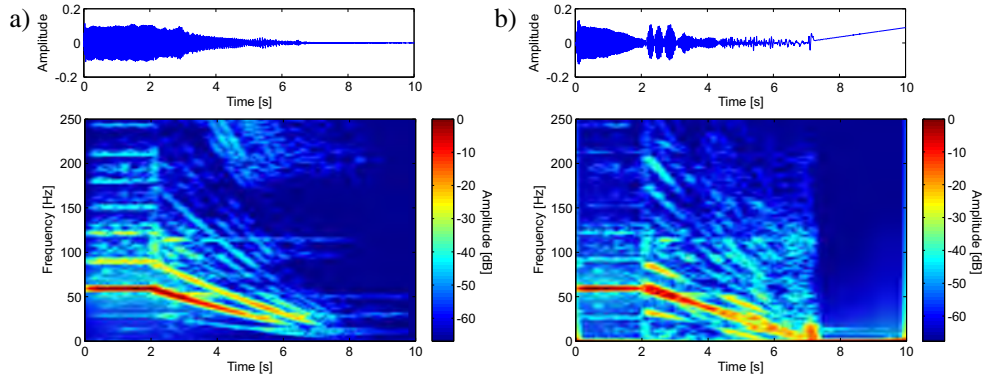

Figure 2.11: 2*nd* order component tracked from the coast-down signal, in time domain (top) and the time-frequency representation using STFT (bottom), which is calculated using the approaches: a) SRCKF_OT, b) VKF_OT.

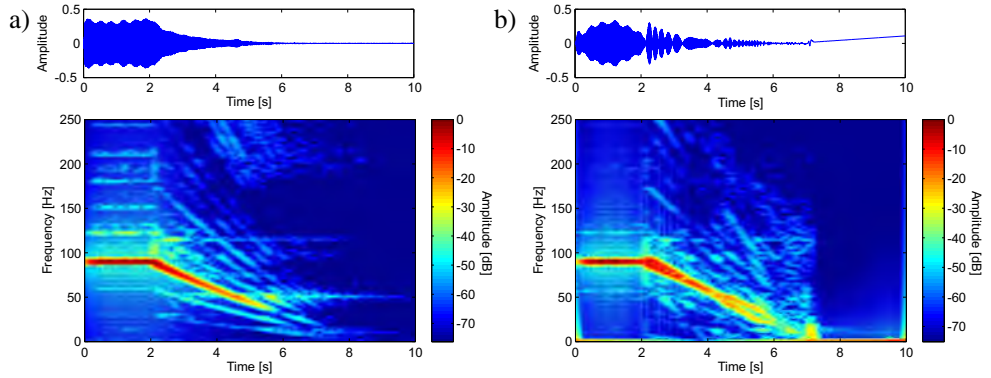

Figure 2.12: 3*rd* order component tracked from the coast-down signal, in time domain (top) and the time-frequency representation using STFT (bottom), which is calculated using the approaches: a) SRCKF_OT, b) VKF_OT.

der components, respectively, that are estimated using SRCKF_OT and VKF_OT. Although in the former case, each amplitude gets non-zero value at the minimum frequency, amplitude estimation and posterior waveform reconstruction are close to the original. For latter approach, in contrast, each amplitude reaches zero value. But the order components are contaminated with noise since reference speed forces the model to get zero value, and hence the estimated amplitude differs from the one of the original components. After waveform reconstruction, however, each order component gets cyclo-stationary nature; that behaviour does not correspond to real one. Mostly, VKF_OT is very sensitive to synchronization between vibration and reference speed signals, particularly, when there are changes among the different operating moments. Instead, SRCKF_OT does not present that issue.

2.5 Order tracking case studies

2.5.1 Case study 1: Ship Driveline

The proposed methodology is also tested on the ship starboard driveline appraising a diesel engine `Caterpillar 3412C`, 12 valves in Vee, 4 strokes-cycle. The engine that provides 2100 *rpm* maximum speed is directly coupled by a gearbox `MG-520`. The database is recorded using a `ACC102` accelerometer with a spectral range of $0 - 8$ *kHz* and 10 *mV/g* sensibility. `NI9234` acquisition card is employed at a 25.6 *kHz* sampling frequency. The accelerometer is located between the gearbox output and the vessel axel, but perpendicularly to the shaft horizontal plane. The recordings, each one lasting one second, are captured under the forward-running operating condition. Since it is not possible to measure the reference shaft speed that is required by VKF_OT, only SRCKF_OT is used, for which the following free parameters are heuristically fixed as, $q_i^a = 10^{-2}$, $q^f = 10^{-13}$ and $r = 10^{-12}$.
Figure 2.13 shows a time-frequency representation of the measured signal and the estimated

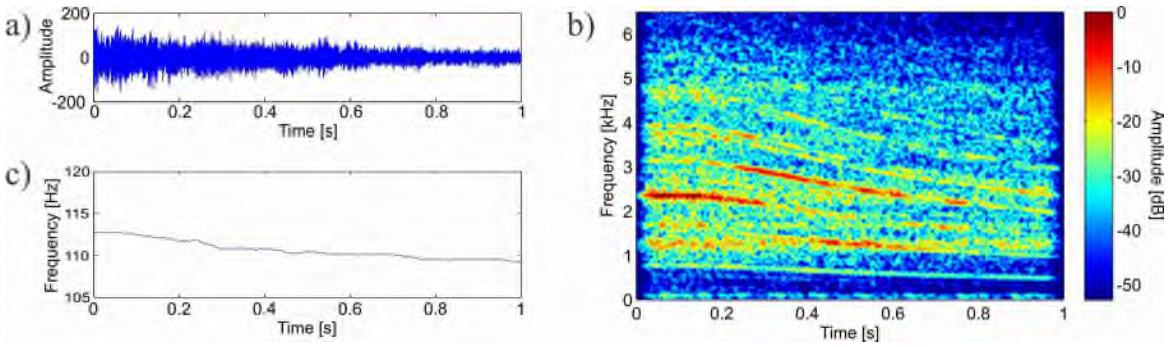

Figure 2.13: Example of an acquired signal from ship driveline under the forward running conditions: (a) in time domain, (b) time-frequency representation using STFT, and (c) estimated instantaneous frequency using SRCKF_OT.

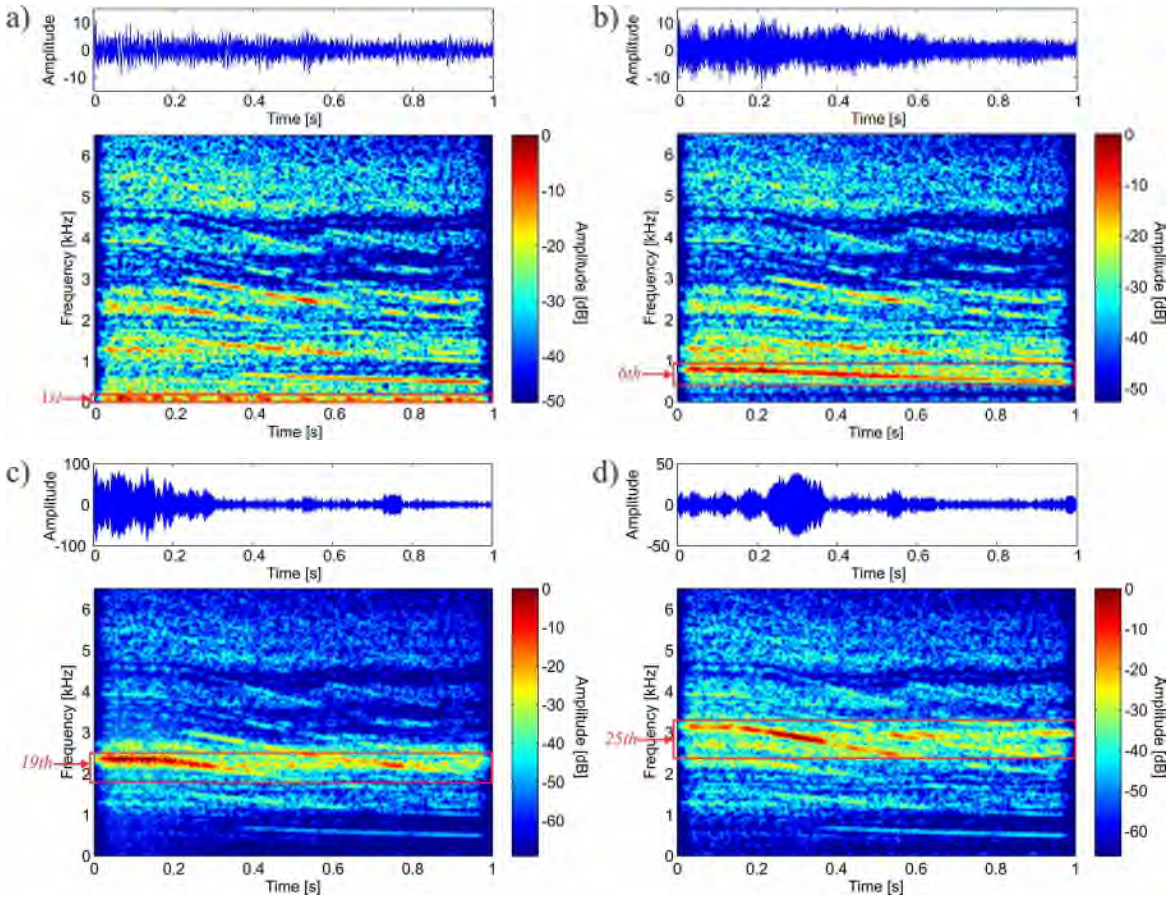

Figure 2.14: Examples of estimated 1*st* (subplot a), 6*th* (b), 19*th* (c), and 25*th* (d) order components, for forward running condition, tracked from ship driveline signal using SRCKF_OT in time domain (top) and its corresponding time-frequency representation using STFT (bottom). The red rectangles show the region of interest in the time-frequency map.

IF using the proposed SRCKF_OT scheme. As seen, the machine speed decreases slowly despite the ship is running forward; that means that the load on the vessel axle is changing. Since the largest the spectral component – the more information they have, only order components with bigger amplitude are extracted. In the concrete case, stronger components relate to the gearbox (e.g. gear-mesh, bearings) and the shaft. As a result, using the above explained procedure in Section 2.2, the estimated and tracked order components for the analyzed signal are $\Gamma = \{1, 6, 8, 10, 11, 13.6, 15, 16.6, 19, 20, 22, 23.4, 25, 26.2, 28.5, 29.6, 30.6, 36, 37.6, 89.4\}$. Time domain (top) and the time-frequency representation (bottom) of the 4 components holding highest amplitudes are shown in Figure 2.14, namely: (a) 1*st*, (b) 6*th*, (c) 19*th*, and (d) 25*th*.

As seen in Figures 2.14(a) and 2.14(b), the most representative components are 1*st* and 6*th*, since they describe the dynamic behavior of the shaft and the output gearbox bearing,

respectively. The first order component shows short impacts associated to the exerted load for a sea movement. An increment in 1*st* component can supply information about an eventual propeller crash into an object, which might generate unbalance or misalignment in the axle. In turn, the 6*th* order component shows a concentrated energy within short time instants; that accumulation distinguishes the output gearbox bearing. Therefore, we hypothesize that fixed amplitude change of the 6*th* order component can supply discriminating information about an eventual fault.

Regarding the 19*th* and 25*th* order components, as seen in Figures 2.14(c) and 2.14(d), they present the highest spectral amplitudes and are derived from the gear-mesh since those components are in constant friction. It must be noted that as the ship speed decreases, the component amplitudes also diminish since there is less friction.

2.5.2 Case study 2: Internal Combustion Engine

In this experiment, the IF is estimated from an IC engine and compared with the tachometer reference to demonstrate that the proposed method can extract the non-stationary behavior associated to variable speed even when the interest component presents a low amplitude. The analyzed mechanical system consists of a 2*L* diesel engine with 4 cylinders in line. The accelerometer recording (provided by Vibration and Acoustic Laboratory from INSA-Lyon) is located on the motor support distribution side in the axial plane, and acquired using 32768*Hz* of sampling frequency lasting 80 seconds approximately. The Fig. 2.15 shows the analyzed signal, where Fig. 2.15(a) depicts in the top part the complete vibration recording and the bottom part the signal downsampled 32 times, reaching 1024*Hz* of sampling frequency. The

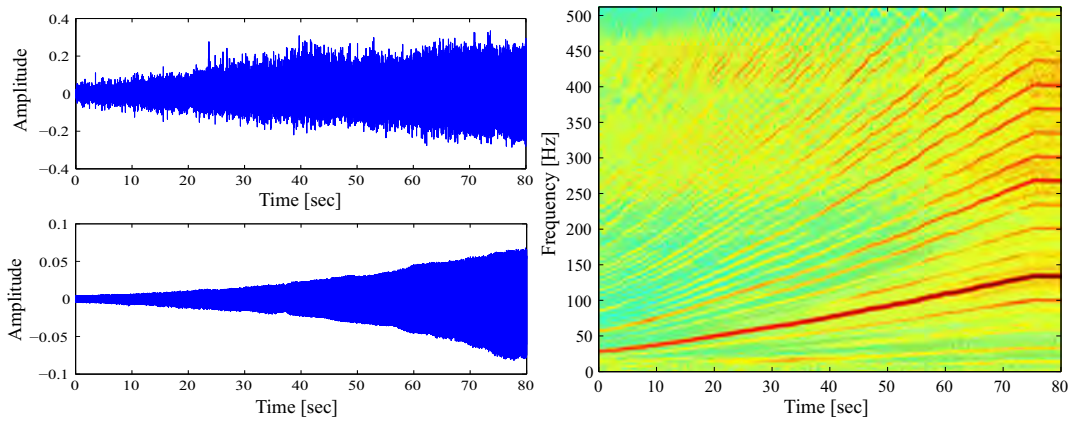

(a) (b)

Figure 2.15: Signal acquired in the IC engine from INSA-LVA laboratory: (a) Signal in time domain complete (top) and a downsampled version 32 times (bottom), and (b) the time-frequency representation of downsampled version.

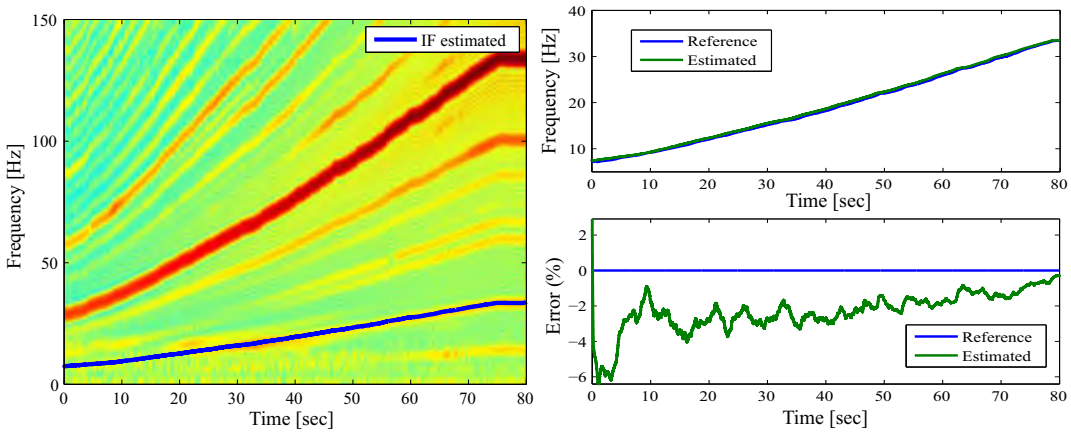

(a) (b)

Figure 2.16: IF estimated by IAS-OT model from INSA-LVA IC engine signal: (a) time-frequency representation highlighting the estimation with blue line, and (b) a comparison with the tachometer reference (top) and its relative error (bottom).

preprocessing applied to the signal is required because the complete signal exhibit a time-varying cyclic behavior that breaks the imposed oscillatory model. However, the downsampled version present a clear harmonic behavior that preserves the continuity condition to estimate the order component amplitude. Fig. 2.15(b) display the time-frequency representation of downsampled version computed by the spectrogram with a 4096 frequency bins, 50% overlapping and a Hamming window of 512 samples. It is worth noting that highest order corresponds with 4 harmonic signal that represents the crankshaft by the number of pistons, and hence, the expected IF has a very low amplitude. Although, the IF extraction by the maxima bins in the spectrogram works successfully taking into account the scalable relationship between the first and forth orders, the proposed approach is applied to obtain multiple order components even when the signal of interest has a low SNR.

Taking into account that the 4*th* order has a biggest amplitude, the harmonic algorithm explained in Section 2.2.1 could not be able of correctly estimating the order components to be tracked. Therefore, the amount of orders is fixed such as $\Gamma = \{1, 2, 3, 4, 5, 6, 7, 8, 9$ $10, 11, 12, 13, 14, 15\}$, and the SRCKF covariances are fixed to $q_i^a = 10^{-5}$, $q^f = 10^{-11}$ and $r = 10^{-12}$. As a result, the IF estimated is displayed in Fig. 2.16(a), and the relative error compared with the tachometer reference (Fig. 2.16(b)) allows to observe that the estimation is closer to measured crankshaft speed, starting in -6% and decreasing to reach error levels under 2%. The high error at the beginning corresponds to the time that the algorithm takes to stabilize the order and IF estimation.

In Fig. 2.17 could be observed the time-frequency representation of the order components lasting from 1*st* to 6*th* in logarithmic scale. It could be appreciated that all order components include information about the 4*th* order due to the model is driven by the spectral component

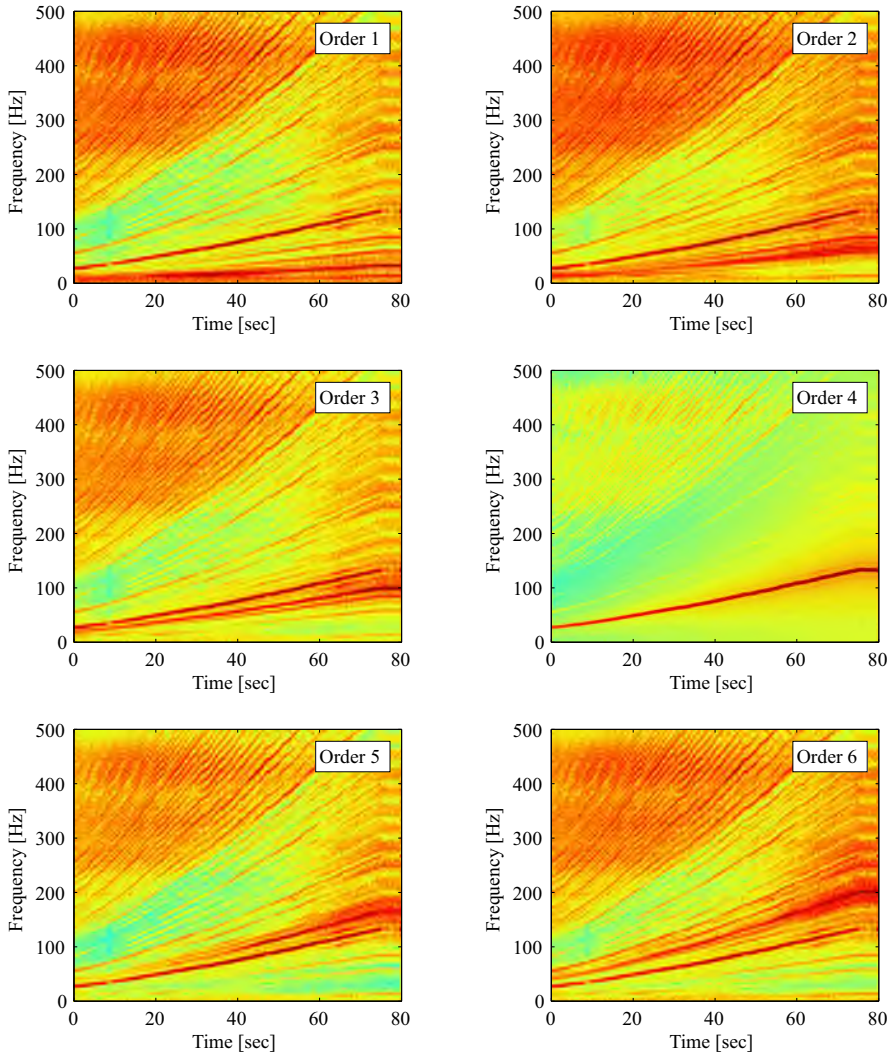

Figure 2.17: Time-frequency representation of six order components estimated from INSA-LVA IC engine signal using the IAS-OT model.

amplitudes. In addition, the spectral information related with orders beyond from 15*th* is distributed into the all estimated components since the model does not separate noise from signal part. However, it is worth noting that the component with highest amplitude on each order corresponds with the estimated component, and its amplitude is much more representative than in the complete signal (see Fig. 2.15(b)). The error introduced by the amount of estimated order components may be reduced if the harmonics set is increased, but the computational cost is increased also. Since the 4*th* order component has the highest amplitude, it is perfectly extracted from the signal, which implies that spectral components with high energy could be estimate with high precision, and the proposed approach is sensitive to the SNR in the sense that between higher is the desired order amplitude, higher is the estimation accuracy.

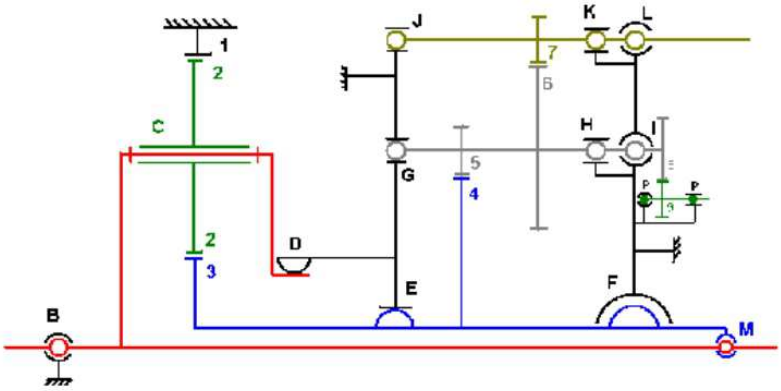

Figure 2.18: Gearbox schematic from CMMNO2014 contest (CMMNO, 2014)

Table 2.3: Amount of each gear teeth presented in Fig. 2.18.

No. Gear	g_1	g_2 (3 planets)	g_3	g_4	g_5	g_6	g_7	g_8	g_9	g_{10}	g_{11}
No. Gear teeth	123	50	21	93	22	120	29	63	23	10	13

2.5.3 Case study 3: Wind Turbine - CMMNO2014 contest

This experiment consisted of estimating the instantaneous speed in *rpm*, or instantaneous frequency in *Hz*, from a wind turbine operating under non-stationary conditions. The information given hereafter, as well as the signal, have been kindly provided by **Maïa Eolis** to solve the contest in the framework of the International conference on Condition Monitoring of Machinery in Non-stationary Operations (CMMNO), December 15-16, 2014 Lyon-France[1]. The provided signal comes from an accelerometer located on the rotor side of the gearbox (high speed shaft) casing in the radial direction, and the speed of the main shaft (also called low speed shaft) is between 13 and 15 *rpm* during the recording. The sampling frequency is 20 *kHz* and the acquisition time is 547 seconds approx. Aiming to understand the planetary gearbox from wind turbine, a kinematic scheme is presented Fig. 2.18. The whole gearbox has three stages: one planetary (pairs 1-2 and 2-3) and two helical parallel stages (pairs 4-5 and 6-7), neglecting the gear pairs 8-9 that are related with the oil bump. Table 2.3 lists the gear parameters of the planetary gear and the fixed-shaft gears. Regarding with the IAS estimation, the red shaft is used as the input shaft (low speed shaft) and the yellow shaft is regarded as high speed shaft. When the input speed of the red shaft is given at any time, it is possible calculating the characteristic frequencies of the planetary gearbox by using the equations listed in Table 2.4, which are deduced from the configuration of planetary and parallel gearboxes. As regards to high speed shaft estimation, f_y, using the expressions listed in

[1]Contest rules link:
http://cmmno2014.sciencesconf.org/conference/cmmno2014/pages/cmmno2014_contest_V2.pdf

Table 2.4: Characteristic frequencies of planetary gearbox

Characteristic frequency	**Expression**
Meshing frequency of gear pairs 1-2 and 2-3	$f_{m12} = f_{m23} = g_1 \cdot f_r$
Rotational frequency of blue shaft	$f_b = \frac{g_1+g_3}{g_3} \cdot f_r$
Meshing frequency of gear pair 4-5	$f_{m45} = g_4 \cdot f_b = g_4 \cdot \frac{g_1+g_3}{g_3} \cdot f_r$
Rotational frequency of grey shaft	$f_{gr} = \frac{g_4}{g_5} \cdot f_b = \frac{g_4}{g_5} \cdot \frac{g_1+g_3}{g_3} \cdot f_r$
Rotational frequency of yellow shaft	$f_y = \frac{g_6}{g_7} \cdot f_{gr} = \frac{g_6}{g_7} \cdot \frac{g_4}{g_5} \cdot \frac{g_1+g_3}{g_3} \cdot f_r$
Meshing frequency of gear pair 6-7	$f_{m67} = g_7 \cdot f_y = g_7 \cdot \frac{g_4}{g_5} \cdot \frac{g_1+g_3}{g_3} \cdot f_r$

where f_r is the rotational frequency of the low speed shaft.

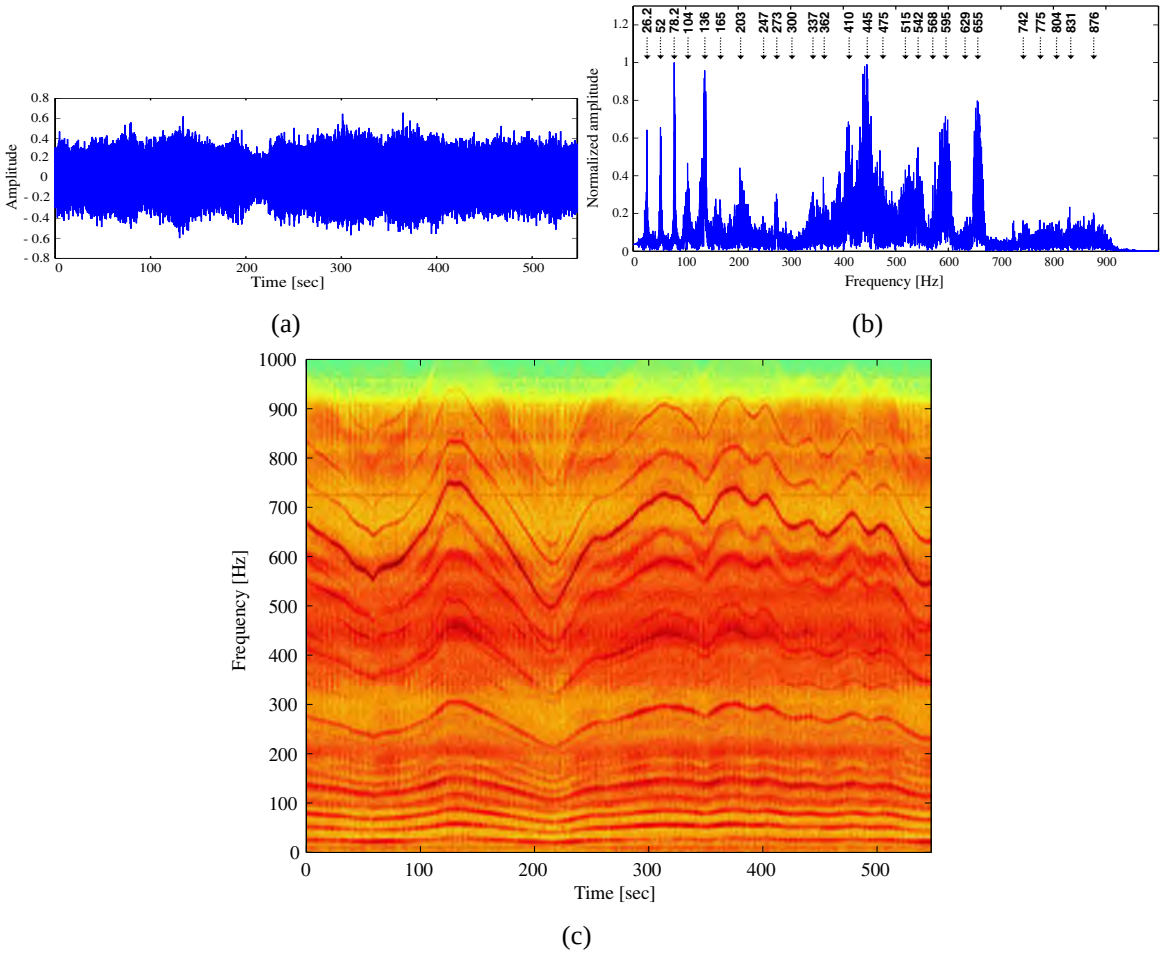

Figure 2.19: Signal provided by CMMNO2014 contest in: (a) time domain, (b) frequency domain, and (c) time-frequency domain.

Table 2.4 are defined the boundaries $[L^f, H^f]$ from the desired IF, obtaining that the reference frequency is between 25.99Hz and 29.98Hz. However, when the testing is carried out, it was found that the minimum boundary must be fixed at 15Hz. In Fig. 2.19, it is shown the pro-

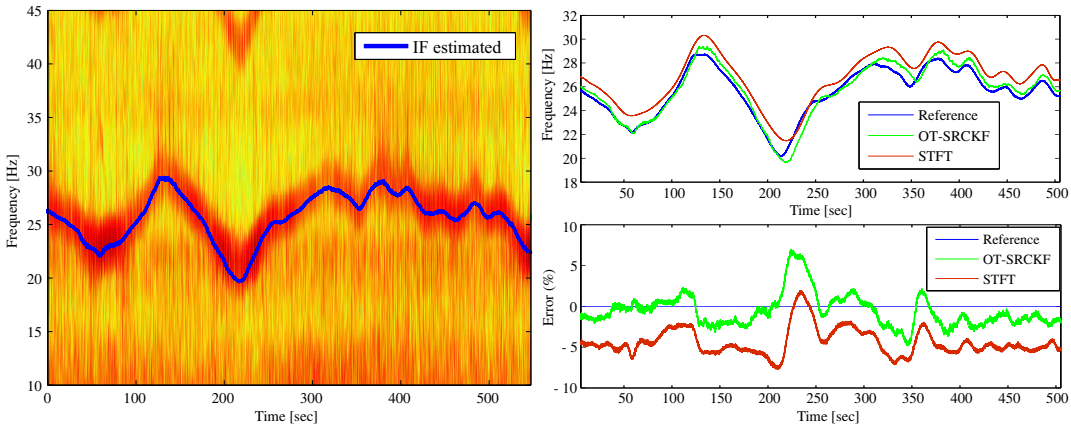

(a) (b)

Figure 2.20: IF estimated by IAS-OT model from CMMNO2014 contest wind turbine signal: (a) time-frequency representation highlighting the estimation with blue line, and (b) a comparison with the tachometer reference and the common (top) and its relative error (bottom).

vided signal, where it is possible to observe the signal in time, frequency and time-frequency domain ((a), (b) and (c) part, respectively). In frequency domain, the harmonics obtained using the harmonic algorithm are marked and showed in the Fourier transform computation from 20 seconds signal segment (see Fig. 2.19(b)). Here, the harmonic 26.2Hz is used as first order, obtaining in total a set Γ of 26 orders. In addition, the SRCKF parameters associated to process and measurement covariances are fixed as $q_i^a = 10^{-3}$, $q^f = 10^{-10}$ and $r = 10^{-11}$. On the time-frequency representation, it is possible to observe that there are two different dynamic behavior in the signal, which are dominated by two different rotating systems, it means that there are harmonics synchronized with the low and high speed shafts, yet there are other harmonics that do not match [1]. As a result, Fig. 2.20 displays the IF estimated using the proposed IAS-OT model. Obtained IF is highlighted with blue line on the time-frequency representation Fig. 2.20(a), where it is possible to see that the estimation match with the high speed shaft, ranging from 20Hz to 30Hz, which confirms the boundaries fixed into the IAS-OT model. A comparison with the tacho reference is shown in Fig. 2.20(b), and besides, the IF estimation (red line) using a traditional method based on time-frequency representation (noted as STFT), which consists in tracking the maxima values in the STFT (Urbanek et al., 2013). It is worth noting that using the aforementioned method was achieved the fifth place in the contest. In that sense, the proposed IAS-OT model allows to improve the result obtained using the based-STFT method, reaching a relative error under ±3% despite the fact that the intervals [220 – 250] and [320 – 350] seconds there are a delay between the reference and the estimated IF. Also, it is important to highlight that the IF estimated

[1] Contest results link:
http://cmmno2014.sciencesconf.org/conference/cmmno2014/pages/PresentationCMMNOcontestwopicts.pdf

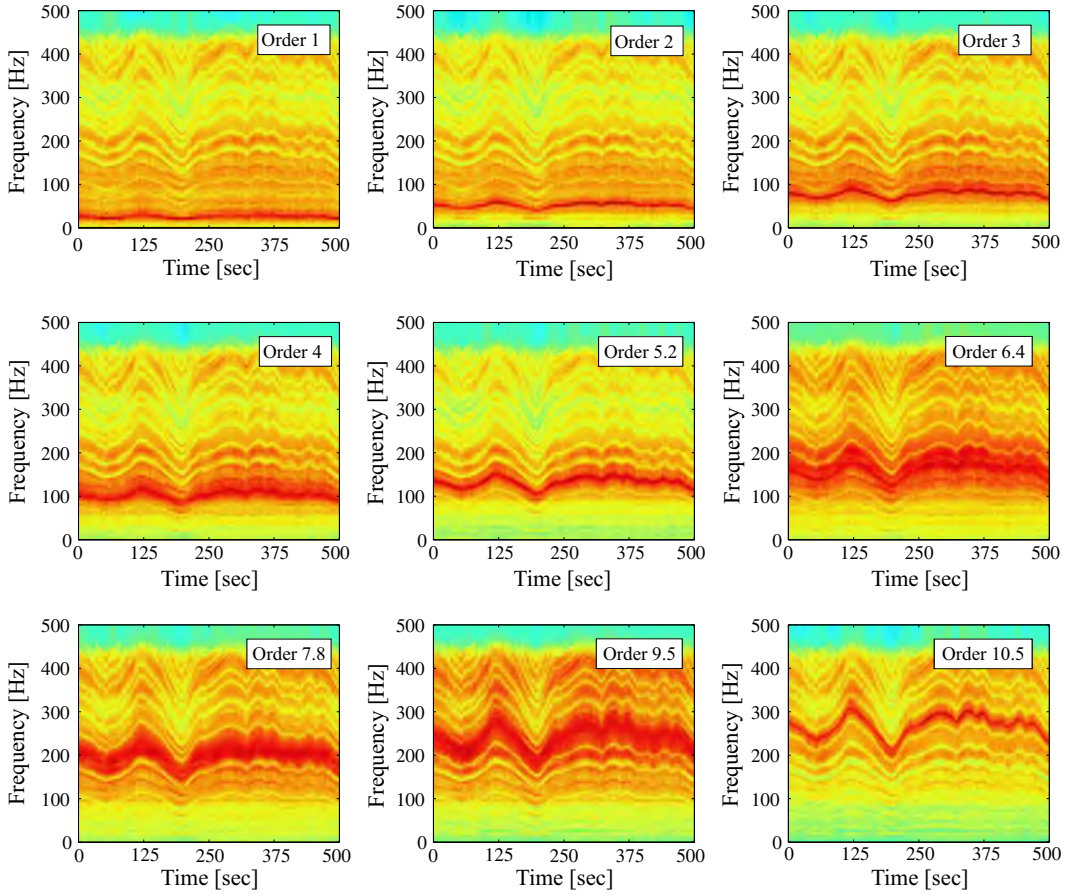

Figure 2.21: Time-frequency representation of nine order components estimated from CMMNO2014 contest wind turbine signal using the IAS-OT model.

by STFT does not match with the reference shaft speed because the maxima tracking was obtained at frequency interval $[500, 750]Hz$ and the scaling factor was not enough accurate. Finally, a time-frequency representation of nine order components is displayed in Fig. 2.21, where it is important to notice that each plot is presented in logarithmic scale, therefore, the filtering provided by the proposed method allows to extract the non-stationary components, even if the order components are not integer multiple from $1st$ order. Similar to case study presented in Section 2.5.2, there are components that comprise noise around the tracked order component, nonetheless, the fact that the order amplitude holds during all signal length, improving the filtering precision of the proposed IAS-OT model.

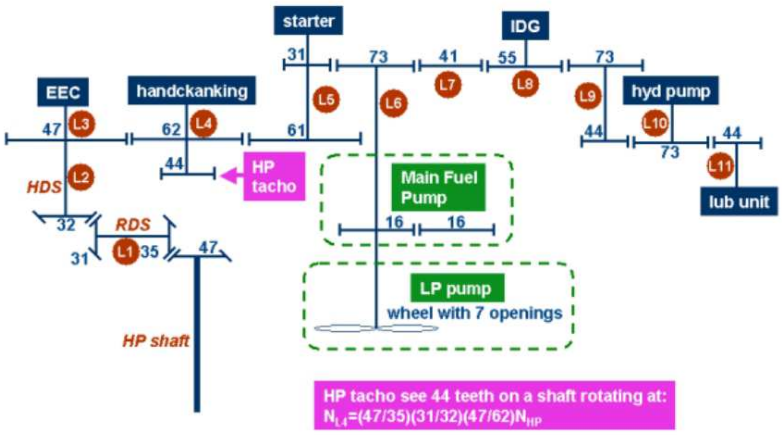

Figure 2.22: Gearbox schematic from SAFRAN contest (SAFRAN, 2015).

2.5.4 Case study 4: Gearbox - SAFRAN SURVEILLANCE 8 contest

This experiment consisted of estimating the instantaneous speed in *rpm*, or instantaneous frequency in *Hz*, from a gearbox operating under non-stationary conditions. The information given hereafter, as well as the signal, have been kindly provided by **SAFRAN** to solve the contest in the framework of the International conference Surveillance 8, October 20-21, 2015, Roanne-France [2].

The contest includes two independent exercises, the signal on each exercise is under non-stationary conditions, i.e. coast-down and start-up operating conditions (exercise 1 and 2 respectively). In this case study just the first exercise was solved using the IAS-OT model, and the results are presented here. The provided vibration signal has a 50*kHz* of sampling frequency and 3.4 minutes of time acquisition. Fig. 2.22 shows the kinematic scheme of the gearbox, where it is possible identifying the transmission lines ($L1 - L11$), and the number of gear teeth, as well as the relationship between different lines in order and frequency terms (Fig. 2.23). For sake of simplicity, the signal exhibits a visible harmonics from HP shaft, and the objective is to recover the non-stationary rotation speed of HP shaft (N2) from a vibration signal mounted on the gearbox casing. A visual inspection of vibration signal is presented in Fig. 2.24, where it is displayed the gearbox signal under coast-down operating condition both in time, frequency and time-frequency domains. When the signal is decimated to 25*kHz* (Fig. 2.24(c)), two different dynamics that cross between them could be distinguished, yet the signal is downsampled 25 times obtaining a clear harmonic patterns that are related to required shaft speed. Nonetheless, there is no a spectral component around 166.67*Hz* (i.e. 10000*rpm*) that presents a visible harmonics. Therefore, in spite of the information included

[2] Contest rules link:
http://surveillance8.sciencesconf.org/resource/page/id/17

N2 speed (rpm)		line 1		line 2		line 3		N2 tacho visu : 44 teeth	line 4	line 5		line 6		line 7		line 8		line 9		line 10		line 11
10000		HP shaft		RDS		Horizontal Drive Shaft		EEC alternator		handcranking		starter		fuel pump		intermediate		IDG		intermediate		hydro. pump		lubrication unit
		aval		amont	aval	amont	aval	amont	aval	amont	aval	amont	aval	amont	aval	amont	aval	amont	aval	amont	aval	amont	aval	amont
number of teeth		47		35	31	32	47	47	47	62	62	61	31	73	73	41	41	55	55	73	44	73	73	44
rotating speed (rpm)		10000		13429		13009		13009		9862		10023		4256		7579		5649		4256		2566		4256
F 1 tooth (Hz)		167		224	224	217	217	217	217	164	164	167	167	71	71	126	126	94	94	71	71	43	43	71
F 1 tooth (N2)		1.0000		1.3429	1.3429	1.3009	1.3009	1.3009	1.3009	0.9862	0.9862	1.0023	1.0023	0.4256	0.4256	0.7579	0.7579	0.5649	0.5649	0.4256	0.4256	0.2566	0.2566	0.4256
gear mesh frequency (Hz)		7833			6938		10190		10190		10190		5179		5179		5179		5179		3121		3121	
gear mesh (mult N2)		47.0000			41.6286		61.1420		61.1420		61.1420		31.0721		31.0721		31.0721		31.0721		18.7284		18.7284	
Fcoincidence (Hz)		4.8			7.0		216.8		3.5		2.7		2.3		1.7		2.3		1.3		1.0		1.0	

Figure 2.23: Characteristic frequencies referenced to HP shaft rotating speed (N2) (SAFRAN, 2015).

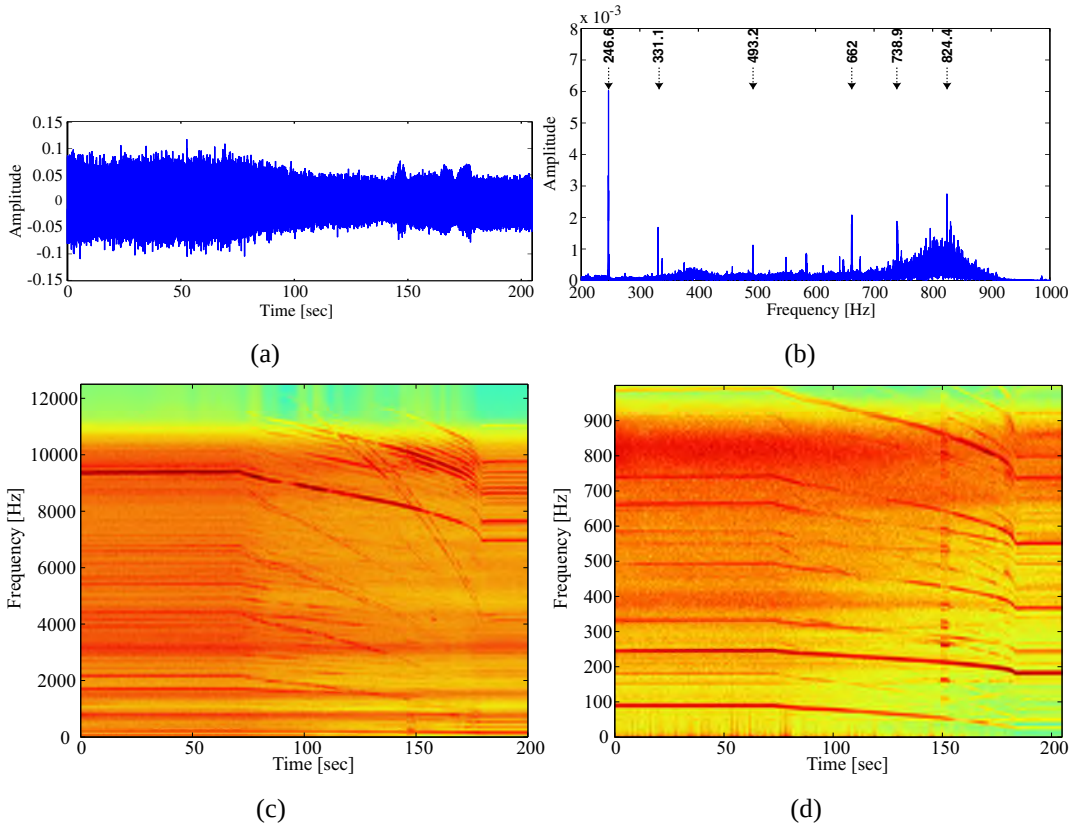

Figure 2.24: Provided gearbox signal by SAFRAN contest in: (a) time domain, (b) frequency domain, and time-frequency domain from downsampled signal (c) 2 and (d) 25 times.

in Fig. 2.23 allows to infer that expected HP shaft component must appears around 166.67Hz (1st order), inspecting the tacho signal measured on line 4, and given for solving the exercise 2, shows that the $L4$ rotational speed ranging from 181Hz to 243Hz. Therefore, taking into account that the relationship between $L4$ and $L1$ (HP shaft speed) is 1.014, it is assumed that the desired shaft speed is around 183Hz and 246Hz. Then, the IAS-OT model boundaries are fixed $L^f = 180$ and $H^f = 250$, and it is not relevant if the operating condition is start-up of coast-down, due to the required useful information is to define an approximated range where the expected IF is changing. The orders to be tracked into the proposed model are estimated

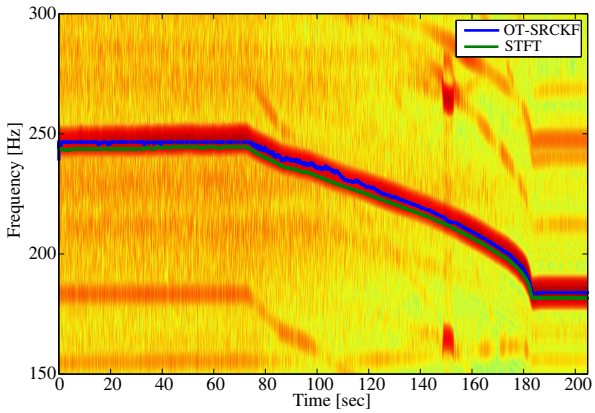

Figure 2.25: Time-frequency of SAFRAN contest gearbox signal (exercise 1) and the estimated IF using the IAS-OT model (blue line).

using the harmonic algorithm (Section 2.2.1) from a 20 seconds signal segment, obtaining the harmonics showed in Fig. 2.24(b). As regards to properly fix the first order component, a high-pass FIR filter is applied, because there is a component around $100Hz$ that is a sub-harmonic of desired component, and the proposed model requires that the first component in the signal corresponds with the first order. In that sense, a total of 6 order components are needed to estimating the IF associated to HP shaft speed. As a result, adjusting the SRCKF parameters to $q_i^a = 10^{-7}$, $q^f = 10^{-11}$ and $r = 10^{-12}$, it is obtained the IF showed in Fig. 2.25. The blue line indicates the IF estimated by the proposed method, and green line corresponds to estimation using the based-STFT method ((Urbanek et al., 2013)). It is possible to see that IF extracted with SRCKF_OT method is centered with respect to spectral component (red band), whereas the based-STFT method obtains a shifted IF which could be generated by a bias introduced when the interpolation of the estimated IF is carried out. Nonetheless, it is worth noting that both methods extracting correctly the IF structure, but the proposed scheme is more accurate, taking into account that the scaling factor in the maxima tracking must be fixed. Other aspect to highlight is that the estimated IF allows us achieve the third place in the contest, yet including the exercise 2 answer. Fig. 2.26 shows the time-frequency representation of the six extracted order components in logarithmic scale. It is important to highlight that first order is extracted perfectly, it means, without spurious noise, whereas the other components are contaminated with low power noise.

2.6 Discussion

The developed experiments allow formulating several findings about the considered OT schemes. So, the following advantages and drawbacks of the proposed scheme are highlighted:

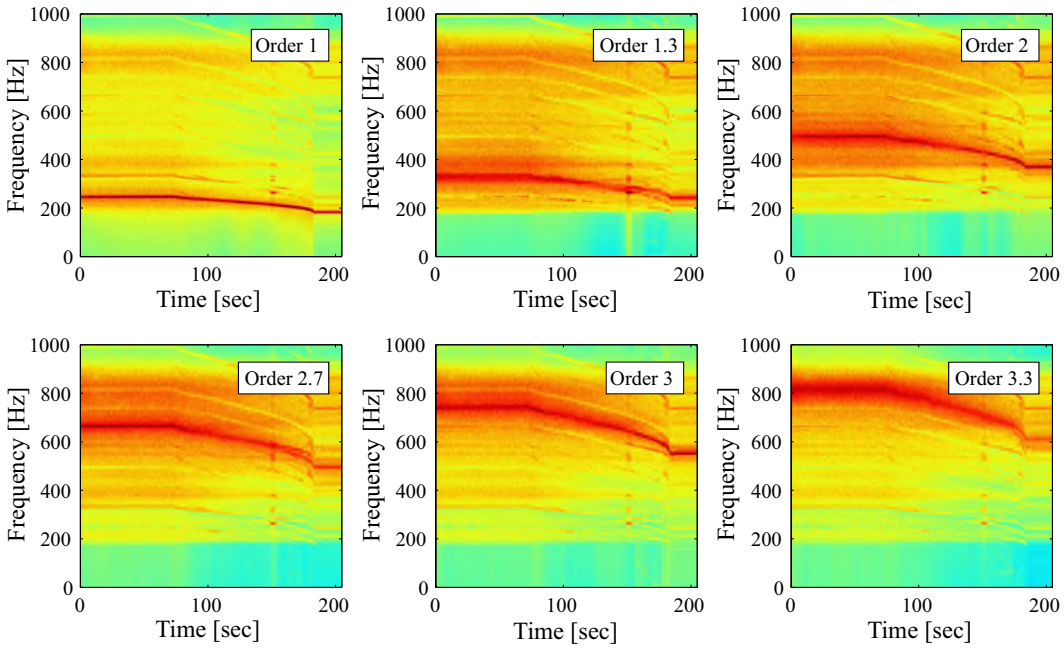

Figure 2.26: Time-frequency representation of six order components estimated from SAFRAN contest gearbox signal using the IAS-OT model.

– The proposed nonlinear model for solving the OT problem can handle vibration signals with multiple oscillatory components represented through several order components. Yet, the approach has a trade-off between the model order ($2K+1$, being K the number of components to be tracked) and the computational cost associated with parameter estimation. Moreover, as K increases the precision also improves, but at the same time, the computing burden grows since the amount of iterations becomes bigger. In the concrete case, K can over exceed hundred components. To cope with this Kalman filtering issue, estimation is carried out just over the most relevant order components. So, the proposed methodology downsizes to the needed variable amount (more less than K) such that it provides enough precision of the respective reconstructed order components.

– However, the proposed OT scheme represents both the signal and noise energy as state variables, and therefore the estimation performance decreases inasmuch as obtained order components from vibration signal are corrupted. To achieve the needed estimation accuracy, particularly, ten order components are used in test rig experiment, as seen in Figures 2.10, 2.11, and 2.12. Likewise, since the noise level is higher, the amount of order components increases to 20 in the ship driveline application (Figure 2.14). Besides, the IF estimation also depends on the amount of spectral components to be tracked, but the noise influence is more focused on amplitude estimation according to the selected model covariance, $\boldsymbol{Q}$. Here, it is worth noting that the tracked

order components could be estimated using the algorithm explained in Section 2.2.1, but when the signal comprises an order components with considerable amplitude, as in the case studies related with both contest.

– Since the IAS-OT model is solved by Kalman filtering, the process and measurement covariances are parameters that strongly affect the estimation accuracy, therefore, it is suggested to utilize a grid of parameters comprising the following values: *i)* $q^a \in [10^-3, 10^-6]$, *ii)* $q^f \in [10^-6, 10^-11]$, and *iii)* $r = q^f \cdot 10^-1$. Starting with those parameter values reduce the possibility to find a correct estimation both order components and IF.

In addition, comparison between SRCKF_OT and VKF_OT brings the following observations:

– In terms of the achieved estimation performance, compared models turn to be adequate for all considered databases. Therefore, the obtained outcomes in simulated experiment (see Table 2.2) allow inferring that the waveform reconstruction using SRCKF_OT gets a lower error, which is reduced to half in average, for each estimated order component. Error reduction can be explained since the proposed scheme does not require any synchronization between vibration and tacho signals, while VKF_OT scheme does. In contrast, amplitude estimation of each order component shows that VKF_OT supplies better approximation to the original components because it modulates each component using the amplitude parameter, while the proposed scheme is just based on the frequency parameter. Yet, when experimental data are used, the achieved performance has no meaningful differences between compared approaches, i.e., both schemes are satisfactory. Therefore, comparison must be rendered in a graphical way. Generally, the VKF_OT scheme needs a reference signal coming from the rotation speed of the machine. Instead, the SRCKF_OT does not require any synchronization and is able to estimate the frequency associated with the first component as well as other components that might not be integer multiples of the rotation speed, such as resonances (Figure 2.9).

– As seen in Figures 2.3, 2.4, and 2.5 (theoretical experiment), as well as in Figures 2.10, 2.11, and 2.12 (test rig experiment), the VKF_OT approach performs as an amplitude modulation scheme, carrying out a cumulative integration of the angular velocity to get the forming signal phase of each component (Pan and Lin, 2006), and hence, this approach presents a high estimation error when reference signal vanishes at all. In contrast, in the proposed scheme, each component is estimated from its own waveform and then the amplitude is calculated from each in-phase and quadrature component; this allows to track more complex dynamic systems.

– As shown in Table 2.2, the proposed scheme requires larger component amount K to perform more precise estimation of each component. Instead, the VKF_OT can estimate the desired component, provided the reference speed signal. However, to get similar accuracy, the latter scheme requires fine synchronization of the vibration signal along with the reference. In the case of the closed-order component estimation, VKF_OT is more accurate in determining the amplitude, but the waveform reconstruction error is worse when the order component is estimated since there is a phase delay between the base signal and the modulation performed. The same behavior can be seen in Figures 2.10, 2.11, and 2.12. On the other hand, SRCKF_OT performs more precise estimation because it preserves the waveform and amplitude at current time, despite the noise influence; this fact is an advantage in real-world applications.

– From the carried out test rig analysis two aspects are to be emphasized: first, the proposed scheme performs suitable estimation, mainly, since it does not require any reference shaft speed measurement. Rather, there are three parameters associated to Kalman filter recursion that must be tuned. In case of the VKF_OT, there are only two parameters to be fixed. Second, the estimation stability in SRCKF_OT is better than in the VKF_OT case since for each recording a reference shaft speed measurement is needed.

3 Fault identification by novelty detection

Nowadays, condition monitoring of rotating machinery is becoming increasingly important for the industry because it allows reducing accidental damages and improving the machine performance at the same time. This tool mainly relies on the adequate evaluation of the machine health or state, employing a set of measurements (called Condition-based Maintenance – CBM). Nevertheless, most of the real-world machinery operate unique pieces, which are not suitable for inducing faults, making unfeasible to collect useful data from undamaged machine conditions. Therefore, training datasets are unbalanced, presenting enough information just about normal class. Regarding this matter, the *novelty detection* techniques had been developed that aim at inferring or modeling the undiscovered or missing data.

According to the extensive review in Pimentel et al. (2014), the novelty detection methods (also termed one-class classifiers OCC) can be constructed using generative or discriminative models. In either case, non-normal classes can be built based on several representations: Distance-based, Probabilistic, heuristic, subspace-based, or based on information-theoretic learning. Nonetheless, extraction of a representative feature set must be carried out accurately to provide robust performance on test data. To this end, feature extraction achieves a trade-off that maximizes the exclusion of novel samples while minimizes the exclusion of known samples.

For training of CBM systems, data can be measured by several principles: vibration, acoustic emission, and temperature signals, among others. However, the vibration principle is more frequently used because of its low cost and high performance usually provided (Randall, 2011). Furthermore, a set of statistical features has been already proposed for extracting a set of discriminating features from vibration signals (Lei et al., 2010; Villa et al., 2012; Lei et al., 2012; Wang, 2016). However, several machine operations often lead to non-stationary signals due to the dynamic behavior of the machinery excitations, resulting in time-varying operating conditions. Therefore, the development of signal analysis methods suited to extracting the time-varying features from non-stationary signals has become increasingly relevant for machinery fault diagnosis (Feng et al., 2013). To obtain valuable information from non-stationary signals, several principles of feature extraction have been suggested for diagnosis of machinery health conditions (Worden et al., 2011; Goyal and Pabla, 2015). Where it is possible to find stochastic models for time series (like regressive models (Langone et al.,

2015), Markov models (Zhou et al., 2015)), linear time-varying decompositions (harmonic analysis (Cardona-Morales et al., 2014; Heo and joon Kim, 2015), time-frequency analysis (Wang et al., 2015), time-scale analysis (Chen et al., 2016)) , non-linear time-varying decompositions (empirical mode analysis (Lu et al., 2015), complex analysis (Caesarendra et al., 2015)), among others.

Although the implicit trade-off between the time and frequency resolution of the analysis may degrade the performance of time-frequency representation (TFR), its use remains very desirable for machinery diagnostics. The major advantages of TFR are its fast implementation and the provided physically meaningful interpretation as suggested in Sejdic et al. (2009), where different TFR methods are discussed to discriminate test rig faults. Nevertheless, one aspect that may jeopardize the use of linear time-varying decompositions for condition monitoring is the high dimension of the extracted feature set, extremely increasing the computational load of the CBM as a whole notably (Cardona Morales et al., 2013).

In this chapter, a CBM methodology for non-stationary operating conditions is introduced that relies on a set of the time-varying narrow-band features extracted from order tracking approach presented in Chapter 2, aiming to encode the non-stationary behavior of the acquired vibration signals. The key point here is conceiving the order components like dynamic features, and then, estimating several statistical parameters over those features to carry out the dimension reduction of the input training set as discussed in Lu et al. (2015). Another approach to properly characterize each narrow-band component is employing similarity measures as is presented in Sierra-Alonso et al. (2014). Particularly, the multi-dimensional outlier detection problem is solved using two different data description classifiers, including the *Support Vector Data Description* (SVDD) as OCC method that is assumed to accomplish a spherical boundary around the data set by avoiding the estimation of the data density (Tax and Duin, 2004; Cha et al., 2014). The other data description classifier is based on the estimation of the probability distribution function, assuming that the boundary can be modeled by a Gaussian distribution, so-called *Gaussian Distribution One-Class Classifier* (GDOCC) (Tax, 2011).

The proposed CBM methodology comprises two different OCC schemes under different points of view (Section 3.3). Firstly, a traditional scheme, similar to Ding et al. (2015); Lei et al. (2015), where one class encloses the all undamaged data, and another class is compounded from different types of machine faults, either unbalance and misalignment or bearing faults. Moreover, secondly, a novel scheme based on blind label assignment where the dynamic features (i.e. order components) are dealt like pseudo-observations taking into account that each order component inherits the properties of the complete signal. Then, a feature set is built with all undamaged order components to train the classifier algorithms, and the order components estimated from faulty signals are assessed to identify a spectral region where the abnormal condition appears. In order to validate the proposed methodology, several experiments are shown in Sections 3.4 and 3.5 using three different datasets.

First, a dataset collected on a test rig for undamaged, unbalanced and misaligned instances under speed-varying machine conditions (start-up and coast-down). Second, a set of signals acquired on a test rig including undamaged and bearing faults under constant speed. Finally, a dataset composed by undamaged and bearing faults under coast-down operating machine condition.

3.1 Feature estimation

With the purpose of separating the information of spectral sub-bands, the filter bank methods (FBM) decompose bandwidth-limited signals into a set of narrow-band components. Thus, a given signal $y(t) \in \mathbb{R}(T)$ that has a finite bandwidth ΔF (with $F = [0, 1/2\Delta t]$, being $1/\Delta t$ the sampling frequency) is decomposed into $K \in \mathbb{R}^+$ narrow-band components $\boldsymbol{x} = \{x_k(t) : k \in K\}$ so that each one has a bandwidth ΔF_k such that $F_k \subseteq F$.
In that sense, the order tracking model (OT) proposed in Section 2.1 decomposes the signal $y(t)$ in a set of order components $x_k(t) \in \mathbb{R}(T)$ such that the (2.1) can be written as follows:

$$y(t) = \sum_{k=1}^{K} x_k(t), \forall t \in T \tag{3.1}$$

where each order component is $x_k(t) = a_k(t)\cos(k\omega(t) + \varphi_k(t))$, being $a_k(t)$ the order amplitude, $k\omega(t)$ the *k-th* harmonic of the fundamental rotational frequency $\omega(t)$ and $\varphi_k(t)$ the order phase. It is worth noting that depending on the amount of K order components extracted, it is feasible that $x_k(t)$ could be associated with a mono-component signal (i.e. the spectral information is contained in a singular frequency $k\omega(t)$, but considering that in the most of cases K is lower than the actual harmonics in $y(t)$, each $x_k(t)$ has a limited-bandwidth ΔF_k.
Due to the narrow-band components comprises much information about the machine condition, it is necessary to estimate a set of features that may be fed into the classification scheme. In that sense, two different type of features are computed from each order component including the statistical and similarity characteristics.

3.1.1 Features based on statistics

To compute a commonly state-of-the-art feature set, used in Lei et al. (2010); Villa et al. (2012); Wang (2016), both each single recording ($y_i(t)$) and each dynamic feature ($x_{i,k}(t)$) is represented by a set of scalar-valued time–invariant features. Specifically, the suggested statistical features appraises two sets: set 1 having 11 features, $\{\chi_1, \ldots, \chi_{11}\}$, which are proposed to be estimated directly from the time series $\psi(t)$, that denotes either the raw signal $y_i(t)$ or an order component $x_{i,k}(t)$; set 2 with 13 features, $\{\tilde{\chi}_1, \ldots, \tilde{\chi}_{13}\}$, which are estimated from the frequency domain computed by the Fourier Transform of the time series, $\Psi(f) = \mathcal{F}\{\psi(t)\}$. Both sets are shown in Table 3.1, where f_i denotes the i-th frequency value, and in this

Table 3.1: Extracted statistical features in time and frequency domains, after Lei et al. (2008, 2010).

$\chi_1 = \boldsymbol{E}\{\psi(t) : \forall t \in T\}$	$\tilde{\chi}_1 = \boldsymbol{E}\{\Psi(f) : \forall f \in F\}$
$\chi_2 = \text{std}(\psi(t))$	$\tilde{\chi}_2 = \text{var}(\Psi(f))$
$\chi_3 = \text{rms}(\psi(t))$	$\tilde{\chi}_3 = \text{rms}(\Psi(f))$
$\chi_4 = \text{skew}(\psi(t))$	$\tilde{\chi}_4 = \text{skew}(\Psi(f))$
$\chi_5 = \text{kurt}(\psi(t))$	$\tilde{\chi}_5 = \text{kur}(\Psi(f))$
$\chi_6 = \left(\boldsymbol{E}\left\{\sqrt{\lvert\psi(t)\rvert}\right\}\right)^2$	$\tilde{\chi}_6 = \boldsymbol{E}\{f_i\Psi(f)\} / \boldsymbol{E}\{\Psi(f)\}$
$\chi_7 = \max_t \lvert\psi(t)\rvert$	$\tilde{\chi}_7 = \sqrt{\boldsymbol{E}\{(f_i - \tilde{\chi}_6)^2\Psi(f)\}}$
$\chi_8 = \chi_7/\chi_3$	$\tilde{\chi}_8 = \sqrt{\boldsymbol{E}\left\{f_i^4\Psi(f)\right\} / \boldsymbol{E}\left\{f_i^2\Psi(f)\right\}}$
$\chi_9 = \chi_7/\chi_6$	$\tilde{\chi}_9 = \boldsymbol{E}\left\{f_i^4\Psi(f)\right\} / \sqrt{\boldsymbol{E}\{\Psi(f)\}\,\boldsymbol{E}\left\{f_i^4\Psi(f)\right\}}$
$\chi_{10} = \chi_6/\boldsymbol{E}\{\lvert\psi(t)\rvert\}$	$\tilde{\chi}_{10} = \tilde{\chi}_7/\tilde{\chi}_6$
$\chi_{11} = \chi_7/\boldsymbol{E}\{\lvert\psi(t)\rvert\}$	$\tilde{\chi}_{11} = \boldsymbol{E}\left\{(f_i - \tilde{\chi}_6)^3\Psi(f)\right\} / \tilde{\chi}_7^3$
	$\tilde{\chi}_{12} = \boldsymbol{E}\left\{(f_i - \tilde{\chi}_6)^4\Psi(f)\right\} / \tilde{\chi}_7^4$
	$\tilde{\chi}_{13} = \boldsymbol{E}\left\{(f_i - \tilde{\chi}_6)^{1/2}\Psi(f)\right\} / \tilde{\chi}_7^{1/2}$

study, both sets are merged into a single statistical feature set (SFS). An optional dimension reduction is also considered by using Principal Component Analysis (SFS-PCA).
In Table 3.1, $\boldsymbol{E}\{\cdot\}$ stands for the expectation operator, and the set of features $\{\chi_2, \ldots, \chi_5\}$ are: the standard deviation, std$(\cdot)$; the root mean square (RMS) value, rms$(\cdot)$; the skewness, skew$(\cdot)$; and the kurtosis, kurt$(\cdot)$; all of them providing a physical interpretation in terms of vibration severity levels. In addition, other statistical features as χ_9, χ_{10} and $\tilde{\chi}_6$ are the crest factor, the shape factor and the frequency center, respectively.

3.1.2 Features based on similarity measures

With the aim of improving the discriminating ability of the feature set, it is computed a measure of similarity between the input signal $y(t)$ and each extracted k-the narrow-band component, $x_k(t) \in \mathbb{R}(T)$, quantifying their mutual statistical dependence. Taking into account the available FBM representation, it is measured the statistical dependence through the *cross-correlation spectral density (CCSD)* between $\{y(t), x_k(t)\}$ that depicts the distribution of signal content over the frequency domain, defined as below:

$$S_{yx_k}(\omega) = \left| \int_T \int_T y(\tau) x_k(t+\tau) d\tau \exp(-j\omega t) dt \right|^2 \tag{3.2}$$

where $\omega = 2\pi f$. Derived from the spectral measure in (3.2), it could be consider the following generalizing values of mutual statistical dependence:

– *Pearson's correlation coefficient (PCC)*, $\rho_{y,x_k} \in \mathbb{R}[-1, 1]$, that is a straightforward way

to quantify the linear relationship of dependence as bellow:

$$\rho_{y,x_k} = \boldsymbol{E}\left\{S_{yx_k}(\omega) : \forall\omega\in F_k\right\}/\sigma_y\sigma_{x_k} \tag{3.3}$$

where $\sigma^2_{\xi}=(2\pi)^{-1}\int_{F_k}|S_{\xi}(\omega)|^2 d\omega$ is the variance. Note that both $y(t)$ and $x_k(t)$ are assumed zero-mean values.

– *Cumulative spectral density index (CSDI)* introduced as follows:

$$\varrho_{y,x_k} = \boldsymbol{E}\left\{\int_{-\infty}^{\omega} S_{yx_k}(\widetilde{\omega})d\widetilde{\omega} : \forall\omega\in F_k\right\},\ \varrho_{y,x_k}\in\mathbb{R}^+ \tag{3.4}$$

It is worth noting that the higher the values of ρ_{y,x_k} and ϱ_{y,x_k}, the higher statistical association between variables.

3.2 One-class data inference

Based on the optimal signal detection that infers whether the damage is present, different approaches to distinguish one class from the rest of the feature data space, $\boldsymbol{Z}\in\mathbb{R}^{N\times p}$, had been developed, (being p the data dimension and N the number of available objects). Particularly, the measured data space is related to just one of the classes (termed *target* and noted as $\boldsymbol{Z}_{tr}\subseteq\boldsymbol{Z}$) that can be properly characterized and compactly clustered, in such a way, as to guarantee the discrimination of other possible objects (that is, *outlier* class from which no measurements are available) distributed outside of the target class. So, to hold the target class within concrete boundaries, two concepts are introduced: *i*) the distance, $d(\boldsymbol{z}_i)\in\mathbb{R}^+$, that measures the closeness of an object $\{\boldsymbol{z}_i : i=1,\ldots,N;\ \boldsymbol{z}_i\in\boldsymbol{Z}\}$ to the target class, and *ii*) the threshold $\theta\in\mathbb{R}^+$ on this distance, that fixes the decision boundary of the target class, that is (Tax, 2011):

$$\begin{cases} d(\boldsymbol{z}_i)<\theta, & \boldsymbol{z}_i\rightarrow\text{target class}\\ d(\boldsymbol{z}_i)>\theta, & \boldsymbol{z}_i\rightarrow\text{non-target class}\end{cases} \tag{3.5}$$

The definition of the adequate classification boundary around target class remains the most challenging issue. Moreover, the threshold θ should allow as many objects as possible from the target class, minimizing the chance of accepting non-target (or outlier) objects at the same time (Khan and Madden, 2010). The most important feature of OCC, as is discussed in (Tax, 2011), is the trade-off between the fraction of the target class that is accepted, t_p, and the fraction of outliers that is rejected, f_n, or the equivalent trade-off between the error of the first and the second types, ε_I and ε_{II}, respectively (see Table 3.2). In OCC problems, the errors are commonly denote in terms of the false positive f_p (outlier accepted) and the true

Table 3.2: Types of classification error in the OCC problem. In multiclass problem the errors are noted as type I error (ε_I) and type II error (ε_{II}).

		True class label	
		target	outlier
Assigned label	target	true positive (t_p) target accepted	false positive (f_p) outlier accepted (ε_I)
	outlier	false negative (f_n) target rejected (ε_{II})	true negative (t_n) outlier rejected

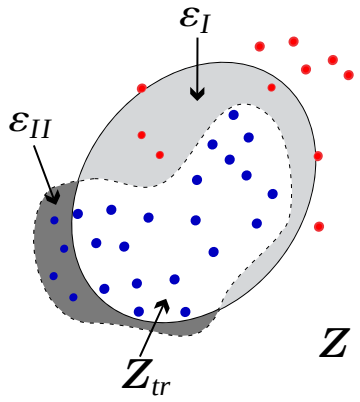

Figure 3.1: Regions in OCC. A spherical shaped one-class boundary is trained using the training set (blue dots). The outliers are represented by red dots. The gray areas represent the error of the first and second types.

negative t_n (target rejected). The general setup is shown in Fig. 3.1. The circular boundary is the data description which should describe the data, however, it makes some errors: a part of the target data are rejected and some outliers are accepted. Increasing the volume of the data description aiming to decrease the error ε_{II}, will automatically increase the number of accepted outliers, and hence, increase the error ε_I. In practice, the employed distance can be implemented by the simple Euclidean or even more complex statistics-based distances. In that sense, the distances are more robust when it is impose a model to the OCC that allows to provide a highly dense volume of the decision hyper-sphere. Specifically for implementing the OCC, the Gaussian distribution classifier (using Mahanalobis distance) and the Support Vector Data Description (using kernel based square distance) are explained below.

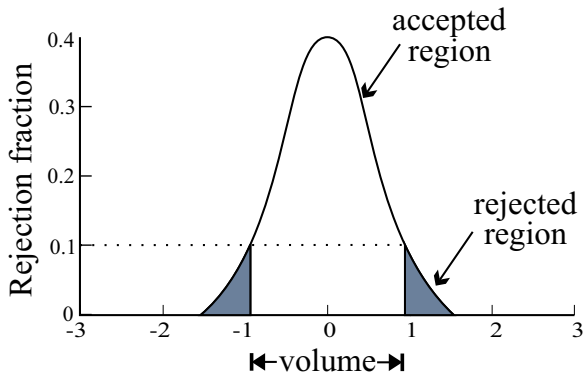

Figure 3.2: Threshold on a 1-dimensional Gaussian distribution.

3.2.1 Gaussian-Distribution One-Class Classifier - *GDOCC*

The Gaussian-distribution-based OCC fits a p-dimensional multivariate normal distribution (e.g. see Fig. 3.2) to the data set (Bishop, 1995):

$$\Xi(\boldsymbol{z}) = \frac{1}{(2\pi)^{p/2}\det(\boldsymbol{\Sigma})^{1/2}} \exp\left(-\frac{1}{2}(\boldsymbol{z}-\boldsymbol{\mu})^{\top}\boldsymbol{\Sigma}^{-1}(\boldsymbol{z}-\boldsymbol{\mu})\right), \tag{3.6}$$

where $\boldsymbol{\mu} \in \mathbb{R}^{p\times 1}$ and $\boldsymbol{\Sigma} \in \mathbb{R}^{p\times p}$ stand for the mean vector and covariance matrix of the training set, $\boldsymbol{Z}_{tr}$. In order to distinguish between target and outlier data a threshold on the probability distribution function is set and then, the Mahalanobis distance of a new object $\boldsymbol{z}_v$ is computed as follows:

$$d(\boldsymbol{z}_v) = \sqrt{(\boldsymbol{z}_v-\boldsymbol{\mu})^{\top}\boldsymbol{\Sigma}^{-1}(\boldsymbol{z}_v-\boldsymbol{\mu})}. \tag{3.7}$$

The instances with the $\theta = 10\%$ amount of largest Mahanalobis distance are regarded as outliers. As a result, an ellipsoidal boundary around the data is achieved. This method is expected to work reasonably well when the data are normally distributed.

3.2.2 Support Vector Data Description - *SVDD*

The objective of SVDD is finding the best data description of target data in OCC. Assume a dataset $\{\boldsymbol{z}_i, i = 1, ..., N_{tr}\}$, where N_{tr} is the number of target data. The objective function of SVDD is as follows (**?**):

$$\begin{aligned} &\min \quad R^2 + C\sum_{i=1}^{N_{tr}}\xi_i \\ &\text{s. t.} \quad \|\boldsymbol{z}_i - \boldsymbol{a}\|^2 \le R^2 + \xi_i, \quad \xi_i \ge \boldsymbol{0} \quad \forall i \in N_{tr} \end{aligned} \tag{3.8}$$

where $\boldsymbol{a}$ is the sphere center, R is the radius and ξ_i is a slack parameter used to incorporate the effect of data not included in the spherical description, i.e., it allows a soft boundaries (see

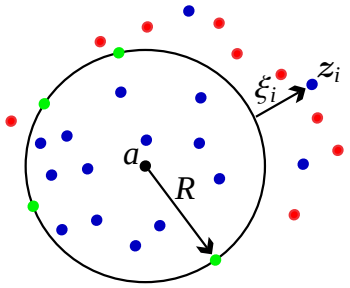

Figure 3.3: SVDD in feature space.

Fig. 3.3). The variable C represents the trade-off between sphere volume and the number of target data outside the sphere, allowing the relative importance of each term to be adjusted. To solve the optimization problem in (3.8), it is constructed a Lagrangian function as follows:

$$L(R, \boldsymbol{a}, \alpha_i, \gamma_i, \xi_i) = R^2 + C \sum_{i=1}^{N_{tr}} \xi_i - \sum_{i=1}^{N_{tr}} \alpha_i \{R^2 + \xi_i - \|\boldsymbol{z}_i - \boldsymbol{a}\|^2\} - \sum_{i=1}^{N_{tr}} \gamma_i \xi_i \tag{3.9}$$

where Lagrange multipliers are $\alpha_i \geq \mathbf{0}$ and $\gamma_i \geq \mathbf{0}$. Finding the stationary point of (3.9), the rearranged function in (3.8) is rewritten as:

$$\begin{aligned} &\min_{\boldsymbol{\alpha}} \sum_{i=1}^{N_{tr}} \sum_{j=1}^{N_{tr}} \alpha_i \alpha_j \mathcal{K}(\alpha_i, \alpha_j) - \sum_{i=1}^{N_{tr}} \alpha_i \mathcal{K}(\alpha_i, \alpha_i) \\ &\text{s. t.} \quad \sum_{i=1}^{N_{tr}} \alpha_i = 1, \quad \alpha_i \in [0, C], \quad \forall i, j = 1, \ldots, N_{tr} \end{aligned} \tag{3.10}$$

where $\mathcal{K}$ represents a Mercer's kernel; usually a Gaussian kernel with standard deviation σ (adjustable parameter) is employed, that is, $\mathcal{K}(\boldsymbol{z}_i, \boldsymbol{z}_j) = \exp\left(\|\boldsymbol{z}_i - \boldsymbol{z}_j\|/\sigma^2\right)$, with $i, j = 1, \ldots, N_{tr}$. Those vectors for which $\alpha_i = C$, termed the *bounded support vectors*, are located outside of the sphere, whereas the objects with $\alpha_i \in [0, C]$, or *unbounded support vectors*, are located exactly on the surface of the decision boundary sphere. By the way, a large fraction of the α_i should become zero during the optimization in (3.10). Then, the introduced squared distance of an object $\boldsymbol{z}_v \in \boldsymbol{Z}$, to the center of the sphere is estimated as follows:

$$d(\boldsymbol{z}_v) = \mathcal{K}(\boldsymbol{z}_v, \boldsymbol{z}_v) - 2 \sum_{i=1}^{N_{tr}} \alpha_i \mathcal{K}(\boldsymbol{z}_v, \boldsymbol{z}_i) + \sum_{i=1}^{N_{tr}} \sum_{j=1}^{N_{tr}} \alpha_i \alpha_j \mathcal{K}(\boldsymbol{z}_i, \boldsymbol{z}_j) \leq R^2 \tag{3.11}$$

In consequence, the threshold θ, is the radius calculated as the distance from the sphere center to an unbounded support vector. In practice, the average distance to a set of unbounded support vectors is used.

3.2.3 Performance measures

In classification problems, the primary source of performance measurements is the coincidence matrix showed in Table 3.2. The equations of most commonly used metrics that can be calculated from coincidence matrix are as follows (Olson and Delen, 2008):

$$\begin{aligned} prec &= \frac{t_p}{t_p + f_p} \\ rec &= \frac{t_p}{t_p + f_n} \\ f_1 &= 2 \cdot \frac{prec \cdot rec}{prec + rec} \end{aligned} \tag{3.12}$$

where $prec$, rec and f_1 denote precision, recall and f-measure, respectively. The precision or confidence denotes the proportion of predicted positive cases that are correctly real positives, whereas the recall or sensitivity is the proportion of real positive cases that are correctly predicted positive. The f-measure references the true positive instances to the arithmetic mean of predicted positives and real positives, being a constructed rate normalized to an idealized value (Powers, 2011). Those measures focus only on the positive instances and predictions, for which are adequate measures for OCC problems, i.e. when negative examples are missing. In addition, those measures are ranged at the interval [0, 1], being measure values closer to 1 a sign of satisfactory performance in classification.

3.3 Experimental setup

The proposed methodology comprises two different classification schemes, for which is employed the diagram displayed in Fig. 3.4. First, a traditional classification scheme is carried out, where OCC algorithms are trained with a feature set $\boldsymbol{Z} \in \mathbb{R}^{N \times p}$, such that the goal is detecting if any fault exists or not. Here, three distinct ways to build the feature sets are considered: *i)* $p = 24$ statistic features from the raw signal $y(t)$ (Table 3.1); *ii)* a singular statistical features ($p = K$) from each order component $x_k(t)$ such as standard deviation (OT-STD), root mean square (OT-RMS) and kurtosis (Ot-KURT), due to those statistics provided basic information about the physical nature of each narrow-band component; and *iii)* the similarity measures (OT-CCSD, OT-CSDI and OT-PCC) computed between $x_k(t)$ and $y(t)$ (i.e. $p = K$), aiming to encode the relevant spectral information that each dynamic feature enclosed.

In consequence, 8 feature sets are individually tested and fed into the OCC algorithms. Besides, a feature extraction stage is performed using PCA to compare the performance of the estimated features against a set the extracted features. It is worth noting that order decomposition could obtain a different amount of orders, and hence, to accomplish a square feature

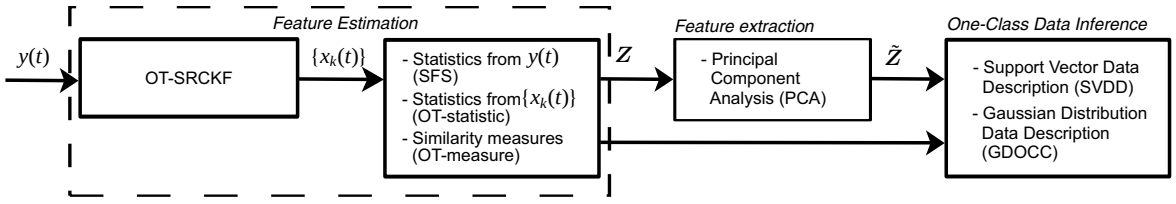

Figure 3.4: Diagram of proposed methodology for fault detection and identification using dynamic features extracted from order component decomposition method.

matrix $\boldsymbol{Z}$, it is needed to fix the p features according to the minimum number of decomposed components K.

Second, taking into account that each order component $x_k(t)$ holds the main characteristics of $y(t)$ in a limited-bandwidth defined by the order frequency $k\omega(t)$, it is possible assuming that $x_k(t)$ is a new *pseudo-observation*. In that sense, the OCC problem comes up the fault detection task like a frequency-located fault detection, where it is assessed if each order component is labeled either target or outlier. The statement mentioned above implies that an outlier order component could be associated with a type of fault, considering that damages close to low orders are related to the shaft defects (e.g. unbalance, misalignment, looseness, among others), and high orders are linked to either bearing or gear faults.

In particular, as regards feature set composition, $\boldsymbol{Z} \in \mathbb{R}^{(N\times K)\times p}$ indicates an augmented feature matrix, where $N \times K$ is the set of pseudo-observations. In a similar way that the first classification scheme, different feature sets are comprised by statistic features ($p = 24$), singular statistics (named as STATS with $p = 3$) comprising STD, RMS and KURT, and similarity measures ($p = 3$) including CCSD, CDSI and PCC, that is named as CSIM. Because of the feature matrix, $\boldsymbol{Z}$, in the major of cases has few features, the feature extraction stage is not carried out.

Both classification schemes are employed by a 20-fold cross-validation and 75% of target objects to training the algorithms aiming to reduce the overtraining, inasmuch the number of observations is very low. Besides, the fraction rejection of the OCC algorithms is fixed to 10%, which gives the fraction of the target set which will be rejected. The tuning of free parameters both SVDD and GDOCC are founded by grid search, in particular, the former case is $\sigma \in [1, 100000]$ using a logarithmic scale, and the last case uses the regularization of Σ given by $\tilde{\Sigma} = (1-\beta)\Sigma + \beta I_p$, being $\beta \in [0.05, 1]$ and I_p the identity matrix of dimension p. The methodology is tested using three different experiments obtained in a test rig from Universidad Nacional de Colombia. Firstly, a dataset that comprises unbalance and misalignment damages under two particular dynamic operating conditions (start-up and coast-down). Secondly, a dataset including bearing faults such as inner race (BPFI), outer race (BPFO) and ball bearing (BSF) defects, under constant speed. And lastly, a dataset of the same damages on bearing faults, but under coast-down operating condition.

3.4 Experiment on test rig: Universidad Nacional de Colombia data 1

A set of experiments is performed by using the supplied test rig, shown in Fig. 2.6, that includes a `2 HP Siemens` electromotor with a maximum speed of 1800 *rpm* (a detailed description is provided in Section 2.4.2).

The data set holds the following types of acquired outliers regarding the considered machine states: *i*) a static unbalance generated by a mass of 0.5*gr* located on the drilled wheel

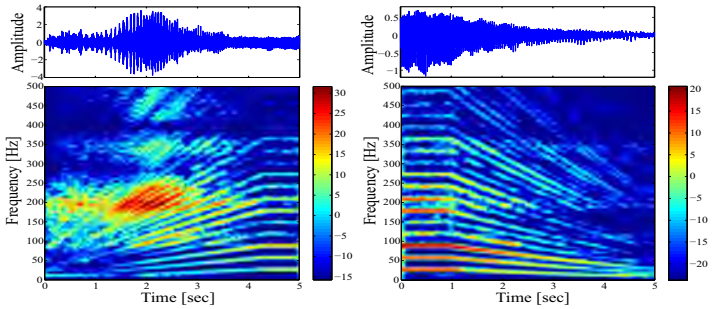

(a) Undamaged

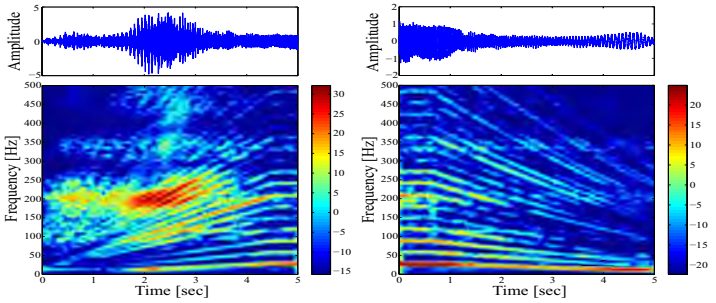

(b) Unbalance

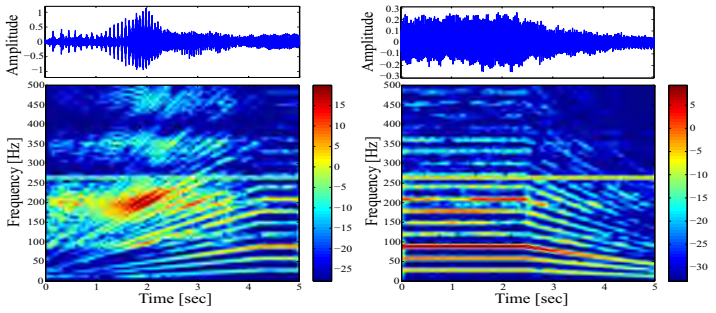

(c) Misalignment

Figure 3.5: An exemplary of signals under both operating conditions, (left) start-up and (right) coast-down. Each type of signal is presented in time domain (top) and its time-frequency representation (bottom).

closer to the rigid coupling, and *ii*) an angular misalignment generated by a horizontal and vertical displacements of 0.3 and 0.7μm, respectively. The data collection also includes an undamaged condition that is assumed as the target class. The recordings are measured under start-up and coast-down operating conditions, where each signal under coast-down condition (Fig. 3.5-right) contains three phases: *i)* maximum speed (1800 *rpm*), *ii)* turning motor off, and *iii)* steady–state regime. The start-up condition case (Fig. 3.5-left) has the same phases in reverse order. Each recording is five seconds long, and the working phases are not synchronized, that is, the decreasing (increasing) may begin at different times within each recording. Here, it is important to highlight that start-up condition includes an interference generated by the electromotor while the speed increase, whereas the coast-down condition shows clear order components.

As a result, 20 recordings were acquired for undamaged and unbalance classes, whereas for misalignment were 8. Taking into account that the maximum spectral information is around 1.2 *kHz* each recording is downsampled to 4*kHz* to reduce the computational cost, yielding a recording length of $L = 20000$ samples in 5*s*. Consequently, the respective OCC analysis is carried out both start-up and coast-down operating conditions using the traditional and novel classification schemes.

3.4.1 Analysis of start-up operating condition

With respect to the feature estimation, it is needed to define the signal harmonics that will be tracked by the SRCKF_OT algorithm. To cope this procedure, a harmonic estimation algorithm is performed to 1 second signal segment at maximum speed (i.e. the last recording second), obtaining the harmonics showed in Fig. 3.6. It is possible to observe that unbalance class presents a highest amplitude in the order attained to 30*Hz* (1*st* order), whereas the 3*rd* order stands out in misalignment and undamaged case. As a result, the amount of harmonics is $K = 10$, $K = 9$ and $K = 10$ for undamaged, unbalance and misalignment instances (that number could change depending on the spectral information of the each observation). In addition, the SRCKF covariances are fixed to $q_i^a = 10^{-6}$, $q^f = 10^{-9}$ and $r = 10^{-9}$, and an advantage of the method is based in the fact that the parameters are founded once time and

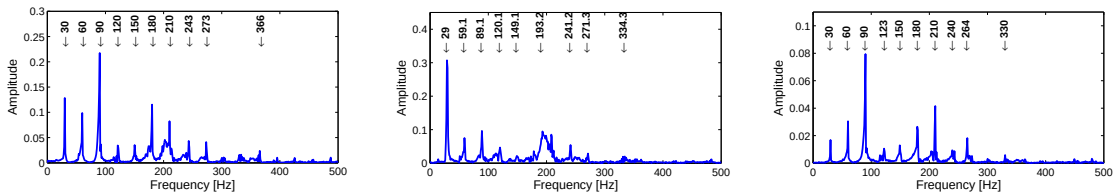

(a) Undamaged (b) Unbalance (c) Misalignment

Figure 3.6: Orders estimated from start-up regime using maximum harmonics algorithm.

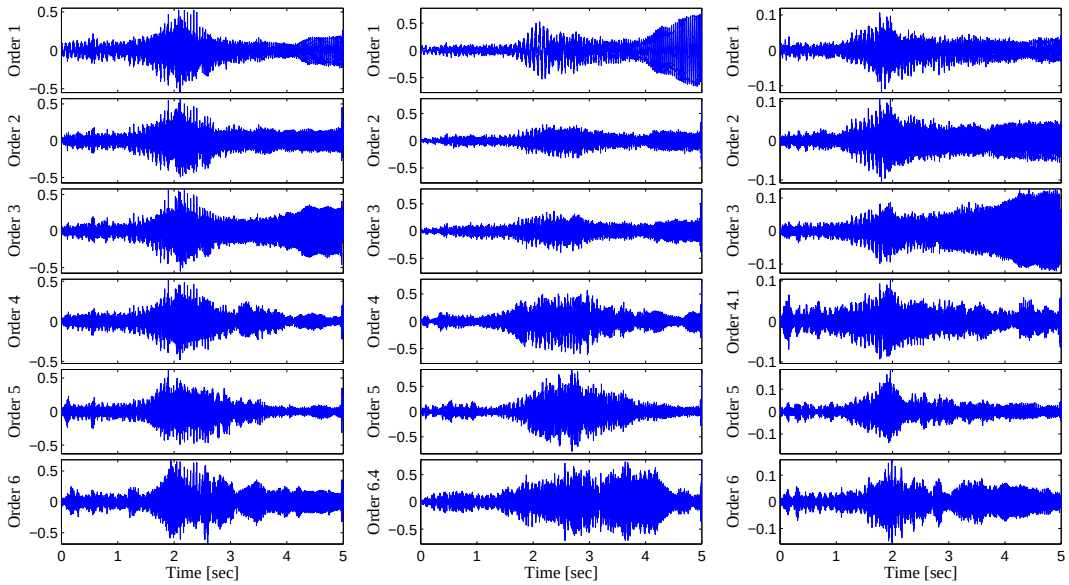

(a) Undamaged (b) Unbalance (c) Misalignment

Figure 3.7: An exemplary of first six order components for the machine states under start-up operating condition.

it does not need searching those parameter values again.

An exemplary of tracked orders in time domain is shown in Fig. 3.7, where it is notorious that both undamaged and misalignment are distributing the electromotor noise between all order components, increasing the OCC problem difficulty. In contrast, the unbalance class has different signal structures on each component, especially, the 1*st* order that could be considered without noise since it presents a great amplitude respect with the others.

Afterwards, the traditional classification scheme results are shown in Table 3.3, where it is observed that OT-RMS and OT-STD features overcome the other features, reaching an overall performance 95 ± 8.3 and 89 ± 11 percent using GDOCC ($\beta = \{0.5, 0.4\}$) and SVDD ($\sigma = \{8.8, 10\}$), respectively (where the first number indicates the mean value of 20-folds and the second is its corresponding standard deviation). Also, the traditional feature set (SFS) presents an acceptable performance, being comparable with OT-RMS and OT-STD when the SVDD is utilized. In contrast, the OT-KURT feature set achieves the worst performance, and when PCA is used, the performance does not increase (in almost all cases), which is expected in the sense that the employed OCC algorithms work better under the non-linearities of the feature set. On similarity feature sets, the obtained performance indicates that those characteristics are not suitable to represent the considered machine condition (start-up), nonetheless, by means the SVDD, the performance increases significantly.

In case of the classification scheme 2, Table 3.4 shows the averaged training performance of each classifier in terms of percentages. It is observed that both algorithms (GDOCC and

Table 3.3: Performance results in (%) of faults associated to shaft under start-up regime using the classification scheme 1.

	GDOCC				SVDD			
Feature set	f_p	*prec*	*rec*	f_1	f_p	*prec*	*rec*	f_1
SFS	5.2 ± 14	83 ± 3.5	90 ± 7.3	86 ± 4.1	0 ± 0	100 ± 0	72 ± 16	83 ± 14
SFS-PCA	16 ± 8.7	50 ± 10	81 ± 19	59 ± 5.5	4.5 ± 3.4	77 ± 18	67 ± 23	68 ± 14
OT-STD	**0 ± 0**	**100 ± 0**	**91 ± 14**	**95 ± 8.3**	**0.52 ± 1.7**	**97 ± 9.1**	**84 ± 14**	**89 ± 10**
OT-STD-PCA	11 ± 5.7	61 ± 16	84 ± 18	67 ± 5.9	4.1 ± 2.1	78 ± 10	78 ± 17	76 ± 10
OT-RMS	**0 ± 0**	**100 ± 0**	**91 ± 14**	**95 ± 8.3**	**0.52 ± 2.3**	**98 ± 9.6**	**83 ± 16**	**89 ± 11**
OT-RMS-PCA	8.6 ± 6.2	68 ± 18	80 ± 18	70 ± 7.2	2.8 ± 1.4	83 ± 9.7	75 ± 19	77 ± 12
OT-KURT	32 ± 16	30 ± 12	69 ± 19	40 ± 11	3.4 ± 0	61 ± 9.9	35 ± 14	44 ± 14
OT-KURT-PCA	94 ± 6.6	15 ± 1.3	94 ± 13	25 ± 2.5	5.9 ± 1.6	53 ± 11	39 ± 14	44 ± 12
OT-CSDI	21 ± 16	55 ± 30	83 ± 16	59 ± 16	2.4 ± 1.6	85 ± 11	69 ± 17	75 ± 10
OT-CSDI-PCA	21 ± 16	52 ± 29	78 ± 14	57 ± 17	0 ± 0	100 ± 0	67 ± 25	77 ± 19
OT-CCSD	21 ± 16	54 ± 30	81 ± 17	59 ± 18	1.2 ± 1.7	92 ± 14	65 ± 23	73 ± 18
OT-CCSD-PCA	17 ± 17	63 ± 32	78 ± 17	62 ± 16	0 ± 0	100 ± 0	62 ± 16	75 ± 12
OT-PCC	3.4 ± 2.5	83 ± 11	78 ± 19	78 ± 8.5	4 ± 2.6	75 ± 15	60 ± 17	65 ± 11
OT-PCC-PCA	4.1 ± 2.1	79 ± 8.2	84 ± 14	80 ± 4.6	2.2 ± 1.7	82 ± 14	56 ± 18	65 ± 16

Table 3.4: Performance results in (%) of faults associated to shaft under start-up regime using the classification scheme 2.

	GDOCC			SVDD		
Feature set	*prec*	*rec*	f_1	*prec*	*rec*	f_1
SFS	100	75	86	100	97	98
STATS	100	89	94	100	85	92
CSIM	**100**	**91**	**95**	**100**	**98**	**99**

SVDD) properly describe the target class, achieving performance rates over 86%. A precision (*prec*) of 100% indicates that all predicted training samples are effectively true positive, which it is expected since the training is performed using only target samples. Therefore, the performance depends on the proportion of real positive instances that are correctly labeled as target. Nonetheless, when the outlier objects are labeled by the classifiers, the performance rates do not preserve, which implies that a high classification rates in the training step do not entail a high performance in testing.

Fig. 3.8 displays the label assigned to each pseudo-observation ($x_{i,k}(t)$) from the actual observations $y_i(t)$, where the label could be target (blue color) or outlier (red color). Here, the goal consists of detecting if each order component labeled as outlier effectively corresponds with the expected fault, it means, in unbalance case (UNB) the outliers are located in the 1*st* order, whereas the 2*nd* and 3*rd* orders are characteristics from misalignment (MIS). As a result, the CSIM feature set reaches the best performance since it is able to distinguish the order components associated to faults mentioned above. The best or worst performance

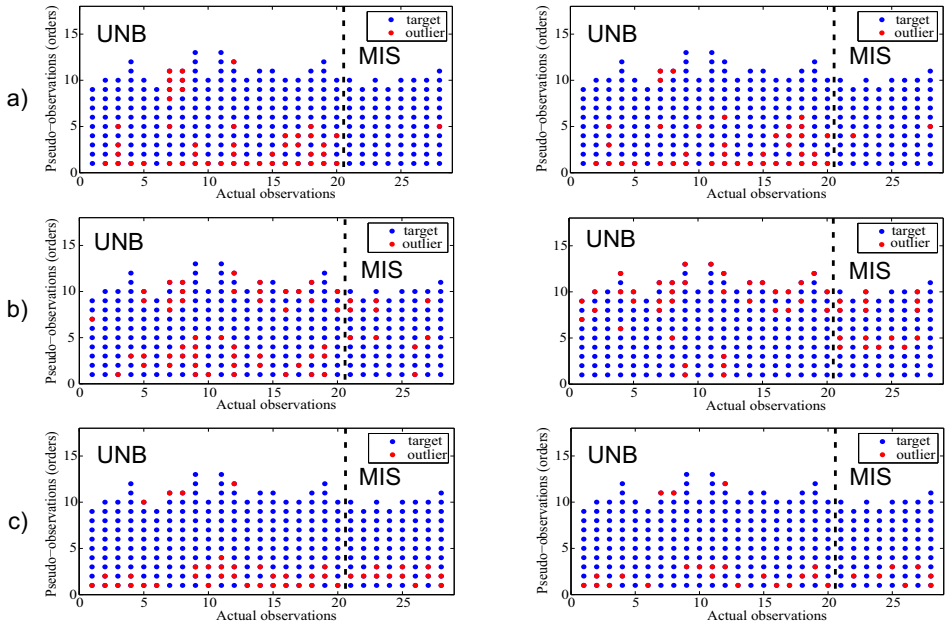

Figure 3.8: Performance obtained under start-up regime with (left) GDOCC and (right) SVDD classifiers using the features: a) SFS, b) STATS, c) CSIM.

is defined taking into account the ability for identifying the spectral range where the faults are present, from each pair OCC classifier together each type of feature set. It implies that in several classification outcomes the OCC methodology fails, for example, the class MIS is wrongly classified in the majority of employed approaches due to that the relevant order components are labeled either as outliers or targets. This low performance is because the pseudo-observations of undamaged and misalignment classes are very similar, and hence, the estimated features do not provide discriminant information.

3.4.2 Analysis of coast-down operating condition

When the proposed methodology is validated in the coast-down case, the obtained results are presented below. First, the set of harmonics (Γ) are calculated from 1 second signal segment using the algorithm proposed in Section 2.2.1. In consequence, the harmonics showed in Fig. 3.9 are introduced to the SRCKF_OT algorithm to estimate the new pseudo-observations. In this case, it is observed that undamaged class differs in amplitude from misalignment, but the 3*rd* harmonic still preserving the highest amplitude. As the same way than start-up operating condition, unbalance is characterized by a 1*st* order predominant.
For the sake of estimate the order components, the amount of harmonics of each observation is around $K = 11$, $K = 8$ and $K = 11$ for undamaged, unbalance and misalignment, respectively. Since the number of harmonics depends on the spectral information of the signal. Besides, the covariances of the OT algorithm are found through grid search, obtaining

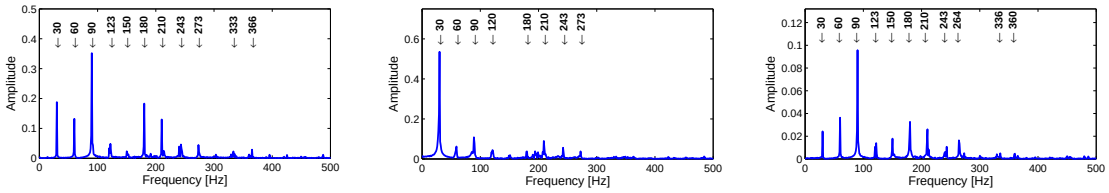

(a) Undamaged (b) Unbalance (c) Misalignment

Figure 3.9: Orders estimated from coast-down regime using maximum harmonics algorithm.

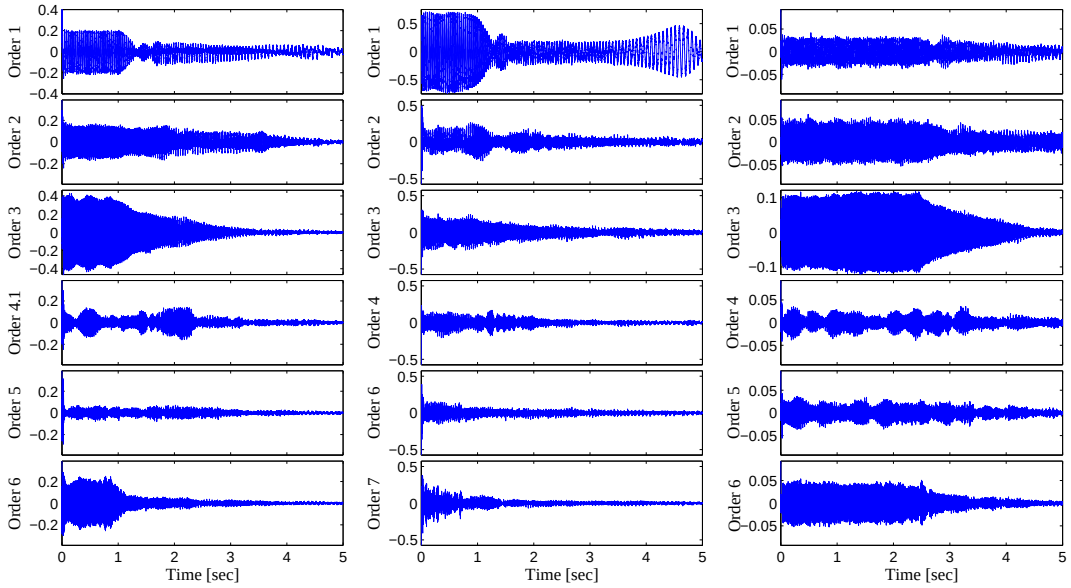

(a) Undamaged (b) Unbalance (c) Misalignment

Figure 3.10: An exemplary of first six order components for the machine states under coast-down operating condition.

the reference values $q_i^a = 10^{-4}$, $q^f = 10^{-8}$ and $r = 10^{-8}$, which may present changes of $10^{\pm 1}$, avoiding performing the complete searching. Fig. 3.10 displays an exemplary of six extracted order components that are considered as dynamic features. It is possible to see that the amplitude of each narrow-band component is consistent with its own amplitude showed in Fig. 3.9, that is, the 3*rd* order is predominant in undamaged class, as well as in misalignment, whereas in the unbalance class the highest amplitude corresponds to the 1*st*. It is worth noting that since the electromotor is turned off, there is no external noise that contaminates the order component information.

When the classification scheme 1 is applied, the OT-STD and OT-RMS achieve the best performance again, both using the GDOCC (with $\beta = \{0.45, 0.8\}$) and SVDD (with $\sigma = \{9000, 8500\}$) classifiers. In Table 3.5, it is observed that GDOCC overcomes to SVDD, but

Table 3.5: Performance results in (%) of faults associated to shaft under coast-down regime

	GDOCC				SVDD			
Feature set	f_p	*prec*	*rec*	f_1	f_p	*prec*	*rec*	f_1
SFS	9.2 ± 13	86 ± 5,6	92 ± 11	89 ± 6.6	**0 ± 0**	**100 ± 0**	**86 ± 22**	**91 ± 16**
SFS-PCA	3.8 ± 0.9	88 ± 6.1	92 ± 19	90 ± 13	2 ± 1.3	85 ± 14	87 ± 22	85 ± 16
OT-STD	**0 ± 0**	**100 ± 0**	**96 ± 8.2**	**98 ± 4.6**	**0 ± 0**	**100 ± 0**	**93 ± 9.8**	**96 ± 5.4**
OT-STD-PCA	27 ± 5.5	31 ± 3.8	93 ± 9.8	46 ± 4.5	16 ± 6.9	41 ± 7.4	80 ± 19	52 ± 3.9
OT-RMS	**0 ± 0**	**100 ± 0**	**96 ± 8.2**	**98 ± 4.6**	**0 ± 0**	**100 ± 0**	**89 ± 15**	**93 ± 9.3**
OT-RMS-PCA	25 ± 5.7	32 ± 4	92 ± 16	47 ± 6	20 ± 5.8	38 ± 8.6	92 ± 12	53 ± 6.4
OT-KURT	70 ± 13	14 ± 2.6	88 ± 12	24 ± 2.9	20 ± 1.3	33 ± 4.9	79 ± 19	47 ± 8.2
OT-KURT-PCA	79 ± 1.2	13 ± 1	93 ± 9.8	22 ± 1.9	23 ± 2.3	30 ± 3.8	82 ± 17	44 ± 6.5
OT-CSDI	6.6 ± 13	83 ± 29	95 ± 14	84 ± 22	**0 ± 0**	**100 ± 0**	**88 ± 14**	**93 ± 8.2**
OT-CSDI-PCA	7.4 ± 20	88 ± 27	96 ± 8.2	88 ± 22	**0 ± 0**	**100 ± 0**	**89 ± 17**	**93 ± 11**
OT-CCSD	5.8 ± 17	88 ± 26	96 ± 14	88 ± 22	**0 ± 0**	**100 ± 0**	**88 ± 15**	**93 ± 9.2**
OT-CCSD-PCA	5.8 ± 15	87 ± 27	87 ± 18	83 ± 21	**0 ± 0**	**100 ± 0**	**88 ± 16**	**93 ± 10**
OT-PCC	0 ± 0	100 ± 0	81 ± 17	89 ± 10	0.13 ± 0.6	99 ± 5.6	67 ± 25	77 ± 19
OT-PCC-PCA	0.13 ± 0.6	99 ± 4.5	84 ± 18	90 ± 12	0 ± 0	100 ± 0	63 ± 23	75 ± 16

Table 3.6: Performance results in (%) of faults associated to shaft under coast-down regime using the classification scheme 2.

	GDOCC			SVDD		
Feature set	*prec*	*rec*	f_1	*prec*	*rec*	f_1
SFS	100	86	93	100	86	93
STATS	100	82	90	**100**	**100**	**100**
CSIM	**100**	**97**	**98**	**100**	**98**	**99**

the last increases the performance (over 90%) when the similarity measures are employed, even using PCA. This fact implies that SVDD has a better generalization capability than GDOCC and offers more feature set options to characterize the considered faults. The possibility of working with a major set of distinct features, allows to assess relevant information that provide different physical interpretations. On the other hand, CSIM and STATS reach the best performance under the classification scheme 2, because of the training rate is 99% and 100%, when SVDD is applied Table 3.6. Nonetheless, the former case is better because the outcomes classifying the outliers shows that in many cases the pseudo-observations associated to unbalance and misalignment are correctly labeled as outliers. In spite of there are several mistakes concerning the exact order component that characterizes each fault, i.e., 1*st* and 3*rd* orders, the results indicate that the fault is located in a low frequency range (see Fig. 3.11(c)). As regards to STATS feature set, the performance is very low on the unbalance class, assigning the outlier label to the last order component. While SFS and CSIM achieve regular classification rates, falling in the number of accepted non-target pseudo-observations when GDOCC is used, and in some cases, labeling both low- and high-frequency instances

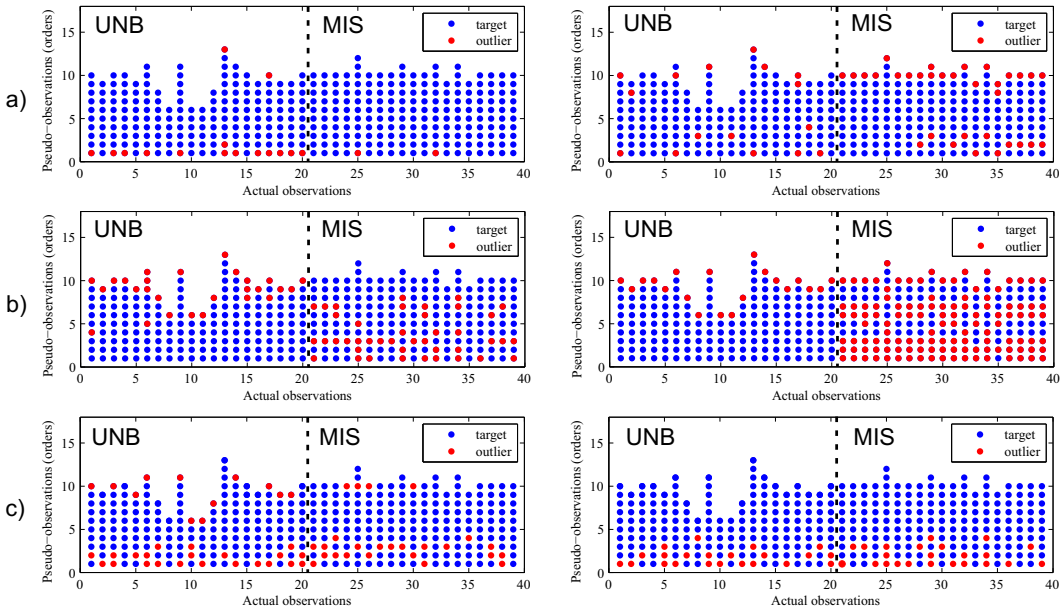

Figure 3.11: Performance obtained under coast-down regime with (left) GDOCC and (right) SVDD classifiers using the features: a) SFS, b) STATS, c) CSIM.

like target class. In misalignment case, CSIM has a satisfactory result since a big number of the objects are correctly classified. Conversely, both statistic feature sets do not provide a successful identification, because there are either a lot or none of the outliers accepted. This result may be caused by the similar component amplitudes between undamaged and misalignment classes.

In general terms, both classification schemes achieve satisfactory results when they are applied to detect frequency-located faults associated to shaft speed like unbalance and misalignment. In particular, the dynamic features based on order tracking components allow extract relevant information of the machine providing a physical meaning that improves the OCC interpretation.

3.5 Experiment on test rig: Universidad Nacional de Colombia data 2

The goal of this experiment is validating the proposed methodology (presented in Fig. 3.4) to detect bearing faults and identify the spectral range where the fault exists. The mechanical system is displayed in Fig. 3.12(a), and consists of a shaft driven by a 1.5*HP* DC electric motor able to reach 1720*rpm* through the equipped rigid coupling. The test rig has two bearings `HTH-UC206` and two drilling wheels that are used to simulate bearing and unbalance faults, respectively. The database holds acoustic signals lasting three seconds at 44.1*kHz* sam-

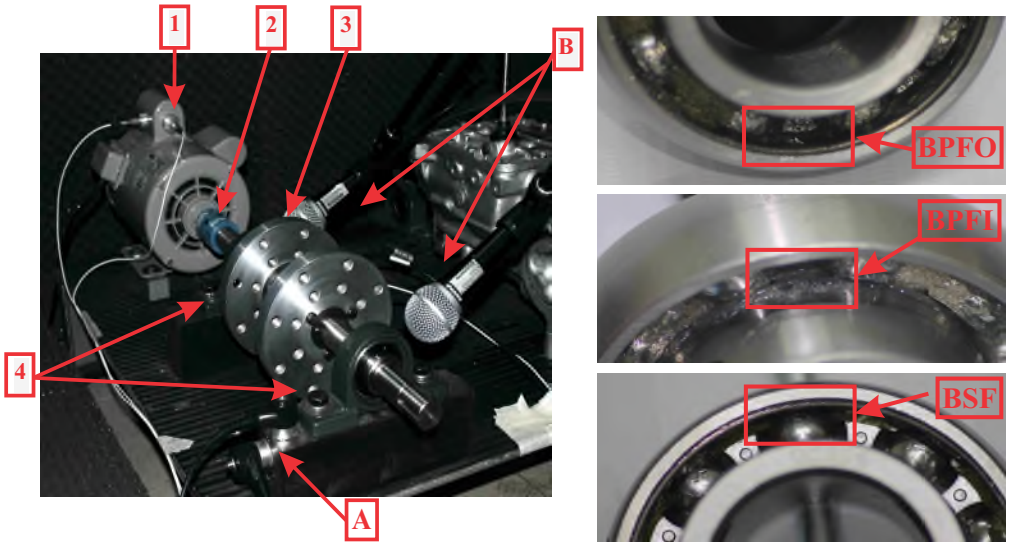

(a) (b)

Figure 3.12: Experimental test rig (left): 1) Motor driven, 2) Rigid coupling, 3) Drilling wheels, 4) Bearing housing. Sensors location: (A) Accelerometers and (B) Microphones. The simulated BPFO, BPFI and BSF defects (right).

pling frequency and 20 vibration recordings captured simultaneously, lasting four seconds at 25.6*kHz* sampling rate. The acoustic signals were acquired by two microphones located at a distance of 2*cm* in front of each bearing housing. Simultaneously, the vibration recordings were collected in the horizontal plane, employing several accelerometers mounted on bearing supports.

In the concrete case of introduced bearing faults, the following outlier classes in rotating machines are considered: inner race (BPFI), outer race (BPFO), and ball elements (BSF). The damages are simulated on the bearing located at shaft end, introducing a crack on the surface of interest with a motor tool (Fig. 3.12(b)). To validate the proposed OCC scheme, two different operating conditions are analyzed: steady-state regime and dynamic regime, that is, the machine operates under constant and variable (coast-down) speed, respectively.

3.5.1 Bearing faults under steady-state regime

For this experiment, the signals were recorded at $\sim 1800\,rpm$ constant speed and just the vibration signal closest to the faulty bearing is employed. Fig. 3.13 shows an exemplary of the different bearing faults in the time domain (top part) and its correspondingly time-frequency representation (bottom part) using the STFT with 8192 frequency bins, a Hamming window of 512 samples, and 50% of overlapping. The bearing faults evidence a notable cyclostationary behavior that is characteristic of this type of defects. Nonetheless, two aspects must be highlighted: First, it is expected that at high-frequency appears a representative

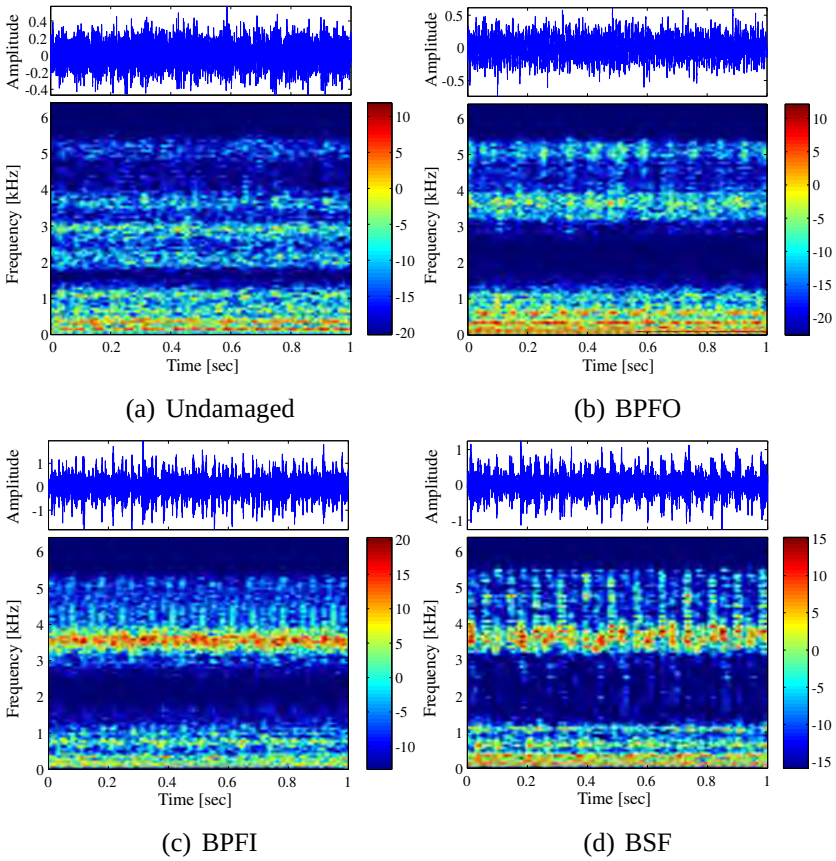

(a) Undamaged (b) BPFO

(c) BPFI (d) BSF

Figure 3.13: Exemplary of bearing fault signals in time domain (top part) and its time frequency representation (bottom part), which was acquired under steady-state regime.

spectral information, which is clearly observed in BPFI and BSF (around 3.5kHz), yet BPFO is distinct since the spectral information with the highest amplitude is under 1kHz. Second, the undamaged recording presents a cyclo-stationary phenomenon, which may be caused by the low quality of the bearings. Therefore, that behavior is not considered as a bearing fault and introduces more difficulties to the OCC problem.

Afterwards, aiming to obtain the different narrow-band spectral components $x_{i,k}(t)$ from the actual observations $y_i(t)$, the signal harmonics are estimated following the algorithm presented in Section 2.2.1. In consequence, the estimated harmonics to be tracked are displayed in Fig. 3.14 on the signal spectra, where it is possible to see that each machine state has a different number of harmonics K. Besides, it is worth noting that all faults have more amplitude than undamaged ones, because there is a big spectral component at 120Hz that is the four harmonic of the electromotor inasmuch it has four poles. In contrast, the biggest harmonic in the undamaged signal is 161.1Hz that is associated with the bearing quality.

In this particular signal instances, it is observed that BPFI has the highest spectral components at high-frequency compared with BPFO and BSF, being that phenomenon a clear

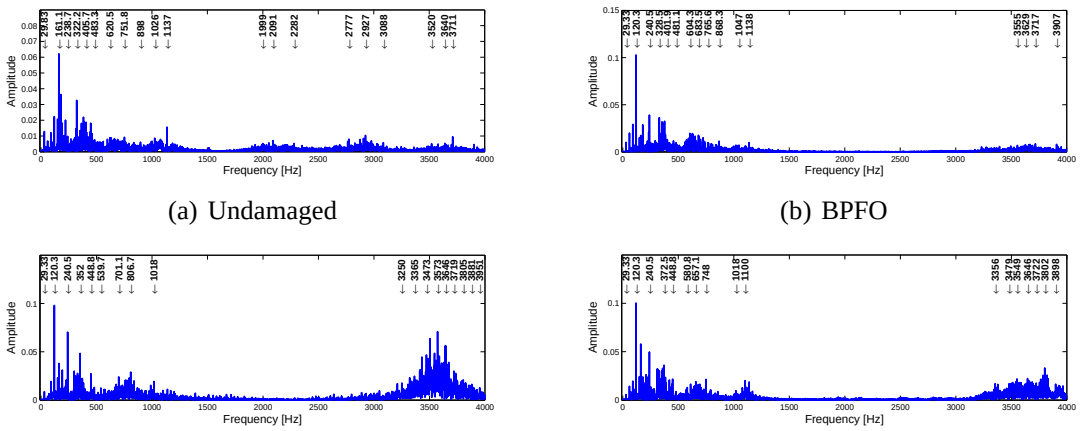

(a) Undamaged (b) BPFO

(c) BPFI (d) BSF

Figure 3.14: Orders estimated from bearing fault signals when the machine operates under a steady-state regime, and its respective spectrum.

sign of a bearing fault. As a result, $K = \{20, 16, 18, 17\}$ is the number of harmonics that are included into the SRCKF_OT algorithm for undamaged, BPFO, BPFI and BSF, respectively. In this case, the covariance parameters are heuristically fixed as $q_i^a = 10^{-3}$, $q^f = 10^{-6}$ and $r = 10^{-7}$ for all machine states. An exemplary of tracked order components is shown in Fig. 3.15, where the first three and the last three narrow-band dynamic features are displayed.

Since the machine speed is not measured, the interval $[L^f, H^f]$ is fixed as $[28, 32]Hz$, obtaining an estimated IF profile that oscillates between $[29.5, 30.5]Hz$, which allows that several components have noise. For instance, the $1st$ order of all considered machine states is very noisy, and hence, a clear sinusoidal component at the shaft speed frequency is not observed. Besides, the non-tracked harmonics are distributed among estimated harmonics, causing noisy order components. For those reasons, all obtained narrow-band components attained to $1st$ order present impulsive behavior that is added on the baseline associated with the main tracked frequency.

On the other hand, the last order components (lower row in each machine state) evidence a strong cyclo-stationarity that is described by the impulsive behavior, and hence, it is expected that those narrow-band components allow characterizing the bearing defects. From a visual inspection, it is possible to highlight that both BSF and BPFI have a clear cyclo-stationary behavior, whereas BPFO does not show a cyclic dynamic.

After obtaining the dynamic features $x_{i,k}(t)$, the different feature sets are estimated, and both classifiers are tested, achieving the results exhibited in Table 3.7. As a result of the fault detection task, OT-CSDI reaches the best performance with 95% using GDOCC, overcoming the classical SFS feature set that only achieves 82% of classification rate. In contrast, when SVDD is employed, OT-RMS performance is better improving OT-CSDI by 2%. Another

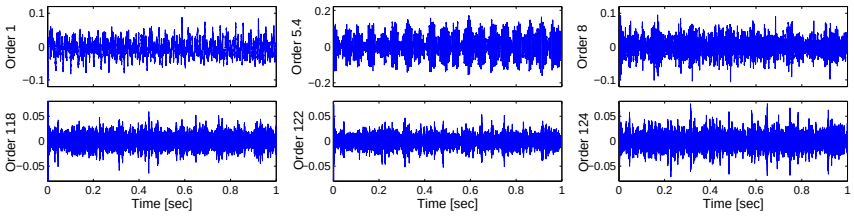

(a) Undamaged

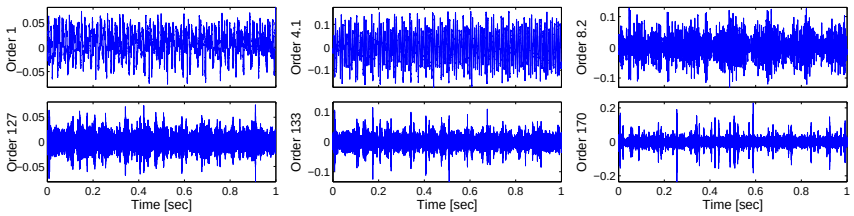

(b) BPFO

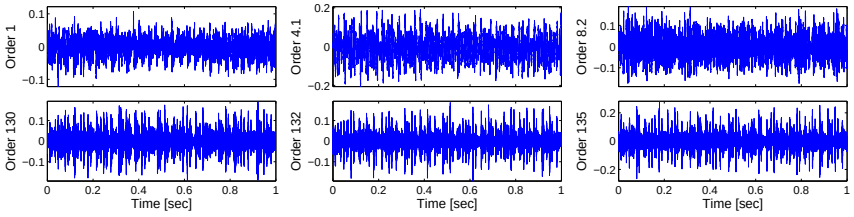

(c) BPFI

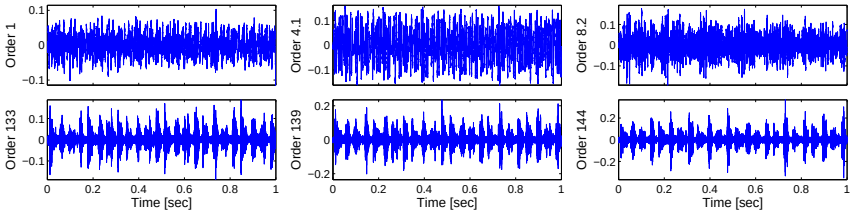

(d) BSF

Figure 3.15: Exemplary of several estimated order components from bearing fault signals when the machine operates in steady-state regime.

important aspect is based on the fact that the false positives f_p are zero, and the precision is 100% when OT-STD, OT-RMS, OT-CSDI and OT-CCSD features are used, indicating a perfect rate of the proposed OCC scheme for rejecting the outliers inside of the classifier boundary. In general, GDOCC accomplishes better outcomes than SVDD, and the utility of PCA is not reflected because the classification rates are not increased.

Regarding the classification scheme 2, where the pseudo-observations are characterized and fed into both OCC algorithms, CSIM obtains the best performance, reaching a perfect rate with SVDD in the training stage. Nonetheless, STATS achieves a similar classification rate with SVDD, whereas SFS makes the same with GDOCC (see Table 3.8). When the faulty signals are assessed, the high performance is associated with those order components

Table 3.7: Performance results in (%) of bearing faults under steady-state regime using the classification scheme 1.

	GDOCC				SVDD			
Feature set	f_p	*prec*	*rec*	f_1	f_p	*prec*	*rec*	f_1
SFS	12 ± 3.5	78 ± 1.2	87 ± 12	82 ± 7.3	10 ± 1.5	83 ± 11	78 ± 20	80 ± 13
SFS-PCA	19 ± 6.7	75 ± 12	87 ± 16	81 ± 12	17 ± 3.2	81 ± 5.5	83 ± 17	82 ± 10
OT-STD	**0 ± 0**	**100 ± 0**	**85 ± 23**	**90 ± 16**	**0 ± 0**	**100 ± 0**	**82 ± 25**	**88 ± 18**
OT-STD-PCA	25 ± 9.5	42 ± 15	80 ± 23	53 ± 10	17 ± 8.5	44 ± 15	60 ± 26	48 ± 11
OT-RMS	**0 ± 0**	**100 ± 0**	**87 ± 20**	**92 ± 13**	**0 ± 0**	**100 ± 0**	**82 ± 20**	**89 ± 13**
OT-RMS-PCA	27 ± 5.5	38 ± 3.8	83 ± 17	52 ± 5.8	39 ± 2.7	32 ± 3.5	90 ± 16	47 ± 5.9
OT-KURT	36 ± 6.3	28 ± 6.7	72 ± 25	40 ± 10	76 ± 5	15 ± 3.7	70 ± 21	25 ± 6.3
OT-KURT-PCA	51 ± 9.5	24 ± 4.6	82 ± 20	37 ± 7	77 ± 6.3	17 ± 3.4	80 ± 20	28 ± 5.7
OT-CSDI	**0 ± 0**	**100 ± 0**	**92 ± 18**	**95 ± 13**	**0 ± 0**	**100 ± 0**	**80 ± 25**	**87 ± 18**
OT-CSDI-PCA	2.3 ± 3.3	91 ± 13	93 ± 14	91 ± 10	**0 ± 0**	**100 ± 0**	**75 ± 26**	**83 ± 19**
OT-CCSD	**0 ± 0**	**100 ± 0**	**87 ± 17**	**92 ± 10**	4.7 ± 3.1	82 ± 12	87 ± 23	81 ± 12
OT-CCSD-PCA	**0 ± 0**	**100 ± 0**	**87 ± 17**	**92 ± 10**	**0 ± 0**	**100 ± 0**	**73 ± 21**	**83 ± 15**
OT-PCC	7.7 ± 7.6	76 ± 20	80 ± 25	72 ± 13	3.3 ± 4.6	84 ± 21	60 ± 17	68 ± 15
OT-PCC-PCA	19 ± 11	49 ± 17	77 ± 24	57 ± 16	21 ± 7.8	46 ± 14	83 ± 23	59 ± 15

Table 3.8: Performance results in (%) of bearing faults under steady-state regime using the classification scheme 2.

	GDOCC			SVDD		
Feature set	*prec*	*rec*	f_1	*prec*	*rec*	f_1
SFS	100	89	94	100	86	92
STATS	100	81	90	100	99	99
CSIM	**100**	**90**	**95**	**100**	**100**	**100**

labeled as outliers that comprise high-frequency spectral information. Therefore, observing Fig. 3.16, several aspects are found: firstly, GDOCC wrongly classifies a big number of pseudo-observations, accepting as outliers both low- and high-frequency order components, except the BPFO defects when the objects are characterized with STATS and CSIM. Secondly, the BPFI defect apparently could be distinguished in the majority of order components, because the narrow-band components are labeled as outliers lasting from the 1*st* to the final order. And lastly, the CSIM feature set together with SVDD classifies just the high-frequency order components as outliers, being consistent with the training performance and obtaining the best outcome taking into account the objective of the proposed OCC methodology.

3.5.2 Bearing faults under dynamic regime

The goal of this experiment consists of testing the proposed OCC methodology to discriminate defects on rolling element bearing mechanism when the machine operates at variable

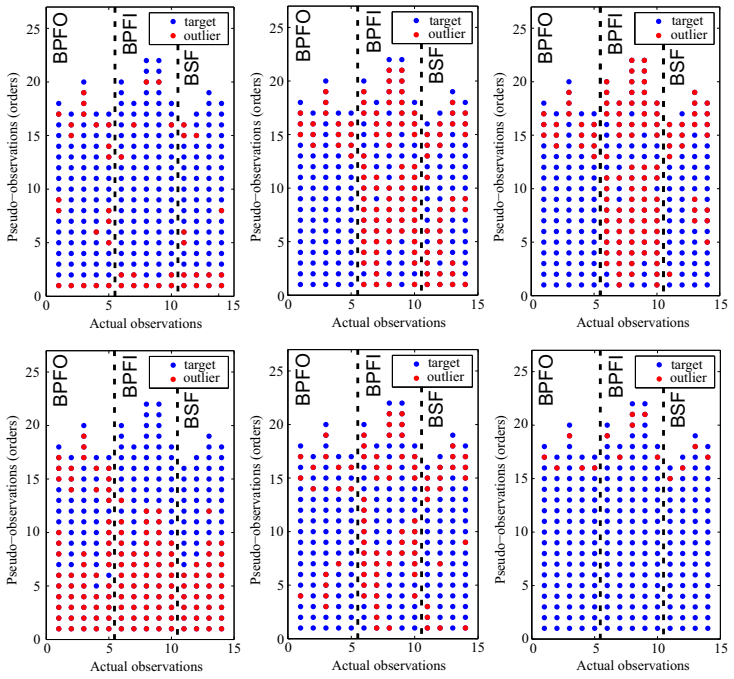

(a) SFS (b) STATS (c) CSIM

Figure 3.16: Performance obtained bearing faults under steady-state regime with (top) GDOCC and (bottom) SVDD classifiers using different feature sets.

speed, in particular, at the coast-down operating condition. In that sense, a set of recordings is captured from the test rig shown in Fig. 3.12 including several faults like BPFO, BPFI, and BSF. Here, the coast-down operating condition implies that the machine works at maximum speed (around $\sim 30Hz$) at the beginning of each signal, and then, the electromotor is turned off decreasing the speed to zero. As a consequence, the recordings lasts 5 seconds with a sampling frequency of $25600Hz$, and an exemplary of each machine condition is displayed in the left column of the Fig. 3.17. Particularly, Fig. 3.17-(Part 1) and -(Part 2) display the undamaged and BPFO, and the BPFI and BSF cases, respectively.

A visual inspection from the raw signals allows determining that the signal harmonics decrease proportionally to the speed change, which may be clearly observed in the undamaged case Fig. 3.17(a)-(left). Nonetheless, when the bearing faults are introduced (Figs. 3.17(b), 3.18(a) and 3.18(b) in the left side), a cyclo-non-stationary behavior emerges, causing AM-FM modulations that depends on the variable speed. That especial condition has been studied when the analyzed signal is mono-component, but in this type of vibrations signals the spectral content is multi-component. In that sense, the signal is treated as angle cyclostationary, and the SRCKF_OT approach could be employed.

Therefore, a signal pre-conditioning is carried out to alleviate the variable speed effects on the signal, applying the following two-steps approach:

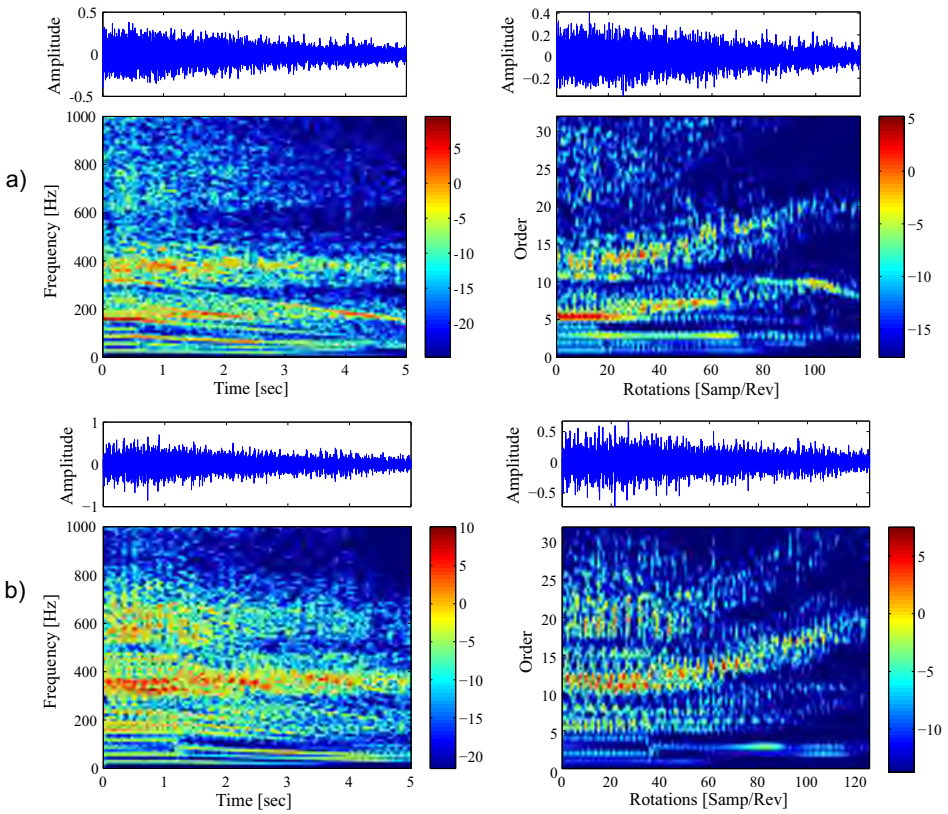

Figure 3.17: (Part 1) Exemplary of bearing fault signals from the machine under coast-down operating condition, both raw signal (left) and its resampled version (right): a) undamaged and b) BPFO.

- *Instantaneous speed estimation:* since the signal is a mixture of several dynamics including cyclo-stationary $x_c(t)$ and stationary $x_s(t)$ components that are governed by the non-stationary speed changes, the (3.1) could be expressed as follows:

$$y(t) = \sum_{c=1}^{K_c} x_c(t) + \sum_{s=1}^{K_s} x_s(t) \tag{3.13}$$

  where K_c and K_s are the number of order components associated with cyclo-stationary and stationary components, being $K = K_c + K_s$. In particular, the K_s components are found around the shaft speed comprising at least 3 or 5 harmonics, whereas the K_c are beyond the 6 harmonic. This fact could be appreciated in the bearing fault signals Fig. 3.17, and thus, it is feasible down-sampling the signal until obtaining a narrow band such that only $x_s(t)$ components appear. As a consequence, the IF is estimated from the removal of the $x_c(t)$ components using the SRCKF_OT algorithm.

- *Angle-order domain transformation:* With the estimated IF, the signal $y(t)$ is transformed into an angle-order domain using a widely known *computed order tracking* -

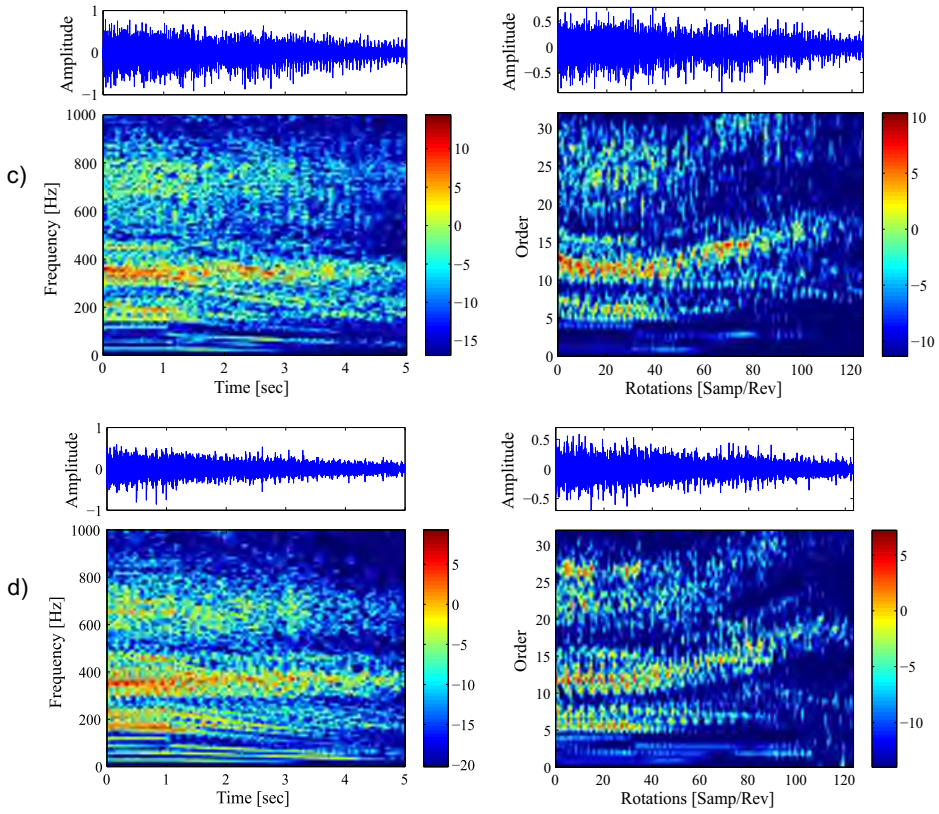

Figure 3.17: (Part 2) Exemplary of bearing fault signals from the machine under coast-down operating condition, both raw signal (left) and its resampled version (right): a) BPFI and b) BSF.

COT method discussed in (Potter, 1990; Fyfe and Munck, 1997). Where the signal $y(t)$ (sampled at constant increments of time, Δt) is re-sampled at constant increments of shaft angle, $\Delta\theta$, based on a keyphasor signal, which may be provided either from a tacho or IF signal. The resampling method is based on two different processes: First, a process of sample time determination, where the resamples are located on the independent axis (time). Second, a process of interpolation that locates the resamples on the dependent axis (amplitude). The success of COT depends on the determination of resample times as accurate as possible because it drives the interpolation process. In the concrete case of the bearing fault signals used in this experiment, the resampling method is performed with 64 samples per revolution, obtaining the angle-order map displayed on the right part of the Fig. 3.17. For the sake of simplicity, the angle domain is noted as rotations, where the domain unity is samples per revolution. The 64 samples used to resampling the signal allow to observe 32 order components, which are estimated using the SRCKF_OT algorithm because the non-stationary dynamic given by the speed changes has been removed.

As a result of the signal pre-conditioning, the obtained order-normalized signals $\hat{y}_i(t)$ are

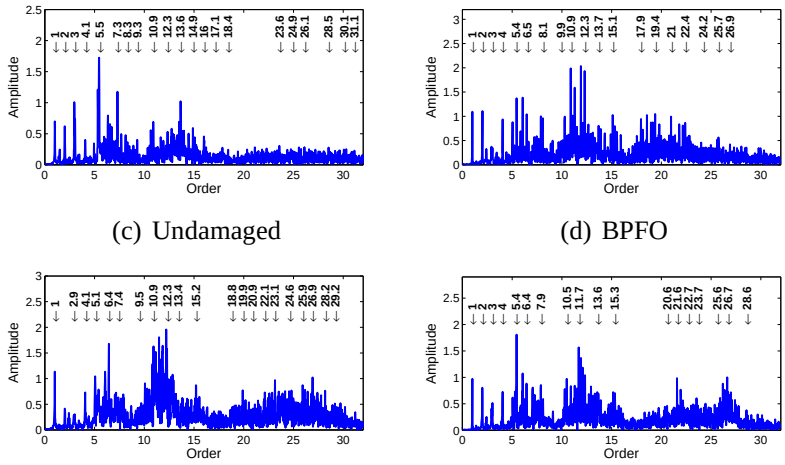

(c) Undamaged (d) BPFO

(e) BPFI (f) BSF

Figure 3.18: Orders estimated from bearing fault signals after COT is applied, when the machine operates under a dynamic regime, and its respective spectrum.

shown in Fig. 3.17-(right), where it is possible to observe that both time and angle domain signals are similar, but several differences are found from the visual inspection of the time-frequency representations. Firstly, the coast-down behavior was removed causing that the order components appear closer to a limited spectral band, and obtaining more separability among them. Secondly, the amplitude of the order components close to shaft speed (low orders) decreases and apparently they are not constant through the angle axis, yet the STFT scaling generates this visual effect. So lastly, the cyclic order components at the interval of $[300, 450]Hz$ (i.e., $[10, 15]th$ orders) preserve its structure but under constant speed. Nonetheless, those components give a false sensation that the speed is increased, because of the spectral information at the time interval of $[2, 3]$ seconds is of a higher order than between $[0, 2]$ seconds.

Afterwards, the set of harmonics Γ is calculated from the Fourier transform of each observation $\Im\{\hat{y}(\theta)\}$, obtaining the narrow-band components $\hat{x}_{i,k}(\theta)$. Fig. 3.18 displays an exemplary of the order components to be tracked, being $K = \{21, 19, 21, 18\}$ the number of harmonics that are included into the SRCKF_OT algorithm for undamaged, BPFO, BPFI and BSF, respectively. In this case, the covariance parameters are heuristically fixed as $q_i^a = 10^{-4}$, $q^f = 10^{-5}$ and $r = 10^{-9}$ for all machine states, having deviations of 10^1 and 10^{-1} for q_i^a and q_i^f, respectively. It is important to notice that the maxima amplitudes are similar between the considered classes, yet the damages present a more spectral information above the $10th$ order.

For that reason, in Fig. 3.19 a couple of order components are exhibited from low, medium and high frequency. Here, it is possible to see that the $1st$ order presents a low frequency that is a few perturbed by noise, however, the waveform is similar. On the other hand, the

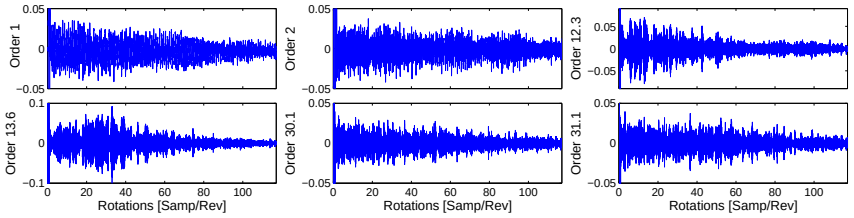

(a) Undamaged

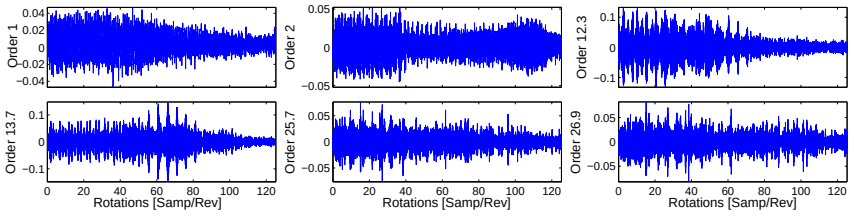

(b) BPFO

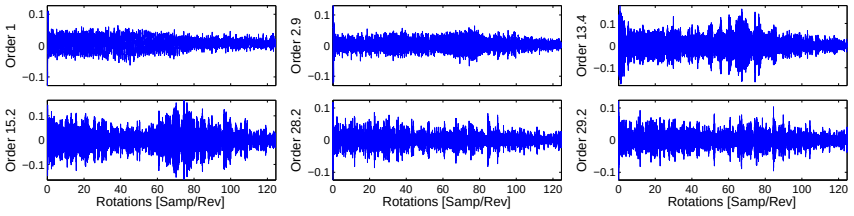

(c) BPFI

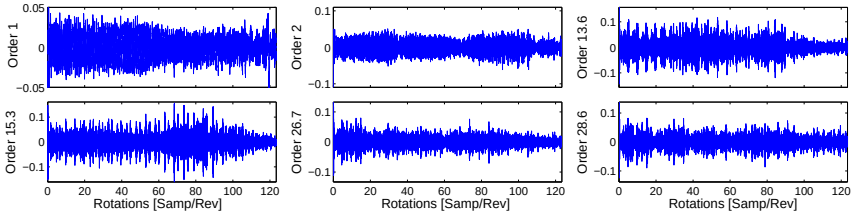

(d) BSF

Figure 3.19: Exemplary of estimated order components in low, medium and high frequency, from the re-sampled version of the bearing fault signals under coast-down operating condition.

medium and high order components (i.e., $[12, 15]th$ and $[28, 31]th$), present amplitude modulations that are generated by the shaft speed and the bearing fault fundamental frequency. Since the higher order components are more impulsive, it is expected that the proposed OCC methodology discriminates those ones.

As regards traditional OCC scheme, the 7 feature sets computed from the $\hat{x}_{i,k}(\theta)$ and the SFS set are each one fed into both classifier algorithms, obtaining the outcomes exposed in Table 3.9. Consequently, it is observed that OT-RMS and OT-STD achieve a performance rate above 90% and 80%, overcoming the other feature sets using both GDOCC and SVDD, respectively. Nonetheless, when the GDOCC is employed, the classical features reaches a relevant performance due to that the precision is 100% and all false positives are rejected.

Table 3.9: Performance results in (%) of bearing faults under non-stationary regime

	GDOCC				SVDD			
Feature set	f_p	*prec*	*rec*	f_1	f_p	*prec*	*rec*	f_1
SFS	**0 ± 0**	**100 ± 0**	**83 ± 23**	**89 ± 16**	8 ± 4.2	75 ± 6.4	85 ± 18	79 ± 13
SFS-PCA	0 ± 0	90 ± 5.8	85 ± 10	87 ± 6.2	12 ± 9.4	73 ± 8.5	84 ± 15	78 ± 8.9
OT-STD	**0 ± 0**	**100 ± 0**	**87 ± 17**	**92 ± 10**	**0 ± 0**	**100 ± 0**	**72 ± 22**	**82 ± 16**
OT-STD-PCA	1.3 ± 3.5	94 ± 15	72 ± 25	79 ± 20	40 ± 20	36 ± 24	78 ± 20	45 ± 16
OT-RMS	**0 ± 0**	**100 ± 0**	**92 ± 15**	**95 ± 8.9**	**0 ± 0**	**100 ± 0**	**75 ± 21**	**84 ± 15**
OT-RMS-PCA	8.7 ± 6.5	71 ± 18	87 ± 17	76 ± 12	13 ± 11	60 ± 31	58 ± 21	53 ± 17
OT-KURT	62 ± 25	23 ± 6.9	87 ± 25	35 ± 8.8	59 ± 2.7	20 ± 4.4	75 ± 21	32 ± 7.3
OT-KURT-PCA	77 ± 6.6	20 ± 2.7	97 ± 15	33 ± 4.5	58 ± 3.1	21 ± 5.2	78 ± 25	33 ± 8.7
OT-CSDI	4.7 ± 3.1	78 ± 16	73 ± 26	73 ± 17	6.3 ± 1.5	71 ± 10	78 ± 25	73 ± 16
OT-CSDI-PCA	43 ± 14	33 ± 16	93 ± 17	46 ± 9.5	9.3 ± 6.6	66 ± 23	67 ± 19	62 ± 13
OT-CCSD	2 ± 3.1	92 ± 13	75 ± 26	79 ± 17	8 ± 3.5	67 ± 15	80 ± 25	71 ± 17
OT-CCSD-PCA	28 ± 10	39 ± 7.3	87 ± 20	53 ± 8.9	16 ± 7.6	53 ± 21	78 ± 22	60 ± 14
OT-PCC	17 ± 11	54 ± 22	73 ± 26	56 ± 12	25 ± 12	38 ± 8.8	70 ± 21	47 ± 9.4
OT-PCC-PCA	24 ± 18	48 ± 27	73 ± 23	53 ± 19	**0 ± 0**	**100 ± 0**	**67 ± 24**	**78 ± 18**

Table 3.10: Performance results in (%) of bearing faults under non-stationary regime using the classification scheme 2.

	GDOCC			SVDD		
Feature set	*prec*	*rec*	f_1	*prec*	*rec*	f_1
SFS	100	91	95	100	87	93
STATS	100	86	92	**100**	**96**	**98**
CSIM	**100**	**94**	**97**	**100**	**98**	**99**

In contrast, the OT-PCC feature set joint PCA is able to get a similar classification rate (in terms of f_p and *prec*) using the SVDD classifier.

Different outcomes are appreciated from the second OCC scheme, where the set of similarity features CSIM achieves the best performance both GDOCC and SVDD classifiers, whereas the STATS set presents a similar performance using the last OCC algorithm (see OCC training performance rates exposed in Table 3.10). When the new pseudo-observations are classified either target or outlier (Fig. 3.20), it is observed that the training results are consistent. That is, CSIM can distinguish more accurately the order components that are related with the bearing faults using SVDD because the majority of outliers are above the $14th$ order and the low orders are labeled as target class. An interesting result is depicted by the STATS set, where the order components between $[9, 14]th$ are selected as outliers, inasmuch those components effectively present amplitude modulations and the most of those are associated to shaft speed modulations. In contrast, the classical SFS feature set presents the worst outcome since several low-frequency order components are labeled as outliers.

As a conclusion of this experiment, the traditional and novel OCC schemes were tested for

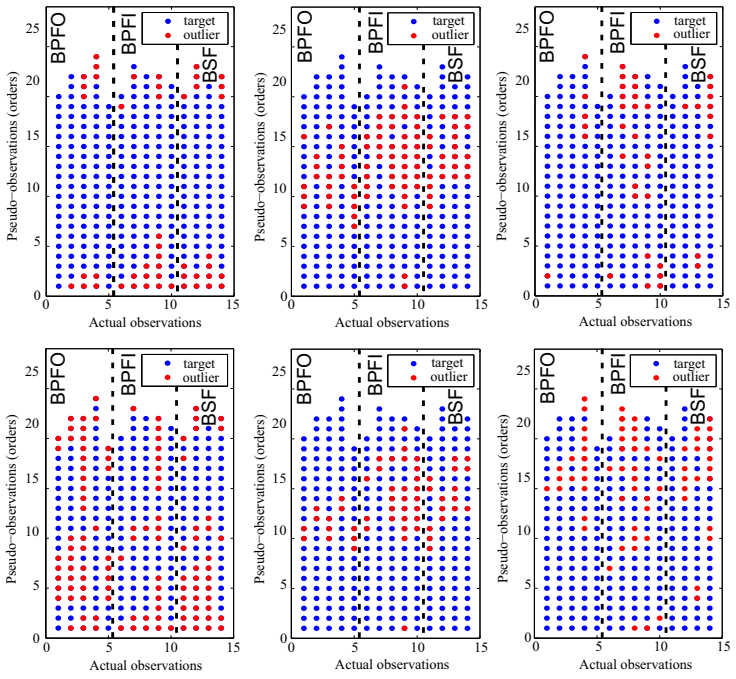

(a) SFS (b) STATS (c) CSIM

Figure 3.20: Performance obtained bearing faults under non-stationary regime with (top) GDOCC and (bottom) SVDD classifiers using the proposed feature sets.

bearing faults, providing useful information about the machine state in the former case. Besides, the second scheme gives information about the frequency range where the fault occurs, which is really important to reduce the searching of the fault when any fault is detected.

3.6 Discussion

The presented OCC methodology in this chapter gives interesting results that must be discussed from several points of view such as the types of machine fault, the performance of the OCC algorithms, and the interpretability provided by the feature sets. In that sense, it is worth to highlight the performance analysis both traditional and frequency-located fault detection schemes.

- As regards the distinct types of machine faults, the three experiments show that it is possible identifying both shaft and bearing faults either under non-stationary and stationary operating conditions. In particular, the traditional OCC scheme, which only detects if any fault exists or not, achieves classification rates between 95% and 98% to distinguish the considered faults. Here it is worth noting that the best-identified faults are the shaft defects under coast-down conditions because those signals present a

clear harmonic behavior, and there is no external noise that affects the characterization and classification processes. On the other hand, the proposed frequency-located OCC scheme reaches the best performance detecting the bearing faults when the machine operates under constant speed. Nonetheless, the most difficult faults to identify are misalignment and BPFI, inasmuch the similarity with the original signal is very high. For instance, in the former case the order components that characterize the undamaged, and the misaligned shaft are similar in amplitude, and hence, either under start-up or coast-down much order components are misclassified as outlier and target. Whereas the BPFI case, most of the order components are labeled as an outlier, which implies that this type of fault is distributed along the spectral range, and it may exist several narrow-bands that evidence the cyclo-stationary behavior.

- On the classification algorithms, it is found that GDOCC can distinguish the considered faults for the traditional OCC scheme, overcoming to SVDD. This fact implies that the built feature sets are appropriately modeled by a Gaussian distribution, and if the problem is delimited only to detect when a fault occurs, this classifier is the best option. In contrast, the experimental results show that to identify any fault present at a frequency band, it is better to use SVDD algorithm than GDOCC. The improvement obtained by SVDD may be based on the fact that there are more instances of the feature set, allowing to generate a data description boundary flexible since this classifier adjusts the boundary taking into account the slack variables. In general, both classifiers perform a high classification rate in terms of false positives and precision, which is most important in CBM problems since it is better to misclassify a target than an outlier.

- Regarding the feature sets carried out, it was proved that SFS does not provide a high generalization capability because the performance is not always successful in both classification schemes. This outcome implies that the non-stationary vibration signals must be enhanced and analyzed by frequency bands. In that sense, the proposed dynamic features based on OT decomposition performs a satisfactory signal characterization, because it preserves the signal properties comprised in a band-limited frequency. Therefore, the statistics could be applied on each band, obtaining that OT-RMS feature set achieves the better result to fault detection, yet CSIM improves the performance to frequency-located fault. That result is explained in the fact that the similarity measures taking into account the spectral information of each band compared with the complete signal. In consequence, a CBM system, that uses this methodology, may give more useful information to the machine operator allowing to detect when the fault occurs and which type of fault is growing.

4 Blind cyclostationary signal extraction based on order tracking

The vibration signal from rotating machines, in most of cases, comprises stationary and non-stationary components that describe the different processes occurring inside the machine. Thereby, the distinct components provide relevant information about the machine health, and the internal and external forces that affect the correct or incorrect system behavior. In the concrete case of the stationary components, these appear if the machine is running at steady-state regime where the speed and load are not time-varying. Nonetheless, when bearing faults arise, non-stationary processes also appears, whose statistical characteristics vary periodically with time depending on some period and are called *cyclostationary processes* (Gardner et al., 2006; Antoni, 2009). The bearing failure frequency governs the cyclic behavior, which may be generated by defects of the inner race, outer race, rolling elements and the cage (holding rolling elements together). Those frequencies are commonly known as *cyclic frequencies* generating AM modulations of the shaft speed (Obuchowski et al., 2014b; Borghesani, 2015).

In practice, the rolling element bearings are the heart of the machine and its failure is a common reason for machine breakdown. Therefore, the vibration signals generated by bearing damages have been widely studied, and powerful techniques are available to diagnose them (Randall and Antoni, 2011). One of the most used methods is the classical envelope spectrum of the raw signal (McFadden and Smith, 1984), because of its simplicity is preferred in the industry. Other methods consist of analyzing the time-frequency response of the signal to identify and characterize the frequency band where the fault occurs, being employed techniques like the Short-Time Fourier Transform (Feng et al., 2013; Obuchowski et al., 2014b,a), and the Wavelet Transform (Liu et al., 2007; Jena and Panigrahi, 2015; He et al., 2015). Nonetheless, the problem to detect a bearing fault signal had been addressed to separate the deterministic and the stochastic parts of the signal, extracting a signal of interest that exhibits the damage characteristics (Borghesani et al., 2012). On this matter, the synchronous averaging explained in Antoni (2009) is validated in real-world signals and a modified versions presented in Leclère and Hamzaoui (2014); Abboud et al. (2016) allow introducing speed fluctuations by a resampling into the angle domain. However, computed order tracking performs a similar signal resampling (Fyfe and Munck, 1997), and it may be used with envelope spectrum to extract the components that distinguish the bearing fault

patterns (Borghesani et al., 2013).

In spite of the multiple methods that could be applied to detect bearing faults, one of the most popular is based on the spectral kurtosis, which was formalized by Antoni (2006), and its improved versions like kurtogram (Antoni and Randall, 2006) and fast kurtogram (Antoni, 2007b) provide an accurate frequency band where the transient associated with an optimal frequency band is observed. On the other hand, there are the approaches based on the cyclic spectrum (Boustany and Antoni, 2005; Cioch et al., 2013; Borghesani, 2015) where the representation of the data in a cycle frequency-frequency domain allows observing precisely the effect of the different modulations that are present in the signal.

For that reason, this chapter is dedicated to demonstrate that the proposed OT model presented in the Chapter 2 has the needed conditions to extract cyclostationary signals. To this end, in Section 4.1.2 the proposed model is defined as a particular case of the cyclic autocorrelation and cyclic power spectrum. Since the proposed method acts as a narrow-band filter, a comparison with the spectral kurtosis is performed using two different datasets including bearing faults under steady-state and dynamic regimes, it means, constant and variable speed. The first experiment is based on the recent benchmark study presented in Smith and Randall (2015), where the recordings of the Case Western Reserve University are labeled as diagnosable, partially diagnosable, and not diagnosable, providing the conditions to use that dataset. The second experiment consists of validating the labels obtained in Section 3.5, where a set of bearing fault signals under different machine operating conditions are classified by a novel frequency-located fault identification scheme.

4.1 Cyclostationary signals

A signal is cyclostationary (CS) of order p (in the wide sense) if and only if it is possible finding some *pth*-order nonlinear transformation of the signal that will generate finite-strength additive sine-wave components, which result in spectral lines (Gardner, 1994). In that sense, a CS process is a stochastic process that exhibits some hidden periodicities in its statistical structure and encompass a subclass of non-stationary signals with an inherent cyclic behavior (Antoni, 2007a). In a simplest way, a signal CS could be understood like an amplitude modulated signal that is characterized by a pair of sidebands in the spectrum, which are spaced around each modulated frequency component by a number equal to the modulation frequency. Nonetheless, there is a hidden structure in the spectrum which can be discovered by correlating the spectrum with itself, giving non-zero correlation for displacements equal to discrete multiples of the sideband spacing, the so-called *cyclic frequency* (Randall, 2011).

4.1.1 Cyclostationarity definition

So, let be $y(t)$ a cyclostationary process whose joint probability density function is a quasi-periodic function of time, and for which its mean, $m_y(t) = \boldsymbol{E}\{y(t)\}$, and autocorrelation function, $R_y(t,\tau) = \boldsymbol{E}\{y(t+\tau)y(t)^*\}$, are periodic with some period T_0 (Gardner, 1990):

$$\begin{aligned} m_y(t+T_0) &= m_y(t) \\ R_y\left(t+T_0+\frac{\tau}{2}, t+T_0-\frac{\tau}{2}\right) &= R_y\left(t+\frac{\tau}{2}, t-\frac{\tau}{2}\right), \end{aligned} \tag{4.1}$$

where $R_y(t+\tau/2, t-\tau/2)$ is a function of two independent variables t and τ, which is periodic in t with period T_0 for each value of τ. It is assumed that the Fourier series representation for this periodic function converges, such that:

$$R_y(t,\tau) = \sum_{\alpha\in\mathcal{A}} R_y^\alpha(\tau) e^{i2\pi\alpha t}, \tag{4.2}$$

for which $\{R_y^\alpha\}$ are the Fourier coefficients,

$$R_y^\alpha(\tau) \triangleq \frac{1}{T}\int_{-T/2}^{T/2} R_y(t,\tau) e^{-i2\pi\alpha t} dt, \tag{4.3}$$

being $\alpha\in\mathcal{A}$ a set of *cyclic frequencies* where the so-called *cyclic autocorrelation function* or *cyclic cross-correlation function* $R_y^\alpha(\tau) \neq 0$. The cyclic autocorrelation can be characterized in a way that reveals the role that periodicity in autocorrelation plays in the frequency domain, implying that a process exhibits cyclostationarity in the wide sense only if there exists correlation between frequency-shifted versions of the process (Gardner, 1990). It also reveals that a process can be stationary only if there does not exist any correlation between any frequency-shifted versions of the process, because only then can $R_y^\alpha = 0$ for all $\alpha \neq 0$.
The Fourier transform of the cyclic autocorrelation function is a spectral descriptor of the signal $y(t)$ and is known as the *cyclic power spectrum* or *cyclic spectrum* (Boustany and Antoni, 2005),

$$S_y^\alpha(f) \triangleq \int_{-\infty}^{\infty} R_y^\alpha(\tau) e^{-i2\pi f\tau} d\tau. \tag{4.4}$$

The cyclic power spectrum may be also understand from the instantaneous probabilistic spectral density, denoted as $S_y(t,f)$, which is the Fourier transform of the instantaneous probabilistic autocorrelation,

$$S_y(t,f) \triangleq \int_{-\infty}^{\infty} R_y\left(t+\frac{\tau}{2}, t-\frac{\tau}{2}\right) e^{-i2\pi f\tau} d\tau, \tag{4.5}$$

where the cyclic power spectrum is the Fourier coefficients of the trigonometric expansion of $S_y(t,f)$ as follows

$$S_y(t,f) = \sum_{\alpha\in\mathcal{A}} S_y^\alpha(f) e^{i2\pi\alpha t}. \tag{4.6}$$

In consequence, the essence of the difference between stationary and cyclostationary or almost cyclostationary processes is that the latter exhibit spectral correlation. Furthermore, this spectral correlation is completely and conveniently characterized by the cyclic power spectrum $\{S_y^\alpha\}$ or equivalently by the cyclic autocorrelations $\{R_y^\alpha\}$.

4.1.2 OT model as cyclostationary process

From the OT model discussed in Section 2.1, the vibration signal $y(t) = x_{1,k}(t) = a_k(t)\cos(2\pi k f_r t + \phi(t))$ could be expressed in the *quadrature-amplitude-modulation* (QAM) form (Gardner, 1990):

$$x_{1,k}(t) = u(t)\cos(2\pi k f_r t) + v(t)\sin(2\pi k f_r t), \tag{4.7}$$

for any value of f_r and $k = 1$, provided $u(t)$ and $v(t)$ can be calculated by using the standard trigonometric identity as follows:

$$\begin{aligned} u(t) &= x_1(t)\cos(2\pi f_r t) + x_2(t)\sin(2\pi f_r t) \\ v(t) &= x_2(t)\cos(2\pi f_r t) - x_1(t)\sin(2\pi f_r t), \end{aligned} \tag{4.8}$$

being $x_2(t)$ the Hilbert transform of $x_1(t)$. In this case, if $x_1(t)$ is bandlimited to $f \in (f_r - B, f_r + B)$, then $u(t)$ and $v(t)$ are bandlimited to $f \in (-B, B)$, and hence, if $B < f_r$, $u(t)$ and $v(t)$ are uniquely determined by $x_1(t)$ and $x_2(t)$. Besides, it can be shown that for any process $x_1(t)$, (4.7) and (4.8) yield a unique definition of envelope magnitude, for which

$$\begin{aligned} a(t) &= [u^2(t) + v^2(t)]^{1/2} \\ \phi(t) &= \tan^{-1}\left[\frac{v(t)}{u(t)}\right]. \end{aligned} \tag{4.9}$$

This QAM representation, called *Rice's representation*, is valid regardless of the probabilistic model for $x_1(t)$. That is, $x_1(t)$ can be stationary, cyclostationary, almost cyclostationary, or more generally non-stationary. To this end, in Gardner (1990) a complete study of the correlation and spectral properties is presented, including the cyclic correlations and cyclic spectra, for $x_1(t)$ and its in-phase and quadrature components $u(t)$ and $v(t)$.
Specifically, let consider the process $u(t)$ as a *Linear Periodically Time-Variant* (LPTV) transformation of the two-dimensional vector of processes $\{x_1(t), x_2(t)\}$, for which the vector of impulse-response functions, that specify the LPTV transformation, $h(t+\tau, t) = \sum_{n=-\infty}^{\infty} g_n(\tau) e^{i2\pi n t/T}$ is periodic in t for each τ, where $\{g_n(\tau)\}$ are a set of Fourier coefficients. The representation of the impulse-response functions both in-phase and quadrature components is as follows:

$$h(t, z) = \{\cos(2\pi f_r t)\delta(t - z), \sin(2\pi f_r t)\delta(t - z)\}, \tag{4.10}$$

and the vector of corresponding system functions is

$$G(t,f) \triangleq \int_{-\infty}^{\infty} h(t,t-\tau)e^{-i2\pi f\tau}d\tau = \sum_{n=-\infty}^{\infty} G_n\left(f+\frac{n}{T}\right)e^{i2\pi nt/T} \tag{4.11}$$

where $G_n(f)$ is the Fourier transform of $g_n(\tau)$.
Therefore, the LPTV transformation, $u(t)$, in terms of cyclic autocorrelation defined in (4.3), is as follows

$$\begin{aligned} R_u^\alpha(\tau) =& \frac{1}{2}\left[R_{x_1}^\alpha(\tau)+R_{x_2}^\alpha(\tau)\right]\cos(2\pi f_r\tau)+\frac{1}{2}\left[R_{x_2x_1}^\alpha(\tau)-R_{x_1x_2}^\alpha(\tau)\right]\sin(2\pi f_r\tau) \\ &+\frac{1}{4}\sum_{n=-1,1}\left\{\left[R_{x_1}^{\alpha+2nf_r}(\tau)-R_{x_2}^{\alpha+2nf_r}(\tau)\right]+ni\left[R_{x_2x_1}^{\alpha+2nf_r}(\tau)+R_{x_1x_2}^{\alpha+2nf_r}(\tau)\right]\right\} \end{aligned} \tag{4.12}$$

and the Fourier transformation of $R_u^\alpha(\tau)$ allows to obtain the cyclic power spectrum as

$$\begin{aligned} S_u^\alpha(f) =& \frac{1}{4}\sum_{n=-1,1}\left\{\left[S_{x_2}^{\ \alpha}(f+nf_r)+S_{x_1}^{\ \alpha}(f+nf_r)\right]+ni\left[S_{x_2x_1}^{\ \alpha}(f+nf_r)-S_{x_1x_2}^{\ \alpha}(f+nf_r)\right]\right\} \\ &+\frac{1}{4}\sum_{n=-1,1}\left\{\left[S_{x_1}^{\alpha+2nf_r}(f)-S_{x_2}^{\alpha+2nf_r}(f)\right]+ni\left[S_{x_2x_1}^{\alpha+2nf_r}(f)+S_{x_1x_2}^{\alpha+2nf_r}(f)\right]\right\}. \end{aligned} \tag{4.13}$$

Equations (4.12) and (4.13) reveal that the set of cyclic autocorrelations and the set of cyclic spectra are each self-determinant characteristics under an LPTV transformation, in the sense that the only features of the excitation that determine the cyclic autocorrelations (cyclic spectra) of the response are cyclic autocorrelations (cyclic spectra) of the excitation (Gardner, 1990).
From (4.12) and its Fourier transform (4.13), it is possible to determine all cyclic correlations and cyclic spectra for $x_1(t)$, $u(t)$, and $v(t)$. For instance, with the use of $\alpha = \pm 2f_r$, it can be shown that the cyclostationarity of $x_1(t)$ at cyclic frequency α depends on the cyclostationarity of $u(t)$ and $v(t)$ at only the cyclic frequency α, if and only if the cyclic correlations are balanced in the sense that

$$\begin{aligned} R_u^{\alpha\pm 2f_r}(\tau) &= R_v^{\alpha\pm 2f_r}(\tau), \\ R_{vu}^{\alpha\pm 2f_r}(\tau) &= -R_{vu}^{\alpha\pm 2f_r}(-\tau). \end{aligned} \tag{4.14}$$

Otherwise, there is dependence on the cyclostationarity of $u(t)$ and $v(t)$ at cyclic frequencies $\alpha \pm 2f_r$, as well as at α.

4.1.3 Spectral kurtosis

Other method to characterize non-stationary processes, specially conditionally non-stationary (CNS) processes, is based on the combination of spectral cumulants, i.e. combinations of several moments of different orders, so-called *Spectral Kurtosis* (SK) (Antoni, 2006). In particular, when it is consider the Wold-Cramer decomposition of non-stationary signals, it is possible to define a signal $y(t)$ as the response of the system with time-varying impulse response $h(t, s)$, excited by a signal $z(t)$. Then, $y(t)$ can be presented as

$$y(t) = \int_{-\infty}^{\infty} H(t, f) e^{i2\pi f t} dZ(f) \tag{4.15}$$

where $H(t, f)$ is the Fourier transform of the time-varying impulse response $h(t, s)$ and $dZ(f)$ is the spectral process associated with $z(t)$. In (4.15), the transfer function $H(t, f)$ may be interpreted as the *complex envelope* or *complex demodulate* of the process $y(t)$ at the frequency f. Then, if $H(t, f)$ is conditioned to a given random variable ϖ that governs its time variations, the $2n$-order instantaneous moment that measures the strength of the energy of the complex envelope at time t and frequency f, can be defined as

$$S_{2ny}(t, f) \triangleq \boldsymbol{E}\left\{|H(t, f)dZ(f)|^{2n} \,|\varpi\right\} / df = |H(t, f)|^{2n} \cdot S_{2nz}. \tag{4.16}$$

Nonetheless, when $H(t, f)$ is time stationary and independent of the $dZ(f)$, the $2n$-order spectral moment can be defined by the ensemble averaging on many ϖ, that is, $S_{2ny}(f) = \boldsymbol{E}\left\{S_{2ny}(t, f)\right\}$, and therefore, the fourth-order spectral cumulant of a CNS process, $y(t)$, is defined as follows:

$$C_{4y}(f) = S_{4y}(f) - 2S_{2y}^2(f), \quad f \neq 0. \tag{4.17}$$

It can be shown that the higher deviation of a process from Gaussianity, the higher its fourth-order cumulant. Therefore, the energy-normalised fourth-order spectral cumulant provides a measure of the impulsivity of the probability density function of the process at frequency f. So, the SK is defined as

$$\kappa_y(f) \triangleq \frac{C_{4y}(f)}{S_{2y}^2(f)} = \frac{S_{4y}(f)}{S_{2y}^2(f) - 2}, \quad f \neq 0. \tag{4.18}$$

Since the high values that $\kappa_y(f)$ may take at whose frequencies where the process $y(t)$ present an impulsive behavior, the SK could be used as a filter function to separate the non-stationary

part of the signal from the stationary part. In that sense, when the signal $y(t)$ is characterized by impulsive components $z(t)$, and buried in additive stationary noise $\eta(t)$, the resulting measurement $y(t) = z(t) + \eta(t)$ has a spectral kurtosis

$$\kappa_y(f) = \frac{\kappa_z(f)}{[1+\rho(f)]^2} \tag{4.19}$$

where $\kappa_z(f)$ is the spectral kurtosis of $z(t)$ and $\rho(f) = P_n/P_z$ the noise-to-signal ratio. In conclusion, the optimal filter that maximises the similarity between the filtered component and the true noise-free signal, i.e. the Wiener filter, is the square root of the SK. Whereas the optimal filter that maximises the SNR of the filtered signal without regard to its shape, i.e. the matched filter, is a narrow band filter at the maximum value of SK (Randall and Antoni, 2011).

4.2 Experimental setup

The goal of the experiments that are presented below consists in to demonstrate the capability of the proposed SRCKF_OT model in Chapter 2 as a blind cyclostationary signal extraction method. To this end, a set of rolling element bearing signals are used because are one of the most mechanisms present in the machines and their failure causes a frequently machine breakdown (Randall and Antoni, 2011). Usually, the bearing faults start as small pits or spalls, and give sharp impulses in the early stages covering a very wide frequency range (even in the ultrasonic frequency range to 100kHz). Several types of bearing faults had been studied in Randall and Antoni (2011); Randall (2011), yet the experiments tested in this chapter are focused on localised faults that are characterized by a precise location of small pits, determining the nature of the impulsive response in the vibration signal.

In the concrete case of localised bearing faults, its modeling may be carried out as a cyclostationary process taking into account that the possible defects are governed by a cyclic frequency (Randall et al., 2001). In particular, each cyclic frequency may be approximated in accordance with the geometrical properties of the rolling element bearings and the shaft rotational speed f_r of the machine, as is shown in Table 4.1.

In Table 4.1, m is the number of rolling elements, D and d are respectively the bearing pitch and ball diameters, φ is the contact angle of the load from the radial plane. The fault frequencies above are based on kinematic relationships assuming that there is no frequency slip, yet it is always present having a variation from the calculated frequency of up to 1 – 2% (Smith and Randall, 2015). The main spectral characteristics from outer race, inner race, and rolling elements, which may be identified in the envelope spectrum are (Taylor, 1994): *i)* $BPFO$ and harmonics, sidebands spaced at f_r; *ii)* $BPFI$ and harmonics, sidebands spaced at f_r, harmonics of f_r; And *iii)* BSF and harmonics (even harmonics often dominant), sidebands spaced at FTF, harmonics of FTF.

Table 4.1: Rolling element bearing fault frequencies

Ball pass frequency, outer race:	$BPFO = \frac{mf_r}{2}\left(1 - \frac{d}{D}\cos\varphi\right)$
Ball pass frequency, inner race:	$BPFI = \frac{mf_r}{2}\left(1 + \frac{d}{D}\cos\varphi\right)$
Fundamental train frequency (cage speed):	$FTF = \frac{f_r}{2}\left(1 - \frac{d}{D}\cos\varphi\right)$
Ball spin frequency:	$BSF = \frac{Df_r}{2d}\left[1 - \left(\frac{d}{D}\cos\varphi\right)^2\right]$

Therefore, the cyclic frequencies corresponding with bearing faults, including $BPFO$, $BPFI$, and BSF, are evaluated in the envelope of the order components $x_{i,k}(t)$ according to (4.9). A graphical description of the experimental setup is shown in Fig. 4.1, where both methodologies discussed in this chapter are displayed: the proposed SRCKF_OT model and the spectral kurtosis.

Since the OT model provides a set of narrow-band components $x_k(t)$, the main idea is to evaluate if those components may be descriptors of cyclostationary signals, in particular, when a bearing fault process is present in the vibration signal $y(t)$. To select the most representative component, it is computed the correlation index (defined by (3.3)) between the envelope signal of $y(t)$ and the envelope signal provided by each order $x_k(t)$, namely $a_k(t)$ in function of (4.9). The obtained measure could be understood as a cyclic correlation that measures the similarity between each narrow-band decomposition and the raw signal.

To validate the OT approach, three experiments are carried out which are organized depending on the machine speed regime, that is, constant or time-varying. The first experiment is performed using the public dataset provided by Case Western Reserve University (CWRU), which includes different bearing faults under distinct load zones. In Smith and Randall (2015) a benchmark studied from that dataset is presented, where each recording is labeled depending on the fault is clearly identified or not. The challenge in this experiment is centered in validating the capability of the proposed approach in data clearly diagnosable and

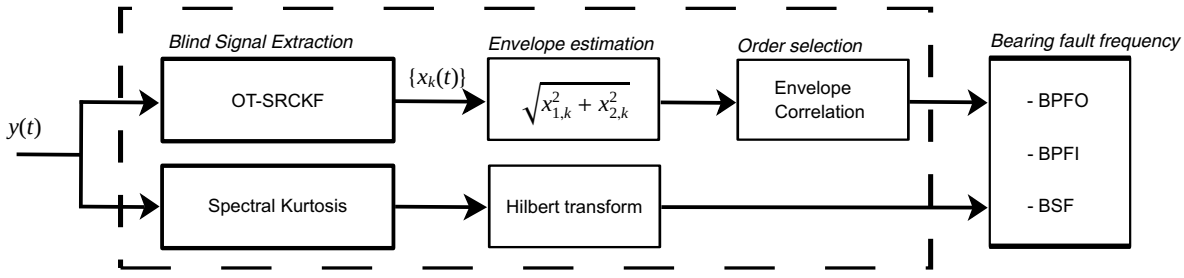

Figure 4.1: Experimental diagram for BSE using the proposed SRCKF_OT model.

not diagnosable for the specified bearing fault.
The second and third experiment is accomplished aiming to validate the existence of the bearing faults in the Universidad Nacional de Colombia data, at constant and coast-down speed operating conditions. The claim in this experiment is centered in the verification of the results obtained by the novel OCC scheme discussed in Section 3.5, because of that approach is just focused on the frequency-located fault detection. As a complement, the identification of the bearing defect, allowing to complete a CBM system that gives to the machine operator clear patterns related to the type of damage present on the system.

4.3 Experiment on test rig 1: Case Western Reserve University data

The provided signals by CWRU were captured from the test rig shown in Fig. 4.2(a). It consists of a 2 *HP* Reliance Electric motor driving a shaft on which a torque transducer and encoder are mounted. Torque is applied to the shaft by using a dynamometer and electronic control system. The dataset holds different types of faults ranging in diameter from 0.007 to 0.028 *in* (0.18-0.71 *mm*) which were seeded on the drive- and fan-end bearings (SKF deep-

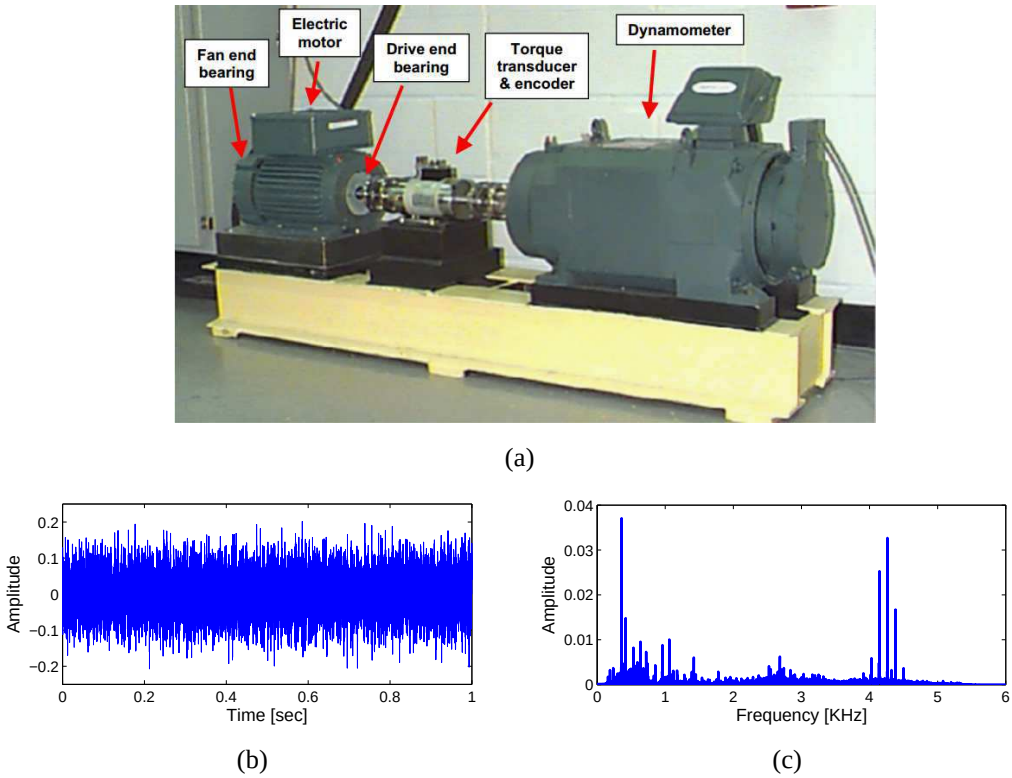

Figure 4.2: Test rig and an exemplary of drive-end bearing signals in undamaged condition[1].

groove ball bearings: `6205-2RS JEM` and `6203-2RS JEM`, respectively) of the motor using electro-discharge machine. Each bearing fault is seeded separately, and the vibration signal is acquired at constant speed for motor loads of 0 – 3 horsepower (approximate motor speeds of 1797-1720 *rpm*). On each test, the acceleration was measured in the vertical direction on the housing of the drive-end bearing (DE), the fan-end bearing housing (FE) and on the motor supporting base plate (BA). Two different sample rates were used including 12kHz and 48kHz, for which the bearing faults $BPFO$, $BPFI$, and BSF, and the undamaged signal are introduced. Further details regarding the test set-up can be found at the CWRU Bearing Data Center Website[1].

This experiment is focused on two different DE recordings acquired at 12kHz sampling frequency, and comprising all bearing faults, taking into account some records analyzed in Smith and Randall (2015), where all data were characterized and labeled accordingly with six categories: Y1, Y2, P1, P2, N1, and N2. The capital letter indicates if the bearing fault is clearly (Y), partial (P) or not (N) diagnosable, and the number provides a grade of difficulty. An exemplary of the undamaged condition is shown in Fig. 4.2 both in the time and frequency domain, where it is possible to see that predominant spectral components are concentrated at the frequency intervals [0.3 – 1] and [4 – 4.5]kHz.

Regarding with the bearing faults, the theoretical bearing fault frequencies are $BPFI = 5.415 f_r$, $BPFO = 3.585 f_r$, $BSF = 2.357 f_r$, and $FTF = 2.357 f_r$ which were calculated based on the kinematic information provided by the bearing manufacturer. Therefore, a set of cursors are located into the envelope spectrum to inspect the spectral components that match with the bearing fault frequencies. In that sense, each bearing fault is analyzed using both the proposed scheme and the SK as filter.

Inner race fault - BPFI

From the set of bearing faults on inner race, there were chosen the recordings DE171 and DE209, which were labeled in Smith and Randall (2015) as P1 and Y2, respectively. Thereby, DE171 is considered a signal partially diagnosable as inner race defect, whereas DE209 was clearly diagnosable but showing non-classic characteristics in either or both time and frequency domains. Analyzed bearing fault signals are shown in Fig. 4.3, where the left column corresponds with the record DE171 and the right column is for DE209. The time domain representation (top row) displays a one second signal segment, and it is observed that DE209 exhibit a clear cyclostationary behavior that is characterized by a constant cyclic period. In contrast, the record DE171 presents an impulsive pattern that is not constant though time.

When the frequency domain is inspected (middle row), it is possible to see that the spectrum of DE171 is wider than the DE209 spectrum, and presents harmonics entirely different

[1] Case Western Reserve University Bearing Data Center Website. http://csegroups.case.edu/bearingdatacenter/home.

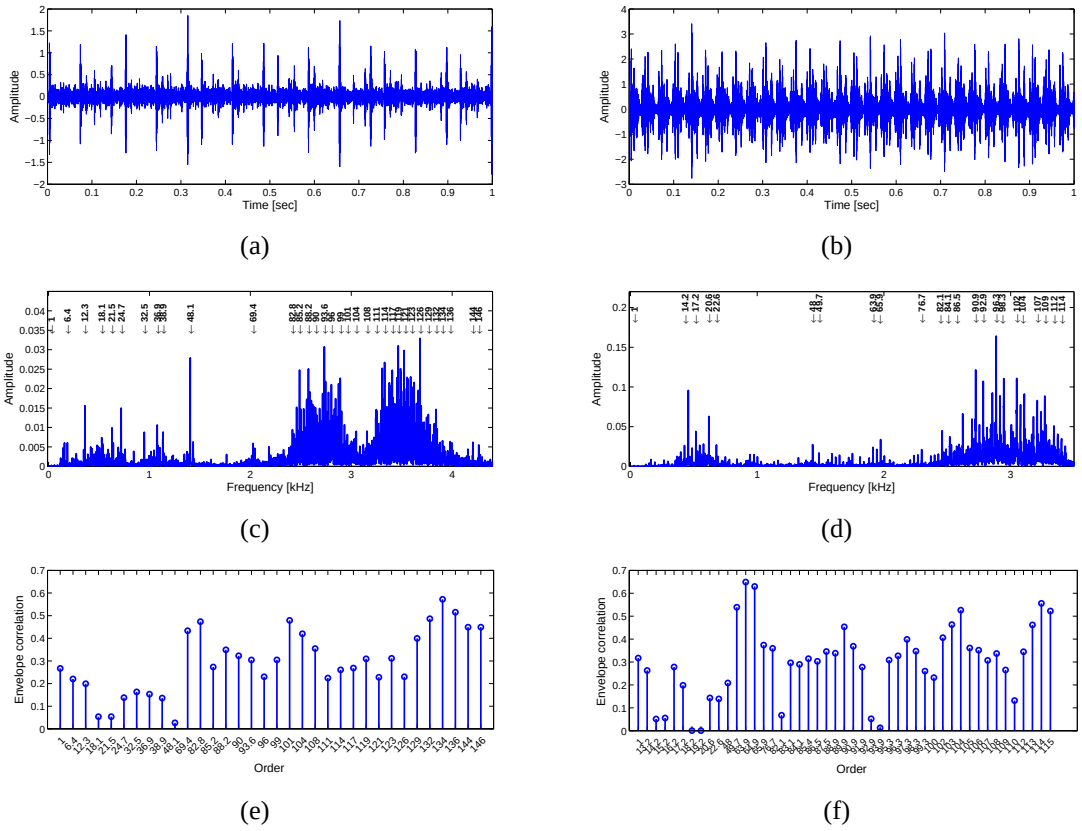

Figure 4.3: Recordings DE171 (left) and DE209 (right) in time domain (top row), frequency domain (middle row), and the envelope correlation indexes (bottom row).

amongst themselves. In fact, the DE209 spectrum evinces constantly spaced harmonics by shaft speed frequency (29.95*Hz*) that characterize an amplitude modulation process. In contrast, DE171 record just exhibits a pattern similar to wide-banded noise, hiding any characteristic of the inner race defect.

Afterwards, a set of harmonics (obtained by the algorithm presented in Section 2.2.1), is used to compute the proposed OT decomposition. The harmonics are disposed, regarding orders normalizing each one with respect to the shaft speed, in Figs. 4.3(c) and 4.3(f) for the recordings DE171 and DE209, respectively. As a result, a total of 34 and 47 order components are obtained from each record. It is worth noting that the 1*st* order is added to set a reference associated to the shaft speed, and the harmonics displayed are the most representatives from the author's point of view.

In the bottom row of the Fig. 4.3 the envelope correlation indexes between the obtained $x_k(t)$ order components and the raw signal $y(t)$ for both recordings are shown. The covariance parameters used to carry out the SRCKF_OT algorithm were $q_i^a = 10^{-4}$, $q^f = 10^{-11}$, and $r = 10^{-12}$, for the vibration signals analyzed in this experiment. It is observed that there

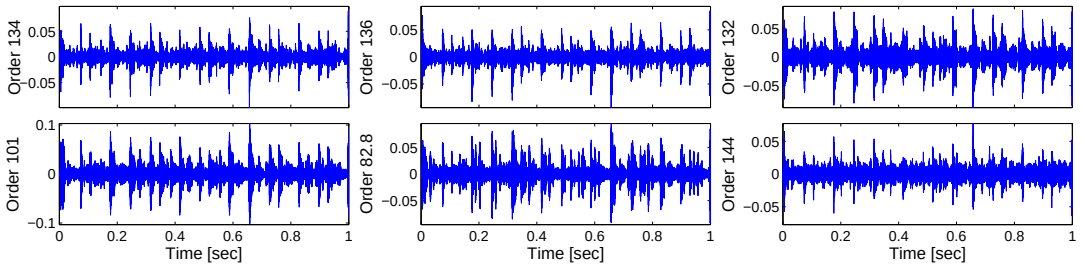

(a) Record DE171

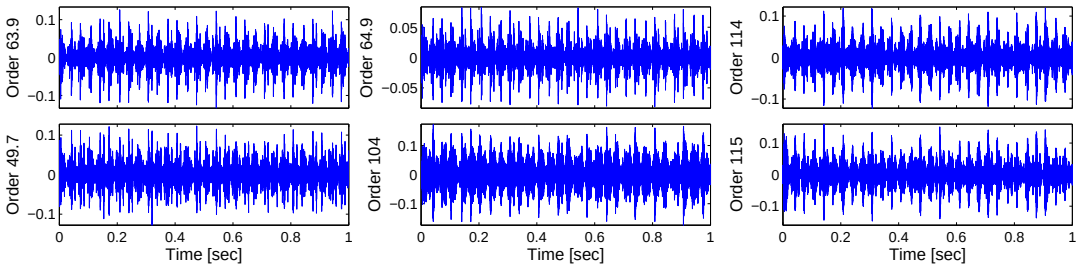

(b) Record DE209

Figure 4.4: Exemplary of the order components with the highest envelope correlation index for both inner race fault recordings from CWRU data.

are more order components correlated with the original signal in the record DE209 than in DE171, assuming a threshold of 0.5, and if the envelope correlation works as an indicator of cyclostationary processes, the highest order component correlated with the signal may exhibit the fault condition. In that sense, Fig. 4.4 displays the six order components more correlated with the raw data, proving that a modulation process governs each one.

After performing a visual inspection of the relevant order components and its envelopes, it is determined that the highest correlated order component captures the cyclostationary dynamic that allows identifying the BPFI frequencies, and hence, the inner race defect. A comparison with SK approach is given in Figs. 4.5 and 4.6 for the records DE209 and DE171, respectively. In particular, the record DE209 evinces clearly both the $BPFI$ frequency, the second harmonic of $BPFI$, and the sidebands spaced by nf_r (being $n = \{1, 2, 3, 4\}$) from the $BPFI$ frequencies.

From a visual inspection in Fig. 4.5, it is possible to see that the cyclostationary signal obtained by the proposed scheme apparently exhibit a cyclic behavior more impulsive, yet the filtered signal by SK presents a higher amplitude at $BPFI$ frequency. The envelope spectrum is normalized to the unity to highlight the comparison between both approaches, since in the time domain the obtained signal with SK has a higher amplitude. Nonetheless, the signal provided by SRCKF_OT displays the main spectral components that allow distinguishing the inner race defect.

Similarly, when the BSE approaches are applied to the DE171 data, it is shown in Fig. 4.6

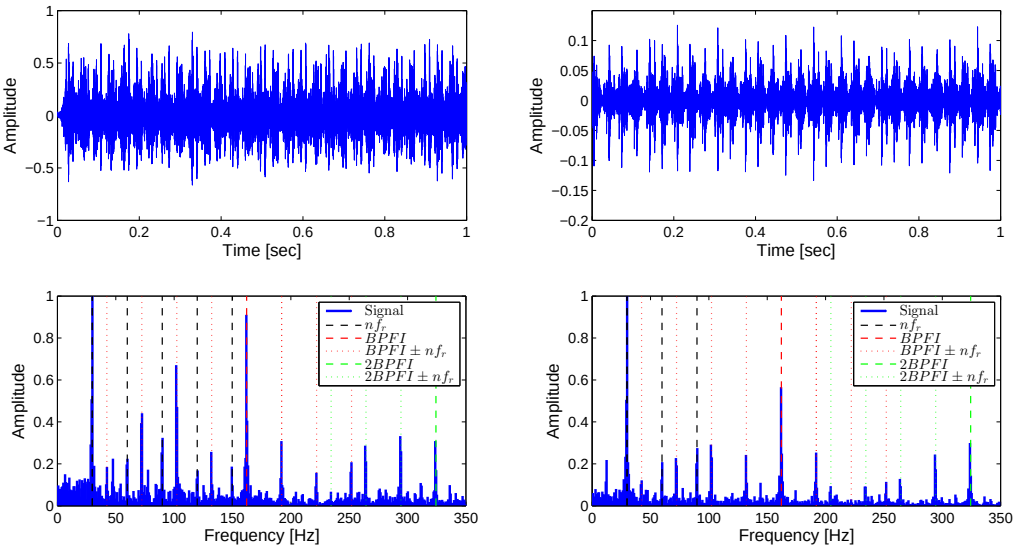

Figure 4.5: Identification of the BPFI frequencies on the envelope spectrum from DE209 using both SK (left) and proposed SRCKF_OT (right) approaches.

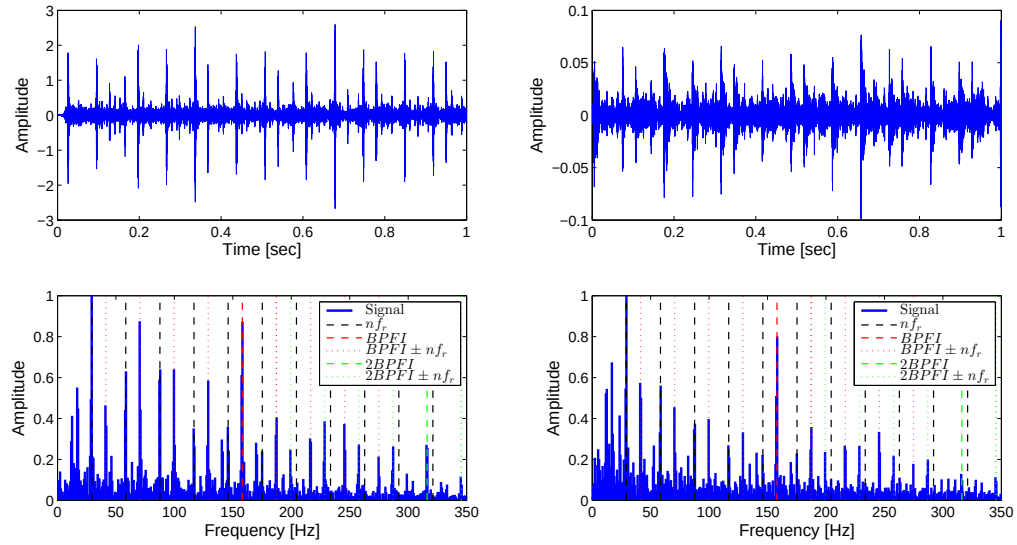

Figure 4.6: Identification of the BPFI frequencies on the envelope spectrum from DE171 using both SK (left) and proposed SRCKF_OT (right) approaches.

that it is clearly diagnosable the inner race defect because the $BPFI$ frequency is perceptible with high amplitude, and there are multiple sidebands spaced at $BPFI \pm f_r$. As a result, both approaches changes the category from P1 to Y2, taking into account the categories defined in Smith and Randall (2015), because the $BPFI$ frequency is differentiable in amplitude from its sidebands and the shaft speed harmonics. Furthermore, the signal in the time domain does

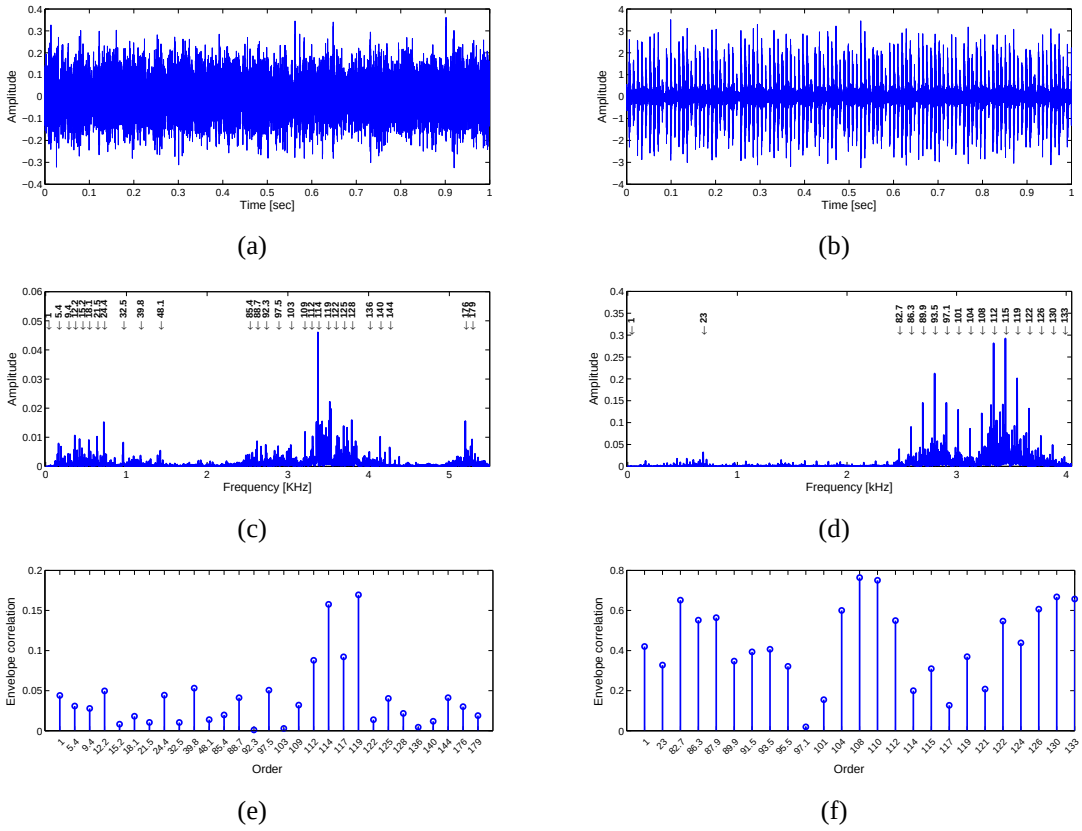

Figure 4.7: Recordings DE198 (left) and DE130 (right) in time domain (top row), frequency domain (middle row), and the envelope correlation indexes (bottom row).

not exhibit a periodic impulsive behavior.

Outer race fault - BPFO

In this experiment, the DE130 and DE198 were the bearing fault signals chosen which present an outer race defect. Those signals are analyzed because the former case presents a clear characteristics from the considered fault (category Y1), whereas the latter is not diagnosable (N2) in accordance with Smith and Randall (2015). In fact, the signals in time domain show appreciable differences, since from a visual inspection, the record DE130 is governed by a cyclic impulsive behavior, yet the record DE198 is indistinguishable from noise (right and left columns in Fig. 4.7-(top row), respectively).
The signal spectra, displayed in the middle row of the Fig. 4.7, exhibit a great differences between the considered recordings, inasmuch in the case of the DE130, there are spectral components located at high frequency and spaced at $BPFO = 3.585\, f_r$, where $f_r = 29.93Hz$. In contrast, the spectrum of DE198 presents low amplitude spectral components where the harmonic 114 of $29.5Hz$ stands out, and there is no evidence of the cyclic fault frequency. Other

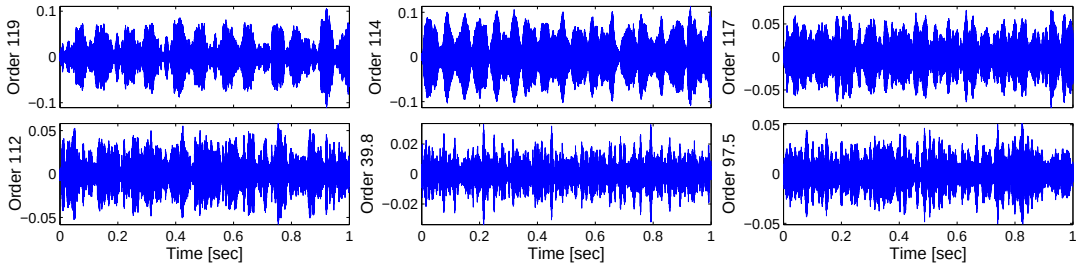

(a) Record DE198

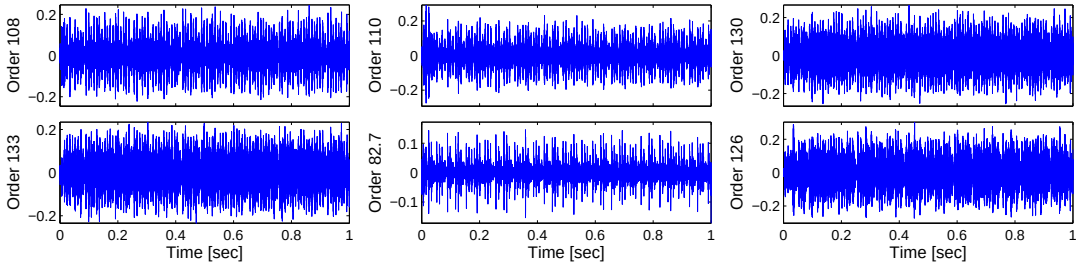

(b) Record DE130

Figure 4.8: Exemplary of the order components with the highest envelope correlation index for both outer race fault recordings from CWRU data.

important difference between the signals is found after applying the proposed scheme and computing the envelope correlations, because of the correlation values obtained in DE130 are higher than the values in DE198 (see the bottom row in Fig. 4.7). This fact implies that the obtained order components capture the cyclostationary behavior generated by modulations between the cyclic fault and shaft frequencies.

Nonetheless, in spite that the envelopes of the order components obtained from the record DE198 are not highly correlated with the envelope of the raw vibration signal, the components with higher correlation describe a modulation processes that may be associated with the bearing fault, but this behavior is dominated by a low frequency modulator signal. In Fig. 4.8 the six order components highest correlated with the original signal are shown, where it is possible to see a cyclostationary behavior where the cyclic frequency is lower than the shaft speed at 119*th* and 114*th* orders. For the sake of obtaining the order components, the SRCKF_OT free parameters were heuristically fixed as $q_i^a = 10^{-4}$, $q^f = 10^{-11}$, and $r = 10^{-12}$, in the DE198 case, whereas for DE130 the values were $q_i^a = 10^{-4}$, $q^f = 10^{-10}$, and $r = 10^{-11}$. As a result, 25 and 29 order components were extracted from DE130 and DE198, respectively.

As regards the SK comparison, the filtered signal with SK (left side) and the most relevant order component (right side) in accordance with the highest envelope correlation are displayed in Figs. 4.9 and 4.10. In the concrete case of DE130 (Fig. 4.9), it is observed that the $BPFO$ frequency, its harmonics and sidebands spaced at nf_r appears with a large ampli-

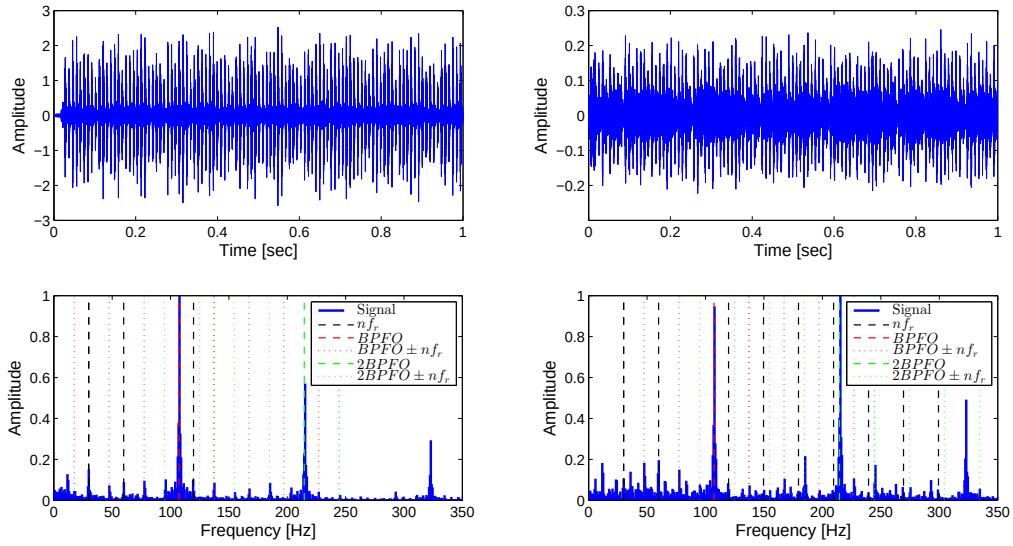

Figure 4.9: Identification of the BPFO frequencies on the envelope spectrum from DE130 using both SK (left) and proposed SRCKF_OT (right) approaches.

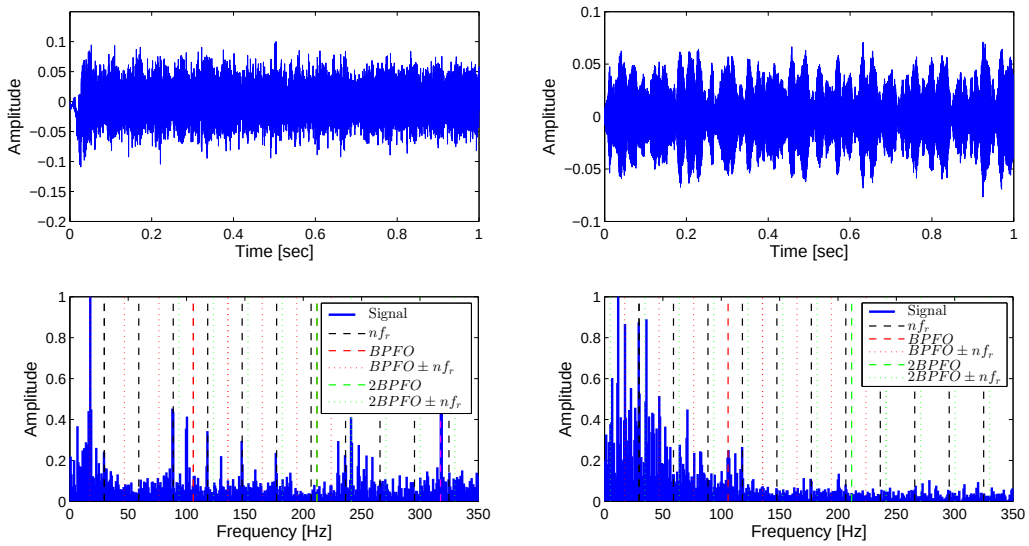

Figure 4.10: Identification of the BPFO frequencies on the envelope spectrum from DE198 using both SK (left) and proposed SRCKF_OT (right) approaches.

tude. The main difference between both approaches lies in the fact that the second harmonic of $BPFO$ is higher in the envelope spectrum (108*th*) obtained employing the proposed approach. Nonetheless, both SK and SRCKF_OT approaches are able to clearly diagnosis the outer race fault.

On the other hand, the blind signals extracted from the record DE198 using both approaches exhibit notable differences (see Fig. 4.10). In the case of SRCKF_OT, the 117*th* order com-

ponent gives the best signs of the outer race defect, which is characterized by a low frequency modulation associated to low sidebands of the frequencies $BPFO$ and $2BPFO$, i.e. the frequencies $BPFO - f_r$, $BPFO - 2f_r$, $BPFO - 3f_r$, $2BPFO - 6f_r$, and $BPFO - 7f_r$, and also, there is a spectral component that matches with $BPFO$, yet its amplitude is small. In contrast, the filtered signal with SK in time domain is similar to wide-band noise, but the envelope spectrum shows that the third harmonic of $BPFO$ appears as well as some sidebands like $BPFO - 3f_r$ and $2BPFO + f_r$. In conclusion, both methods exhibit some characteristics of the outer race fault, being potentially diagnosable (P2) according with the categories provided in Smith and Randall (2015).

Rolling element fault - BSF

In the case of rolling element defects, the BSE approaches are validated using the recordings DE188 (P2) and DE225 (N1). In particular, when the defect becomes large enough to allow movement of the shaft speed, the rolling element signal becomes modulated with the machine speed, generating a sideband to BSF at $\pm FTF$ (Taylor, 1994). Fig. 4.11 shows the analyzed records both in the time and frequency domains (top and middle rows), where it is possible to see that the impulsive behavior caused by the damage is a random process. This process in the case of record DE225 is virtually indistinguishable from noise, yet its spectrum shows a singular pattern of bearing faults at the frequency interval $[3.1 - 3.5]kHz$, and a modulation process at $48.1th$ order with the sidebands spaced at $\pm f_r = 28.82Hz$. Similarly, the record DE188 exhibits in its spectrum several characteristics of bearing faults like modulation processes localised at the frequency interval $[2.5 - 3.5]kHz$, and sidebands spaced $\pm n f_r = 28.73Hz$ (being $n = \{1, 2\}$) at the $48.2th$ and $146th$ orders.

In Fig. 4.11-(bottom row) the envelope correlation indexes computed between the order components and the raw signal are displayed. For the sake of estimating the order components, the covariances of SRCKF_OT were heuristically fixed as $q_i^a = 10^{-4}$, $q^f = 10^{-11}$, and $r = 10^{-12}$, in the DE225 case, whereas for DE188 the values were $q_i^a = 10^{-4}$, $q^f = 10^{-10}$, and $r = 10^{-11}$. As a result, 26 and 30 order components were extracted from DE188 and DE225, respectively. It is possible to see that the higher the impulsive behavior, the higher the envelope correlation; in consequence, the correlation indexes from the record DE188 are higher than the values in DE225.

The six order component with the highest envelope correlation is shown in Fig. 4.12, where the record DE225 evinces modulation processes governed by lower and upper frequencies than f_r, yet the interested order component is the $129th$ order. In the case of DE188, the order components concentrated at the frequency interval $[2.5 - 3.5]kHz$ are those related with the predominant modulation process, and because of the order components are so closer, these components are very similar in its waveform.

Afterwards, from the comparison between filtered signals by using both SK and SRCKF_OT,

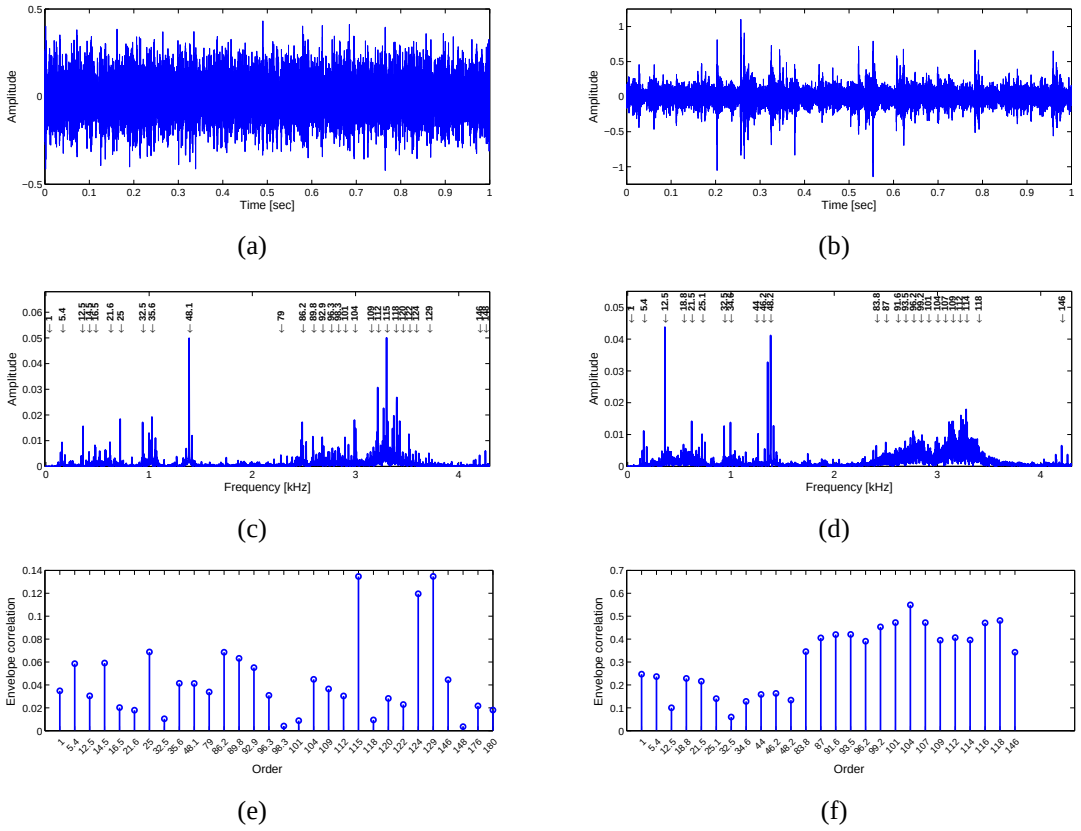

Figure 4.11: Recordings DE225 (left) and DE188 (right) in time domain (top row), frequency domain (middle row), and the envelope correlation indexes (bottom row).

it is possible to infer that the record DE188 is clearly diagnosable (Y2) since it depicts sidebands of the BSF and $2BSF$ spaced at $\pm FTF$, and multiple harmonics of FTF (see Fig. 4.13). It is worth noting that the filtered signal in time domain exhibits a similar waveform, yet the signal obtained with SK has a time delay concerning the outcome of the proposed approach.

When the approaches are applied to the record DE225, it is possible to see in Fig. 4.14 that the extracted signal using SK (left part) is not diagnosable (N1) as rolling element fault because there are no frequencies that match with BSF neither FTF in the envelope spectrum. On the contrary, the obtained component by SRCKF_OT scheme presents some characteristics of this type of fault like the BSF frequency, its sidebands spaced $\pm FTF$, and some low amplitude harmonics of the FTF. Moreover, sidebands of the BSF spaced at $\pm f_r$, and a dominant component associated with the shaft speed indicating that the outer race fault is masked by that frequency. In consequence, the record DE225 is probably diagnosable (P1) using the proposed approach since the envelope spectrum shows discrete components at the expected fault frequency but they are not dominant in the spectrum.

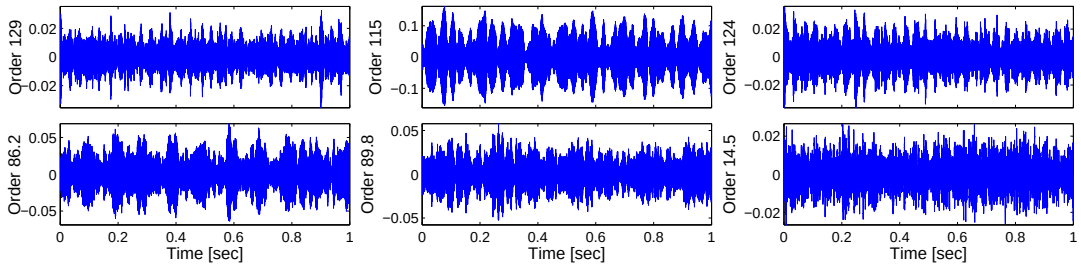

(a) Record DE225

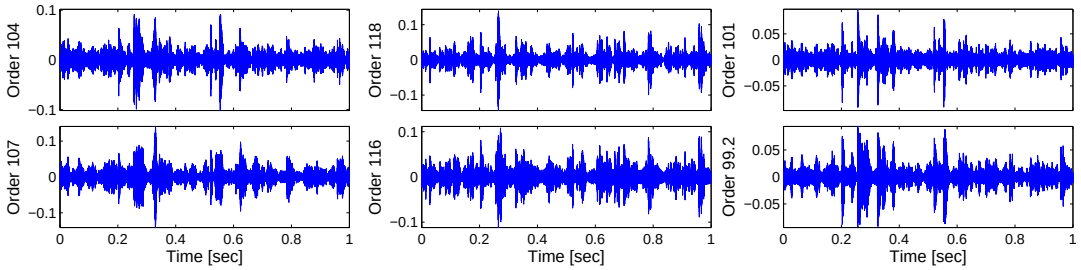

(b) Record DE188

Figure 4.12: Exemplary of the order components with the highest envelope correlation index for both rolling element recordings from CWRU data.

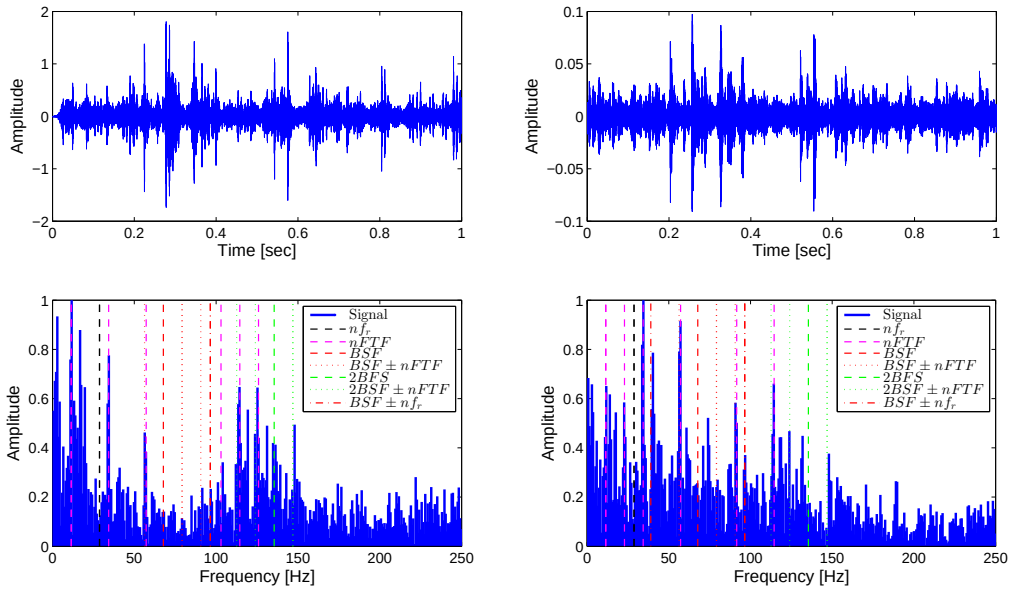

Figure 4.13: Identification of the BSF frequencies on the envelope spectrum from DE188 using both SK (left) and proposed SRCKF_OT (right) approaches.

In general, from this experiment it could be inferred that the obtained order components, using the proposed SRCKF_OT algorithm, comprise relevant information about the bearing

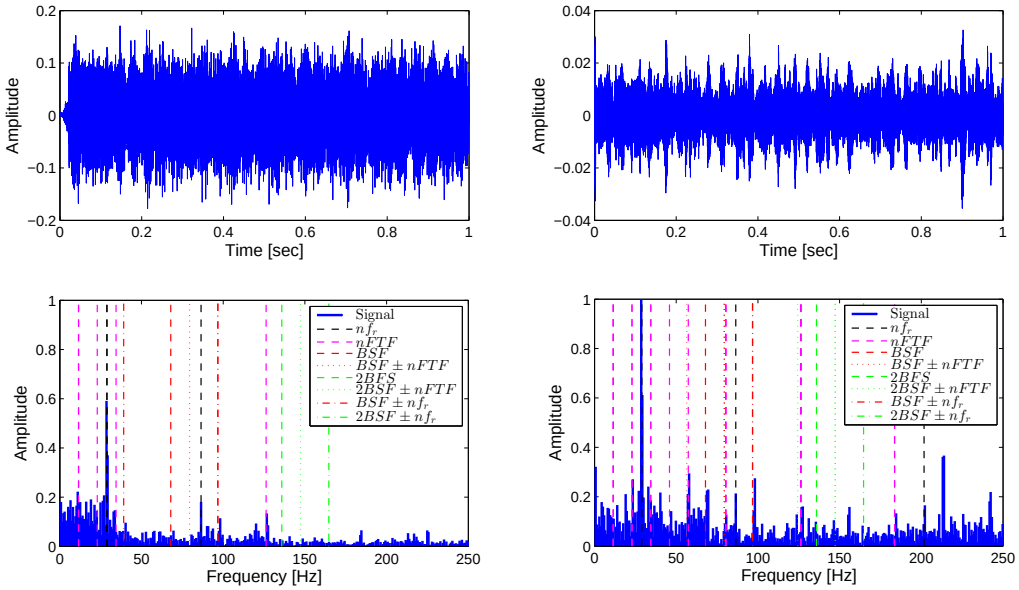

Figure 4.14: Identification of the BSF frequencies on the envelope spectrum from DE225 using both SK (left) and proposed SRCKF_OT (right) approaches.

faults and the modulation processes that occur in the vibration signal, which is very useful as a vibration analysis tool when the process is cyclostationary. In the case of the SK, the achieved results are consistent with the outcomes reported in Smith and Randall (2015), when the CWRU data are used.

4.4 Experiment on test rig 2: Universidad Nacional de Colombia data 2

The goal of this experiment consists of validating that the obtained components using the proposed OT model approach may extract cyclostationary signals hidden in the vibration signal, as well as to provide support to the novel OCC methodology presented in Chapter 3, in the sense, that it is possible detecting the spectral range where the faults appear. In that sense, from the dataset described in Section 3.5, each bearing fault signal both in the steady-state and dynamic regime are analyzed, where the fault frequencies are $BPFI = 5.4783 f_r$, $BPFO = 3.5217 f_r$, $BSF = 2.1913 f_r$, and $FTF = 0.3913 f_r$. Here, it is worth to notice that dynamic regime signals are transformed into the angle-order domain to perform the proposed model, since when the shaft speed presents large changes, e.g. coast-down, the bearing faults introduce cyclo-non-stationary processes that are characterized by AM-FM modulations. Therefore, the assumed model in the SRCKF_OT algorithm does not converge to track the instantaneous speed changes, and hence, the order components are wrongly

extracted. For that reason, the bearing fault signals under variable speed are analyzed after performing the angle domain transformation using Computed Order Tracking (COT) with the same conditions discussed in Section 3.5.2. It is important to highlight that COT may introduce errors in the domain transformation generated by the resampling, in consequence, the frequency slip can be higher.

As regards the identification of the bearing faults, each bearing fault signal is randomly selected, including each one by inner race, outer race, and rolling element defects. The following sections describe the analysis of the signals both the time and the angle domain, comparing the OT model approach with the SK.

Inner race fault - BPFI

In Fig. 4.15 the bearing fault signals are shown, where the left side displays the signal under steady-state regime in the time domain at $29.2Hz$. The right side presents the signal under dynamic regime in the angle domain (top row), being the shaft speed normalized to the $1th$ order. When the spectrum is computed (middle row), it is possible to see that frequency range is higher in the steady-state regime, because under dynamic regime the signal is resampled at 32 orders, which implies that the spectral range is $[0 - 1000]Hz$ approximately. In the steady-state regime case, the spectrum exhibits an inner race fault characteristic components concentred at the interval $[3.2 - 4]kHz$ where there are the majority of order components to be tracked. In change, the order spectrum has a few components between the $10th$ and the $15th$ order which manifest the fault conditions. Nonetheless, there is no a clear pattern about the considered defect in both spectra.

The envelope correlation indexes (Fig. 4.15-bottom row) allow inferring that in steady-state regime is clear extracting a component that shows the damage because the envelopes are highly correlated with the raw signal. However, in the dynamic case, the correlation does not overcome 0.5, and the most correlated components are in medium and low frequency, reducing the possibilities to find the $BPFI$ frequency.

Aiming to estimate the order components depicted in the spectra, the covariances of the SRCKF_OT algorithm were fixed as $q_i^a = 10^{-3}$, $q^f = 10^{-8}$, and $r = 10^{-9}$ in the steady-state regime, while in the dynamic were $q_i^a = 10^{-2}$, $q^f = 10^{-5}$, and $r = 10^{-9}$. As a result, 27 and 18 order components were obtained, from which the six more correlated are display in Fig. 4.16. Here, the order components present an impulsive behavior under steady-state regime, yet in coast-down that behavior is not clearly appreciated in the highest correlated components. Nonetheless, an inspection of the envelope spectrum of the order $5.4th$ allows to determine the existence of the inner race fault. Besides, that order is related with the $BPFI$ frequency normalized by the shaft speed f_r.

Afterward, the comparison of the BSE approaches for the bearing fault signal under steady-state regime is shown in Fig. 4.17. It is observed that both methods distinguish the inner

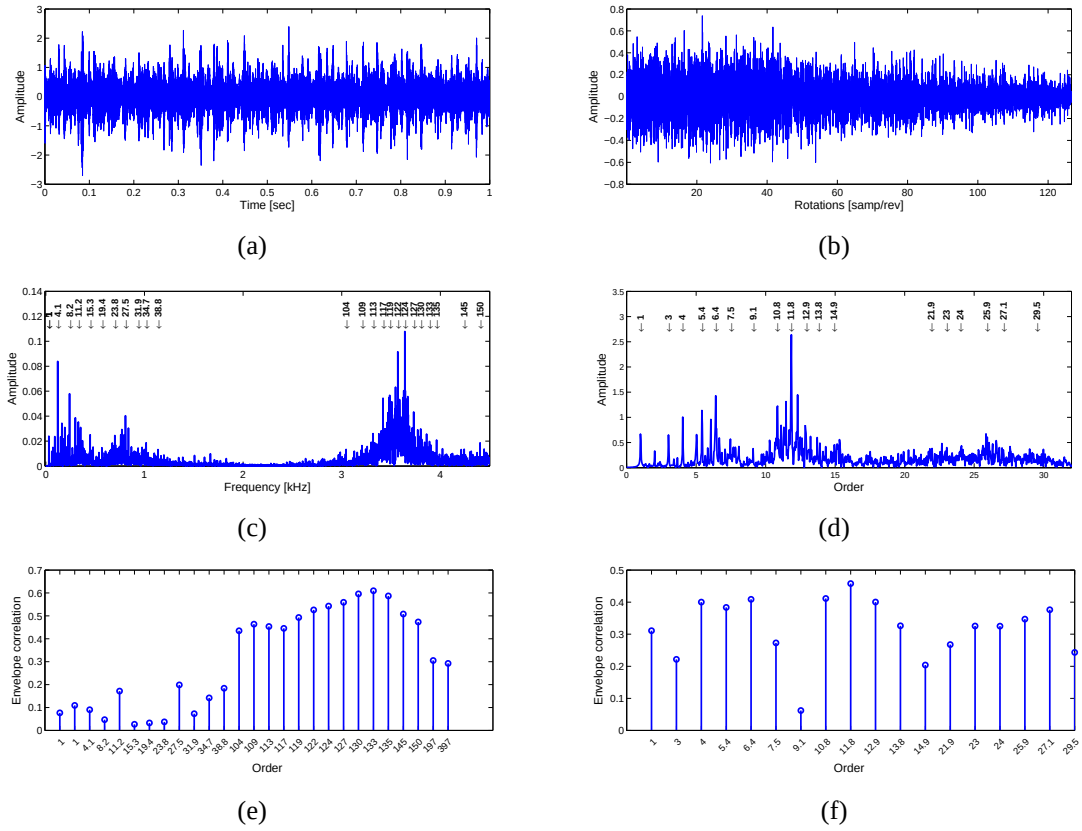

Figure 4.15: Recordings of inner race fault under steady-state (left) and dynamic (right) regimes in time domain (top row), frequency domain (middle row), and the envelope correlation indexes (bottom row).

race fault since the $BPFI$ and its harmonics are clearly identified in the envelope spectra. Furthermore, spectral components associated with the sidebands of $BPFI$ and harmonics of the shaft speed are also detected with a high amplitude, which indicates that the spall size generated on the inner race is an advanced stage.

The notable difference between SK and SRCKF_OT is found in the analysis of the bearing fault signal under the dynamic regime (see Fig. 4.18). Here, the state-of-the-art method (left side) overcomes to the proposed approach because of it exhibits, with a proper amplitude, the spectral components associated with $BPFI$ and several sidebands like $BPFI + f_r$. Nevertheless, the order component with highest envelope correlation also shows the same fault frequencies, but the amplitude is very low.

Outer race fault - BPFO

In this experiment, the analyzed bearing fault signals do not present a clear impulsive components in the time and angle domain under both steady-state and dynamic regimes (see Fig. 4.19-

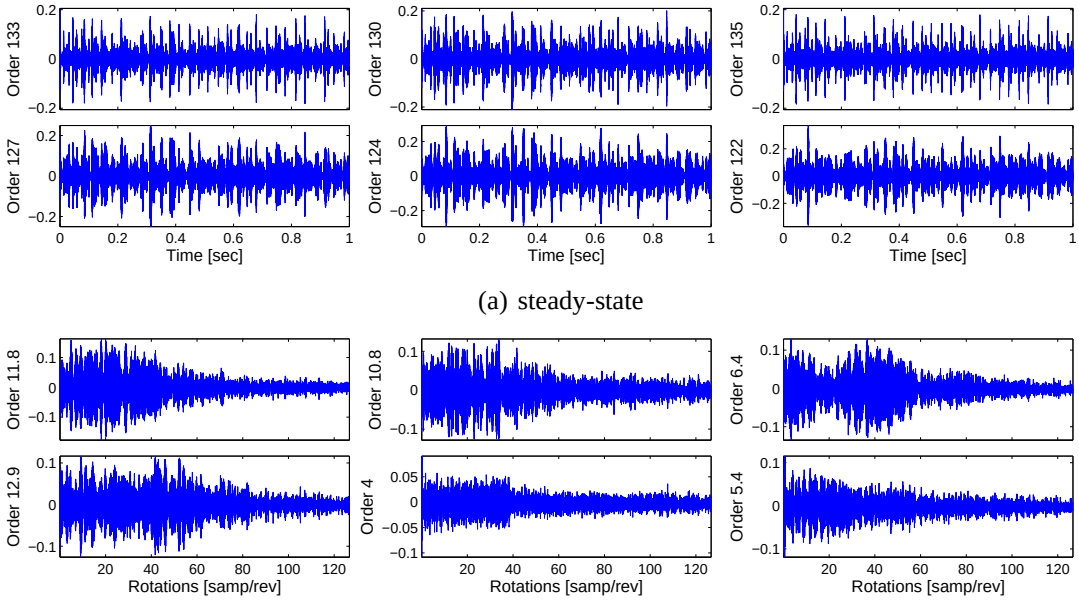

(a) steady-state

(b) Dynamic

Figure 4.16: Exemplary of the order components with the highest envelope correlation index for both inner race fault recordings under different regimes from UN-2 data.

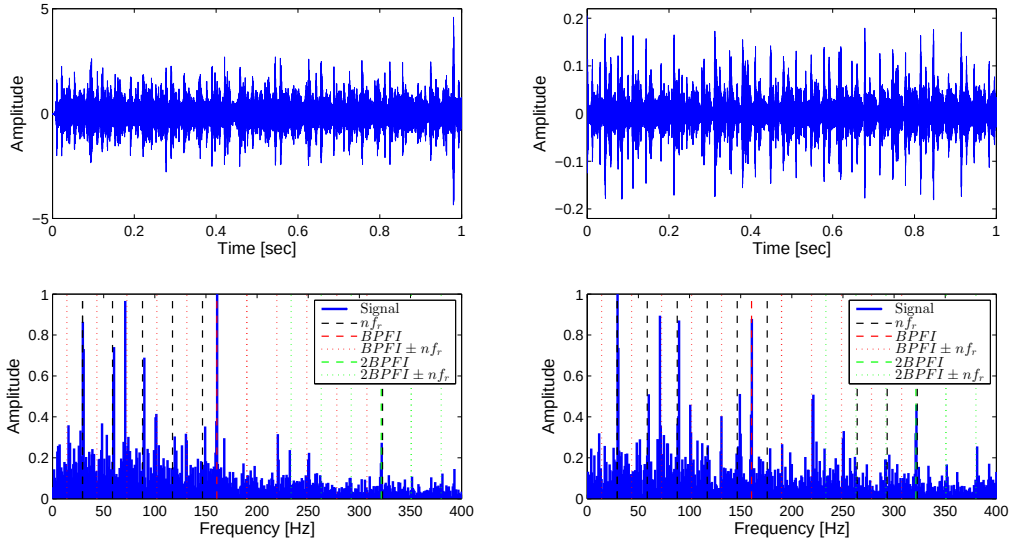

Figure 4.17: Identification of the BPFI frequencies on the envelope spectrum from bearing fault signal under steady-state regime, using both SK (left) and proposed SRCKF_OT (right) approaches.

top row), and hence, the signals may be confused with the undamaged state. In the case of the steady-state regime displayed in the left side of the Fig. 4.19, the spectrum is concentrated in a low frequency range and does not show modulation processes in high frequency,

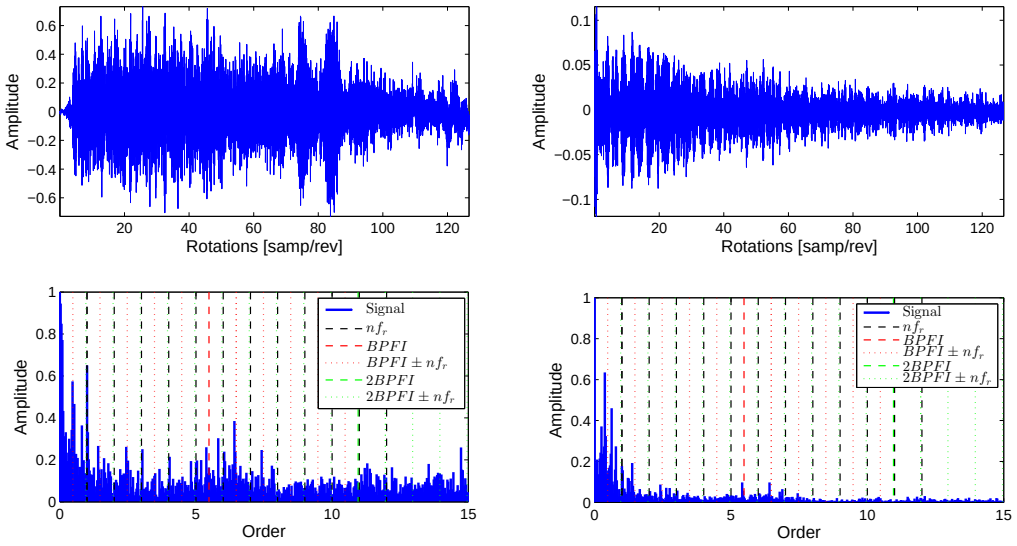

Figure 4.18: Identification of the BPFI frequencies on the envelope spectrum from bearing fault signal under dynamic regime, using both SK (left) and proposed SRCKF_OT (right) approaches.

indicating that the fault could be incipient, or the spall size is slight. Especially, the highest spectral component is the 4.1*Hz* order that corresponds to a characteristic frequency of the electromotor, i.e. the number of poles by the shaft speed that is 120*Hz* approx. The lack of modulations is verified in the envelope correlations (bottom row) between the extracted components and the raw signal, since the reached values are under 0.2. Unfortunately, that correlation values imply that the extracted order components do not comprise a well-defined cyclostationary processes or AM modulations generated by cyclic frequencies.

Similarly, when the machine operates under dynamic regime, the bearing signal spectrum (Fig. 4.19-right side) evinces spurious spectral components that try to emulate modulation processes at between the orders 18*th* and 21*th*. This fact could also be appreciated in the envelope correlation indexes because that order range comprises the highest correlation, improving the achieved values 0.15 compared with the correlations in the steady-state regime.

For the sake of estimating the set of order components using the SRCKF_OT approach, the harmonics depicted on the signal spectra are used, obtaining a total of 33 and 22 components from the bearing signals under the steady-state and dynamic regime, respectively. Moreover, the covariance parameters of the algorithm were heuristically fixed as $q_i^a = 10^{-3}$, $q^f = 10^{-8}$, and $r = 10^{-9}$ in the steady-state regime, whereas in the dynamic regime the parameters were $q_i^a = 10^{-2}$, $q^f = 10^{-5}$, and $r = 10^{-9}$. As a result, the six components more correlated with the raw signal are shown in Fig. 4.20. It is possible to see that the extracted components in the steady-state regime (Fig. 4.20(a)) have a slight impulsive behavior and are governed by an AM modulation that in some cases are cyclostationary, for instance, in the order 39.4*th*. A similar behavior is observed in the dynamic regime (Fig. 4.20(b)), yet the modulator signal

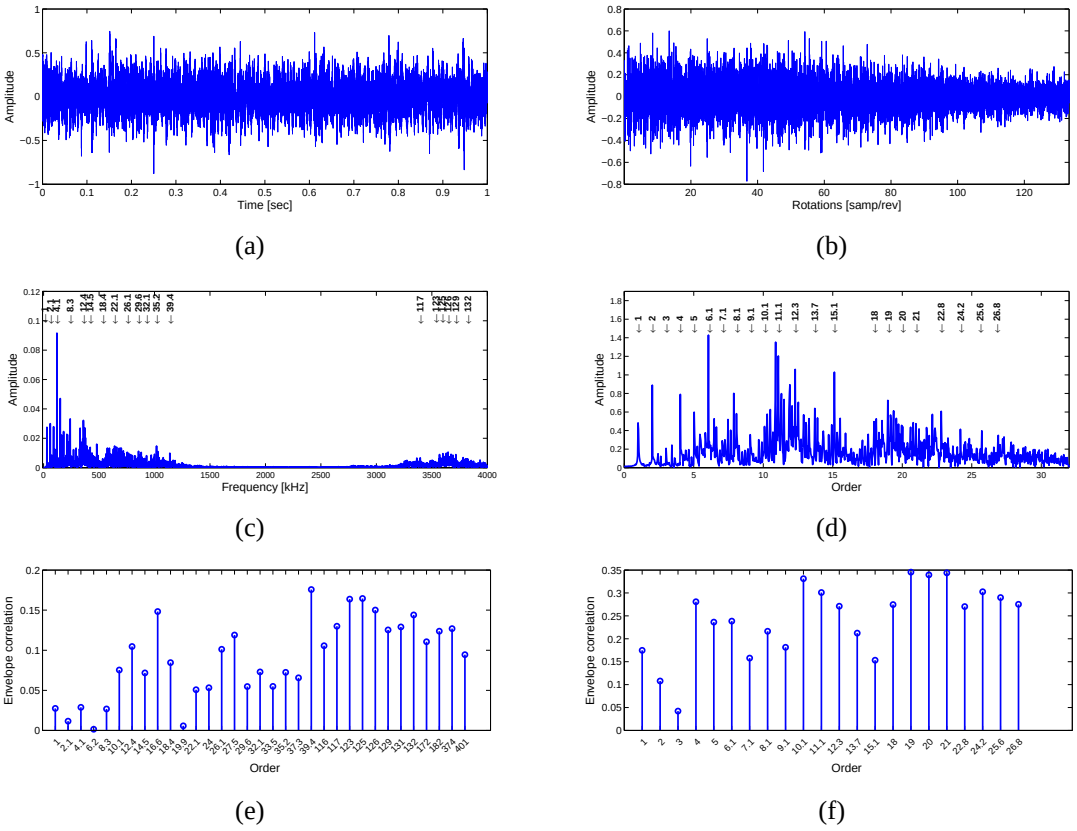

Figure 4.19: Recordings outer race fault under steady-state (left) and dynamic (right) regimes in time domain (top row), frequency domain (middle row), and the envelope correlation indexes (bottom row).

that dominates the cyclicity has a lower frequency.

In the concrete case of the outer race frequency identification in the envelope spectra, the bearing signal under steady-state regime (Fig. 4.21) shows a periodical impact each $1/6sec$ at time domain, which is also observed in the envelope spectrum since the dominant components are spaced by $6Hz$. That behavior may be better appreciated in the filtered signal with SK than with the proposed approach, however, that component does not provide any information about the analyzed fault, and hence, it acts like a mask that hides the outer race fault frequency. Nonetheless, some characteristic patterns of this type of fault may be found in the envelope spectrum such as the $BPFO$ frequency and the first sidebands $BPFO \pm f_r$.

In the dynamic regime presented in Fig. 4.22, it is complicated distinguishing the outer race fault characteristics due to inaccuracies generated during the angle domain transformation (i.e. vagueness caused by COT). Nevertheless, the cyclicity exposed by the filtered signal using SRCKF_OT (right side) allows inferring the existence of modulations that could be related to the studied fault. In that sense, it is possible to detect some spectral components that match mainly with the lower sidebands of the $BPFO$ frequency. On the contrary, despite

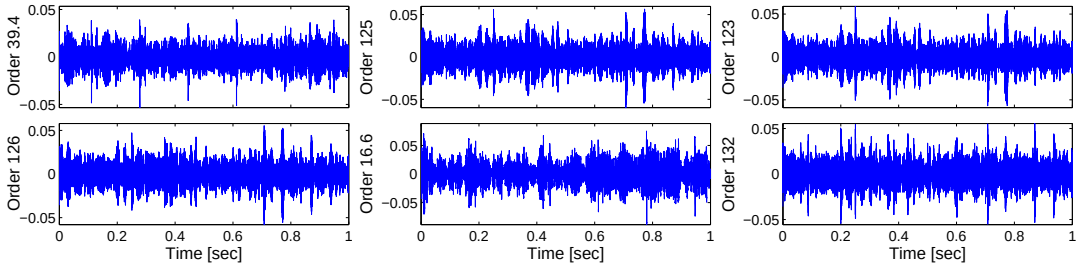

(a) steady-state

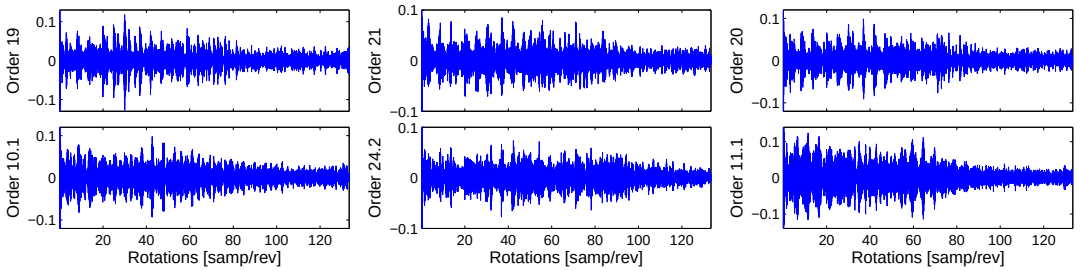

(b) Dynamic

Figure 4.20: Exemplary of the order components with the highest envelope correlation index for both outer race fault recordings under different regimes from UN-2 data.

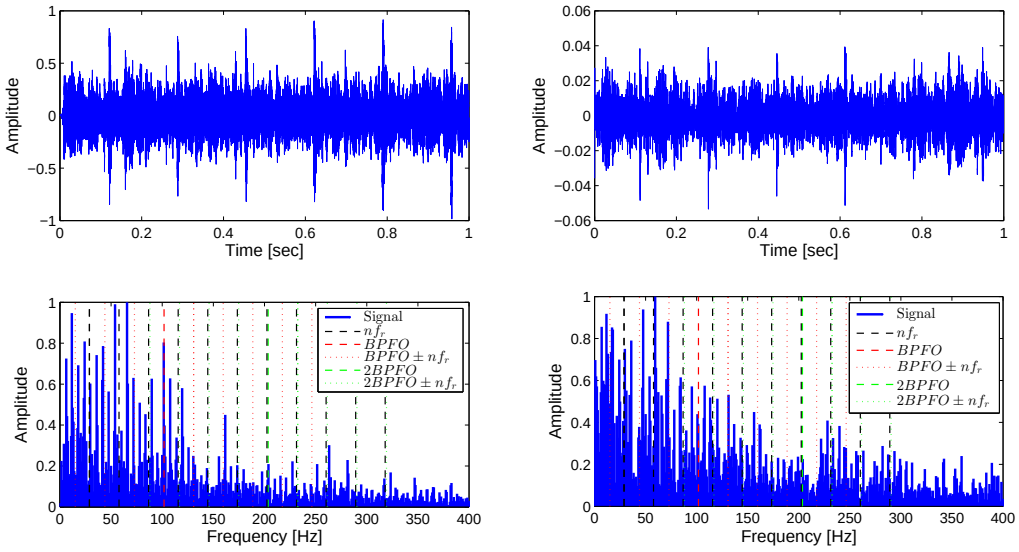

Figure 4.21: Identification of the BPFO frequencies on the envelope spectrum from bearing fault signal under steady-state regime, using both SK (left) and proposed SRCKF_OT (right) approaches.

the signal filtered by SK (left side) in angle domain does not allow perceiving an outer race defect pattern, yet the envelope spectrum depicts some low amplitude spectral components that match with the sidebands of $BPFO$.

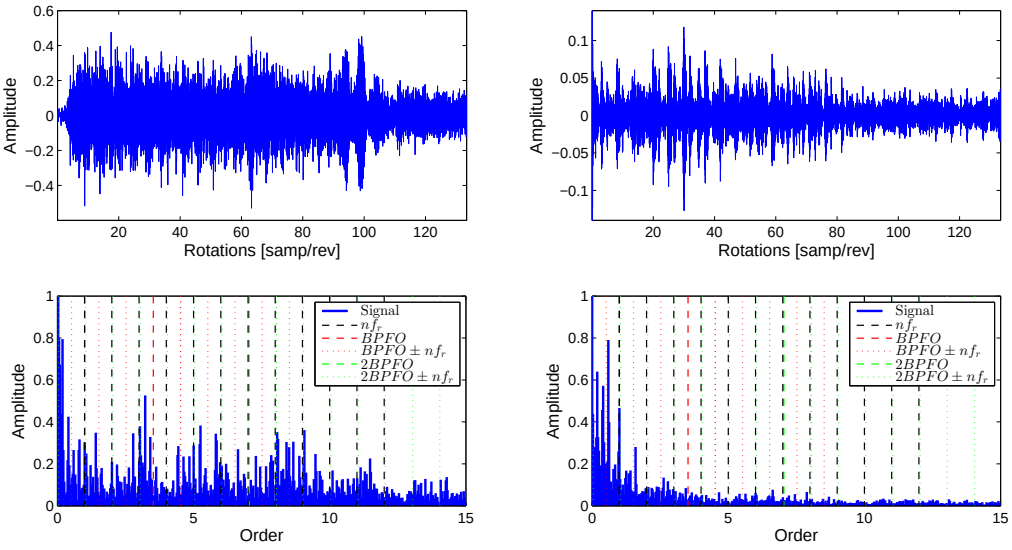

Figure 4.22: Identification of the BPFO frequencies on the envelope spectrum from bearing fault signal under dynamic regime, using both SK (left) and proposed SRCKF_OT (right) approaches.

Rolling element fault - BSF

Fig. 4.23 shows the respective bearing signals under the steady-state (left column) and dynamic regimes (right column), in time and angle domain (top row), their corresponding spectra (middle row), and the envelope correlation values obtained between each order component and the raw signal (bottom row). Firstly, it is observed that the signal in steady-state regime exhibits a clear cyclostationary behavior, whereas in dynamic regime the signal also depicts an impulsive behavior, and in both cases those signs are characteristics of a bearing defect.

Secondly, the spectrum of each regime displays particular spectral components that confirm the information observed in the time and angle domains. Particularly, the spectrum of steady-state regime has representative spectral components at the intervals $[3.2-4]$ and $[5.5-6]kHz$, which commonly are associated to bearing faults. At the same way, there are several lobes in the order spectrum at the order intervals $[10-15]$ and $[25-30]$, which gives some clues about the damage.

Lastly, the envelope correlation indexes allow to establish frequency bands where there are more modulated components, where it is worth to highlight the high correlation values, in the steady-state regime, between the $11.9th$ and the $13.6th$ orders. Conversely, the correlation values in the dynamic regime are acceptable, taking into account that the signal has been resampled, and hence, the highest components may last from the $5.4th$ to $25.6Hz$.

The $5.4th$ order is very particular because it exhibits a modulation generated by a low frequency that corresponds to FTF. Nonetheless, since the idea is to find the order compo-

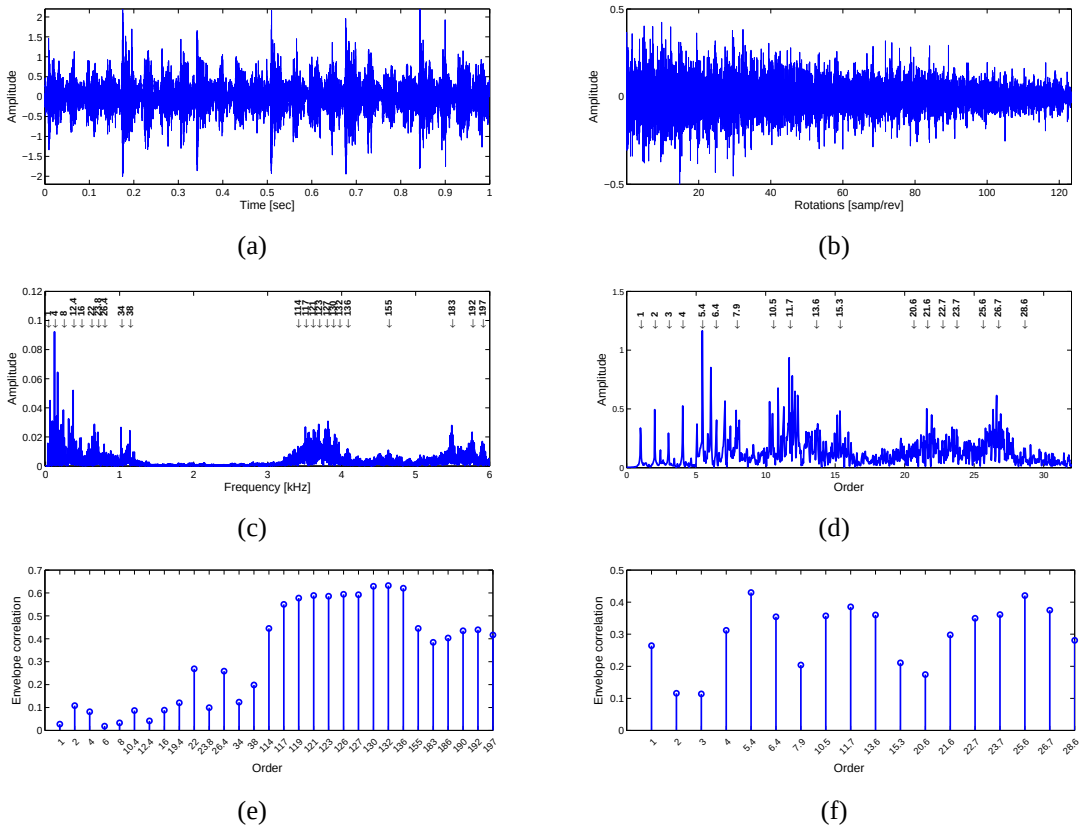

Figure 4.23: Recordings rolling element fault under steady-state (left) and dynamic (right) regimes in time domain (top row), frequency domain (middle row), and the envelope correlation indexes (bottom row).

nent that better describes the rolling element defect, by visual inspection the 13.6*th* order is selected from the six orders with the highest envelope correlation (see Fig. 4.24(b)). Concerning to the steady-state regime the six order components more correlated with the raw signal display a similar behavior, being characteristic a periodic impact spaced at $1/6sec$. The mentioned above order components where estimated fixing the covariance parameters of the SRCKF_OT algorithm as order components, $q_i^a = 10^{-3}$, $q^f = 10^{-8}$, and $r = 10^{-9}$, and $q_i^a = 10^{-3}$, $q^f = 10^{-6}$, and $r = 10^{-10}$, obtaining a total of 30 and 18 components from the bearing signals under steady-state and dynamic regimes, respectively.

As regards the identification of the outer race fault, both tested approaches achieve successfully to detect the BSF frequency and multiple harmonics of the FTF, when the machine operates in steady-state regime (Fig. 4.25). Besides, the visualization of sidebands at $\pm FTF$ and $\pm f_r$ are signs that the defect is an advanced stage. In contrast, when the bearing fault signal under dynamic regime is analyzed (Fig. 4.26), it is found that the proposed scheme reaches detecting more symptoms about the outer race fault than the SK. In consequence, it is possible to see in the envelope spectrum, obtained from an order component (right col-

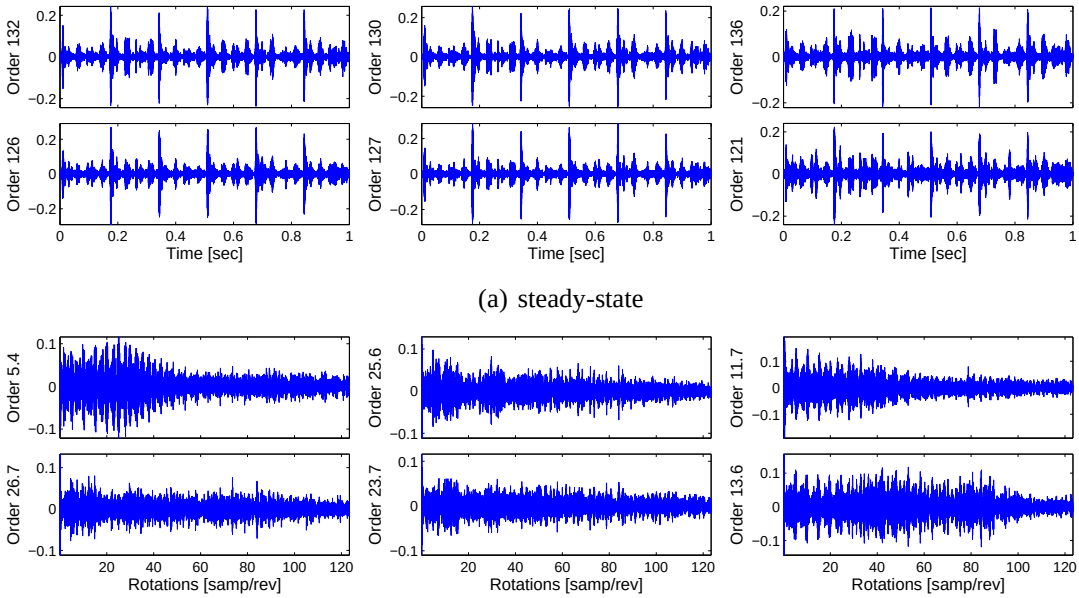

(a) steady-state

(b) Dynamic

Figure 4.24: Exemplary of the order components with the highest envelope correlation index for both rolling element recordings under different regimes from UN-2 data.

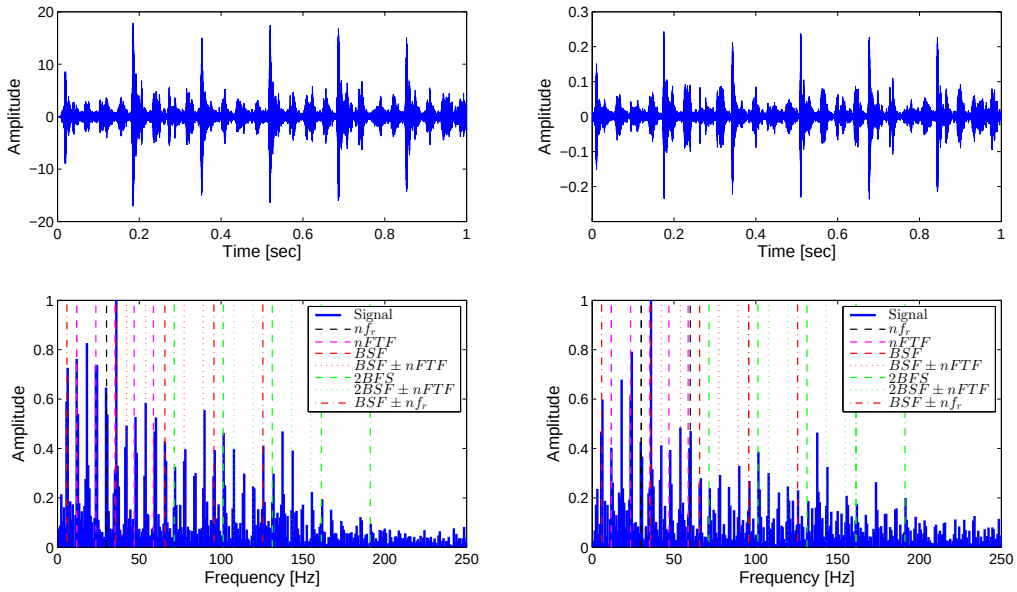

Figure 4.25: Identification of the BSF frequencies on the envelope spectrum from bearing fault signal under steady-state regime, using both SK (left) and proposed SRCKF_OT (right) approaches.

umn), the BSF frequency together with several inferior sidebands, and multiple harmonics of FTF, being this the dominant frequency. In change, the envelope spectrum, of the filtered

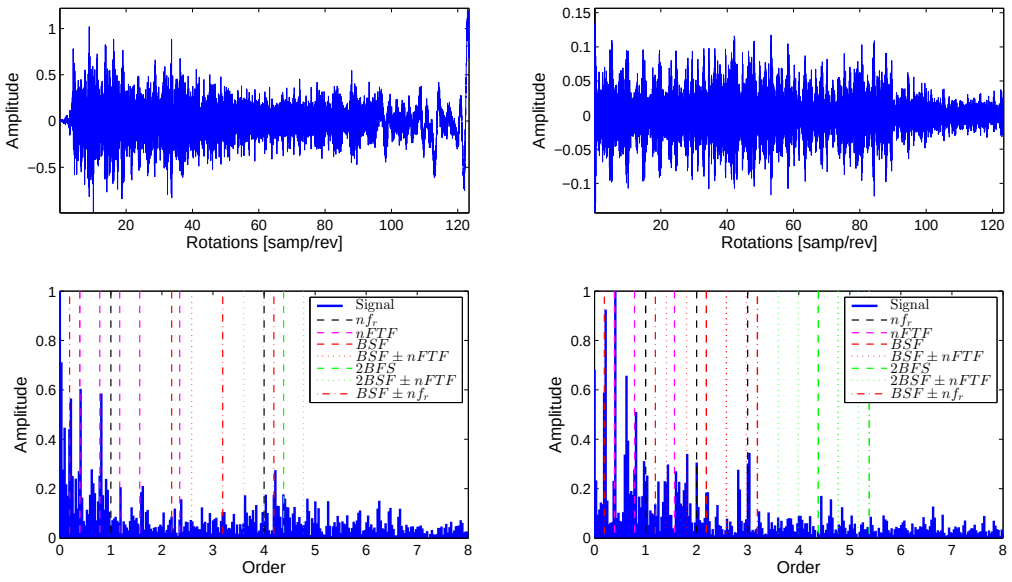

Figure 4.26: Identification of the BSF frequencies on the envelope spectrum from bearing fault signal under dynamic regime, using both SK (left) and proposed SRCKF_OT (right) approaches.

signal with SK (left column), shows only frequencies that match with the FTF frequency and its harmonics.

4.5 Discussion

The obtained results from the experiments presented above provide several aspects to highlight about the studied BSE approaches, taking into account that both methods in most of the analyzed cases were correctly extracting cyclostationary components associated with bearing faults.

On the one hand, Smith and Randall (2015) recommends that new diagnostic algorithms must demonstrate the relative advantages against the benchmark results that they reported, it is chosen the SK filter as the reference approach. In spite of the bearing fault detection methodology does not include the signal preprocessing using the widely-known Discrete/Random Separation algorithm, it is showed that by using the SK is possible to assign the categories provided. Here, it is important to notice that the BSE approaches were tested in two different types of bearing fault signals, that in our terms are considered as the clear and not diagnosable. In that sense, considering the conditions that the cited authors proposes to determine the improvement of the bearing fault detection, using the proposed approach it is possible to change from a partial or not diagnosable to probably or clearly diagnosable in some cases. For instance, the record DE198 changes from N2 to P2, the DE188 from P2 to Y2, and the DE225 from N1 to P1. Nonetheless, regarding the computational efficiency, SK

is better than the proposed approach because it performs the analysis in less computing time, considering that the SRCKF_OT algorithm is still tested in Matlab© and the computational cost depends on the number of order components that are tracked. Besides, SK is plug and play whereas the proposed algorithm still requires the tuning of several parameters such as the number of harmonics K and the covariances of the Kalman recursion.

On the other hand, the experiment considering both steady-state and dynamic regimes show that both approaches (SK and SRCKF_OT) provide the needed elements to diagnose the bearing faults. Nevertheless, in the especial case where the shaft speed is varying, both methods are complementary in the sense that the variable speed component could be estimated using the SRCKF_OT applied to the low-frequency range where the order components preserve the smooth amplitude change condition. Then, the signal is transformed into the angle domain using COT, and the SK filter the signal to extract the cyclostationary component that evinces the bearing fault.

Regarding with the obtained results in the Chapter 3, where the order components of the bearing signals (described in Section 4.4) were classified and labeled as targets or outliers, it is possible to confirm that effectively the outlier components exhibit some characteristic of the either inner race, outer race or rolling element. In that sense, it was found that the frequency-located OCC methodology allows to obtain a spectral range where the fault exists, and then, if the envelope spectrum of the outliers is computed, it is possible to identify characteristic patterns from the bearing faults. In spite of there are other approaches that also provides an informative frequency band about the fault, the proposed methodology could indicates both shaft and bearing defects. The study of gear defects is considered as future work because that topic is out of the scope of this work.

5 Conclusions and future work

This work proposes novel machine diagnostic strategies that are focused on the processing of non-stationary vibration signals, with the aim of providing practical and implementable analysis tools in the industry. In that sense, it was discussed a diagnostic methodology that isolates, detects and identifies several faulty conditions as the faults on the shaft and the rolling element bearings. Particularly, the methodology follows the estimation of the instantaneous speed and the relevant spectral components from the machine, the detection of the faulty condition, and the identification of the particular fault. In that sense, the concluding remarks are described:

- A novel order tracking approach termed SRCKF_OT, that allows estimating the multiple spectral/order components simultaneously together with the instantaneous frequency was presented. The performance of the proposed approach is validated both two laboratory tests and four case studies, providing the following advantages: *i)* distinguishing closed-order components; *ii)* estimating the instantaneous speed under different speed variations comprising, start-up, coast-down, and speed fluctuations as in the case of the wind turbine; *iii)* estimating narrow-band spectral components that may exhibit stationary and cyclostationary processes. Nonetheless, when cyclic components are governed by a variable speed the tracking fails, yet, in this case, the proposed SRCKF_OT could still estimate the shaft speed if the signal is downsampled until reaching only $5th$ order. In general, the proposed OT model is a preprocessing interesting tool that may describe the overall characteristics of a machine.

- A novel OCC methodology, called *frequency-located fault detection* that allow detecting the frequency band where the fault exists was presented. To this end, a set of dynamic features, estimated by SRCKF_OT, describe the narrow-band spectral properties of the signal allowing to determine the existence and the frequency range of the fault. This kind of information is relevant for machine operator without much experience in vibration analysis, reducing the time to find the faulty process and improving the maintenance capabilities. The methodology was tested for different types of data including unbalance and misalignment under start-up and coast-down operating conditions, and bearing fault detection under permanent and coast-down regimes.

- A methodology to extract blind signals from mechanical vibrations was presented. The method is based on the cyclostationary properties of the narrow-band spectral

components obtained using SRCKF_OT, allowing identifying the fault frequencies that characterize the bearing failures. The achieved results were compared with the state-of-the-art BSE approach so-called spectral kurtosis, showing that our methodology is comparable, and in some cases, it provides a more comprehensive information than SK.

Regarding the future work, there are some issues that can be addressed to improve the proposed machine diagnostic framework, including the following considerations:

- Since the free parameters of the proposed SRCKF_OT approach are heuristically fixed, an issue of study is focused on the design and implementation of optimization methods that allow estimating those parameters from the vibration signal. This fact will reduce the time to obtain the best filter response. It is worth noting that the study of Kalman filtering is a current research field since the algorithm convergence depends on the estimation of correct parameters.

- The analysis of cyclostationary processes when the machine operating conditions are time-varying has a growing interest in the condition monitoring community, and in that sense, we consider the improvement of the proposed SRCKF_OT approach to extract both instantaneous frequency (without downsampling) and the cyclostationary order components under speed fluctuations.

- As regards the OCC methodology, it is important the analysis of the different machine faults like gears, complex machines, and the validation of the method for real-world applications. This fact will allow increasing the probability of transforming the machine diagnostic methodology in a tool useful in the industry.

6 Academic discussion

6.1 Journal and conference papers

Journal papers

2014:

[1]. O. Cardona-Morales, L.D. Avendaño, G. Castellanos-Dominguez. *"Nonlinear Model for Condition Monitoring of Non-stationary Vibrations Signals in Ship Driveline Application"*. In: Mechanical Systems and Signals Processing.

2013:

[1]. O. Cardona Morales, D. A. Alvarez Marin, G. Castellanos-Dominguez. *"Outlier detection in rotating machinery under non-stationary operating conditions using dynamic features and one-class classifier"*. In: Dyna.

[2]. O. Cardona-Morales, E.F. Sierra-Alonso, G. Castellanos-Dominguez. *"Identification of wind turbine natural frequencies using narrow-band decomposition methods"*. In: Insight-Non-Destructive Testing and Condition Monitoring.

Book chapter

2016:

[1]. O. Cardona-Morales, E.F Sierra-Alonso, G. Castellanos-Dominguez. *"Blind Extraction of Instantaneous Frequency for Order Tracking in Rotating Machines Under Non-stationary Operating Conditions"*. In: Advances in Condition Monitoring of Machinery in Non-Stationary Operations.

2014:

[1]. E. F. Sierra-Alonso, O. Cardona-Morales, C. D Acosta-Medina, G. Castellanos-Dominguez. *"Spectral Correlation Measure for Selecting Intrinsic Mode Functions"*. In: Progress in Pattern Recognition, Image Analysis, Computer Vision, and Applications.

[2]. H. Fandiño-Toro, O. Cardona-Morales, C. Garcia-Alvarez, G. Castellanos-Dominguez. *"Bearing fault identification using watershed-based thresholding method"*. In: Advances in Condition Monitoring of Machinery in Non-Stationary Operations.

[3]. O. Cardona-Morales, D. Alvarez-Marin, G. Castellanos-Dominguez. *"Condition monitoring under non-stationary operating conditions using time-frequency representation-based dynamic features"*. In: Advances in Condition Monitoring of Machinery in Non-Stationary Operations.

Conference papers

2013:

[1]. O. Cardona-Morales, C. Aguirre-Echeverry, G. Castellanos-Dominguez. *"Outlier detection in rotating machinery combining optimized one-class classifiers"*. In: The Tenth International Conference on Condition Monitoring and Machinery Failure Prevention Technologies. CM2013 and MFPT2013. Krakow, Poland.

[2]. O. Cardona-Morales, E.F. Sierra-Alonso, G. Castellanos-Dominguez. *"Identification of wind turbine natural frequencies using narrow-band decomposition methods"*. In: The Tenth International Conference on Condition Monitoring and Machinery Failure Prevention Technologies. CM2013 and MFPT2013. Krakow, Poland.

2011:

[1]. O. Cardona-Morales, E.F. Sierra-Alonso, G. Castellanos-Dominguez. *"Estudio comparativo entre algoritmos adaptativos para seguimiento de orden en señales de vibracion"*. In: Simposio de Tratamiento de Señales, Imágenes y Visión Artificial. XVI STSIVA 2011. Cali, Colombia.

[2]. O. Cardona-Morales, L. Avendaño-Valencia, G. Castellanos-Dominguez. *"Instantaneous frequency estimation and order tracking based on Kalman filters"*. In: International Operational Modal Analysis. IOMAC2011. Istanbul, Turkey.

6.2 Awards

2014 Espíritu Innovador. Universidad Nacional de Colombia – Manizales.

2013 "The Len Gelman Award" for the best paper published in the Proceedings of the Institute's Condition Monitoring Conference CM 2013/MFPT 2013 by a person in the early stages of their career. The British Institute of Non-Destructive Testing.

2013 Finalist in the PHM2013, Doctoral Symposium. Annual Conference of the PHM Society.

Bibliography

Abboud, D., Antoni, J., Sieg-Zieba, S., and Eltabach, M. (2016). Deterministic-random separation in nonstationary regime. *Journal of Sound and Vibration*, 362:305 – 326.

Alves, D. and Coelho, R. (2010). An adaptive real-time multi-tone estimator and frequency tracker for non-stationary signals. In *Real Time Conference (RT), 2010 17th IEEE-NPSS*, pages 1 –7.

Antoni, J. (2005). Blind separation of vibration components: Principles and demonstrations. *Mechanical Systems and Signal Processing*, 19(6):1166 – 1180. Blind Source Separation.

Antoni, J. (2006). The spectral kurtosis: a useful tool for characterising non-stationary signals. *Mechanical Systems and Signal Processing*, 20(2):282 – 307.

Antoni, J. (2007a). Cyclic spectral analysis of rolling-element bearing signals: Facts and fictions. *Journal of Sound and Vibration*, 304(3–5):497 – 529.

Antoni, J. (2007b). Fast computation of the kurtogram for the detection of transient faults. *Mechanical Systems and Signal Processing*, 21(1):108 – 124.

Antoni, J. (2009). Cyclostationarity by examples. *Mechanical Systems and Signal Processing*, 23(4):987 – 1036.

Antoni, J. and Randall, R. (2006). The spectral kurtosis: application to the vibratory surveillance and diagnostics of rotating machines. *Mechanical Systems and Signal Processing*, 20(2):308 – 331.

Arasaratnam, I. and Haykin, S. (2011). Cubature Kalman smoothers. *Automatica*, 47(10):2245 – 2250.

Arasaratnam, I., Haykin, S., and Hurd, T. (2010). Cubature Kalman filtering for continuous-discrete systems: Theory and simulations. *Signal Processing, IEEE Transactions on*, 58(10):4977 –4993.

Avendano-Valencia, L., Avendano, L., Ferrero, J., and Castellanos-Dominguez, G. (2007). Improvement of an extended Kalman filter power line interference suppressor for ECG signals. *Computers in cardiology*, 34:553–556.

Bai, M., Huang, J., Hong, M., and Su, F. (2005). Fault diagnosis of rotating machinery using an intelligent order tracking system. *Journal of sound and vibration*, 280:699–718.

Barszcz, T. and JabŁoński, A. (2011). A novel method for the optimal band selection for vibration signal demodulation and comparison with the kurtogram. *Mechanical Systems and Signal Processing*, 25(1):431 – 451.

Barszcz, T. and Randall, R. B. (2009). Application of spectral kurtosis for detection of a tooth crack in the planetary gear of a wind turbine. *Mechanical Systems and Signal Processing*, 23(4):1352 – 1365.

Bartkowiak, A. and Zimroz, R. (2011). Outliers analysis and one class classification approach for planetary gearbox diagnosis. *Journal of Physics: Conference Series*, 305(1):012031.

Bishop, C. (1995). *Neural Networks for Pattern Recognition*. Oxford University Press, Walton Street, Oxford OX2 6DP.

Bittanti, S. and Saravesi, S. (2000). On the parameterization and design of an extended Kalman filter frequency tracker. *IEEE trans. Automatic control*, 45.

Bonnardot, F., Randall, R., and Guillet, F. (2005). Extraction of second-order cyclostationary sources—application to vibration analysis. *Mechanical Systems and Signal Processing*, 19(6):1230 – 1244. Special Issue: Blind Source Separation.

Borghesani, P. (2015). The envelope-based cyclic periodogram. *Mechanical Systems and Signal Processing*, 58–59:245 – 270.

Borghesani, P., Pennacchi, P., Randall, R., and Ricci, R. (2012). Order tracking for discrete-random separation in variable speed conditions. *Mechanical Systems and Signal Processing*, 30(0):1 – 22.

Borghesani, P., Ricci, R., Chatterton, S., and Pennacchi, P. (2013). A new procedure for using envelope analysis for rolling element bearing diagnostics in variable operating conditions. *Mechanical Systems and Signal Processing*, 38(1):23 – 35. Condition monitoring of machines in non-stationary operations.

Boustany, R. and Antoni, J. (2005). Cyclic spectral analysis from the averaged cyclic periodogram. In *Proceedings of IFAC*, volume 5.

Caesarendra, W., Kosasih, B., Tieu, A. K., and Moodie, C. A. (2015). Application of the largest Lyapunov exponent algorithm for feature extraction in low speed slew bearing condition monitoring. *Mechanical Systems and Signal Processing*, 50 - 51:116 – 138.

Cardona Morales, O., Alvarez Marin, D. A., and Castellanos-Dominguez, G. (2013). Outlier detection in rotating machinery under non-stationary operating conditions using dynamic features and one-class classifiers. *Dyna*, 80(182):173–181.

Cardona-Morales, O., Avendano, L., and Castellanos-Domínguez, G. (2014). Nonlinear model for condition monitoring of non-stationary vibration signals in ship driveline application. *Mechanical Systems and Signal Processing*, 44(1-2):134 – 148. Special Issue on Instantaneous Angular Speed (IAS) Processing and Angular Applications.

Cardona-Morales, O., Avendano-Valencia, L., and Castellanos-Dominguez, G. (2011). Instantaneous frequency estimation and order tracking based on Kalman filters. In *IOMAC2011 International Operational Modal Analysis Conference*.

Cha, M., Kim, J. S., and Baek, J.-G. (2014). Density weighted support vector data description. *Expert Systems with Applications*, 41(7):3343 – 3350.

Chen, J., Li, Z., Pan, J., Chen, G., Zi, Y., Yuan, J., Chen, B., and He, Z. (2016). Wavelet transform based on inner product in fault diagnosis of rotating machinery: A review. *Mechanical Systems and Signal Processing*, 70-71:1 – 35.

Cioch, W., Knapik, O., and Leśkow, J. (2013). Finding a frequency signature for a cyclostationary signal with applications to wheel bearing diagnostics. *Mechanical Systems and Signal Processing*, 38(1):55 – 64. Condition monitoring of machines in non-stationary operations.

CMMNO (2014). Cmmno'14 diagnosis contest, december 15-16, lyon-france.

Combet, F. and Zimroz, R. (2009). A new method for the estimation of the instantaneous speed relative fluctuation in a vibration signal based on the short time scale transform. *Mechanical Systems and Signal Processing*, 23(4):1382 – 1397.

Das, N., Routray, A., and Dash, P. K. (2009). A robust H_∞ learning approach to blind separation of slowly time-varying mixture of acoustic electromechanical signals. *Mechanical Systems and Signal Processing*, 23(6):2049 – 2058. Special Issue: Inverse Problems.

Das, N., Routray, A., and Dash, P. K. (2010). A robust learning approach to blind separation of signals. *Digital Signal Processing*, 20(2):410 – 416.

Ding, X., He, Q., and Luo, N. (2015). A fusion feature and its improvement based on locality preserving projections for rolling element bearing fault classification. *Journal of Sound and Vibration*, 335:367 – 383.

Feng, Z., Liang, M., and Chu, F. (2013). Recent advances in time-frequency analysis methods for machinery fault diagnosis: A review with application examples. *Mechanical Systems and Signal Processing*, 38(1):165 – 205. Condition monitoring of machines in non-stationary operations.

Fyfe, K. and Munck, E. (1997). Analysis of computed order traking. *Mechanical Systems and Signal Processing*, 11(2):187 – 205.

Gao, Y., Guo, Y., Chi, Y., and Qin, S. (2006). Order tracking based on robust peak search instantaneous frequency estimation. *Journal of physics: conferences series*, 48:479–484.

Gardner, W. A. (1990). *Introduction to random processes with applications to signals & systems*. McGraw-Hill International, second edition.

Gardner, W. A. (1994). An introduction to cyclostationary signals. *Cyclostationarity in communications and signal processing*, pages 1–90.

Gardner, W. A., Napolitano, A., and Paura, L. (2006). Cyclostationarity: Half a century of research. *Signal Processing*, 86(4):639 – 697.

Gelle, G., Colas, M., and Delaunay, G. (2000). Blind sources separation applied to rotating machines monitoring by acoustical and vibrations analysis. *Mechanical Systems and Signal Processing*, 14(3):427 – 442.

Goyal, D. and Pabla, B. (2015). The vibration monitoring methods and signal processing techniques for structural health monitoring: A review. *Archives of Computational Methods in Engineering*, pages 1–10.

Grewal, M. and Andrews, A. (2001). *Kalman filtering: Theory and practice using Matlab*. NY:Wiley,, 2nd edition.

Gryllias, K. C. and Antoniadis, I. A. (2013). Estimation of the instantaneous rotation speed using complex shifted Morlet wavelets. *Mechanical Systems and Signal Processing*, 38(1):78 – 95. Condition monitoring of machines in non-stationary operations.

Guo, Y., Chi, Y., Huang, Y., and Qin, S. (2006). Robust IFE based order analysis of rotating machinery in virtual instrument. *Journal of physics: conferences series*, 48:647–652.

Hajimolahoseini, H., Taban, M., and Abutalebi, H. (2008). Improvement of extended Kalman filter frequency tracker for nonstationary harmonic signals. In *International Symposium on Telecommunications (IST 2008)*, pages 592–597.

Hajimolahoseini, H., Taban, M. R., and Soltanian-Zadeh, H. (2012). Extended Kalman filter frequency tracker for nonstationary harmonic signals. *Measurement*, 45(1):126 – 132.

Hazan, A., Lacaille, J., and Madani, K. (2012). Extreme value statistics for vibration spectra outlier detection. In *Proceedings of CM-MFPT*. British Institute of Non-Destructive Testing.

He, W., Zi, Y., Chen, B., Wu, F., and He, Z. (2015). Automatic fault feature extraction of mechanical anomaly on induction motor bearing using ensemble super-wavelet transform. *Mechanical Systems and Signal Processing*, 54–55:457 – 480.

Heo, Y. and joon Kim, K. (2015). Definitions of non-stationary vibration power for time-frequency analysis and computational algorithms based upon harmonic wavelet transform. *Journal of Sound and Vibration*, 336:275 – 292.

Hoffmann, H. (2007). Kernel pca for novelty detection. *Pattern Recognition*, 40(3):863 – 874.

Hyvärinen, A. and Oja, E. (2000). Independent component analysis: algorithms and applications. *Neural networks*, 13(4):411–430.

Jardine, A. K., Lin, D., and Banjevic, D. (2006). A review on machinery diagnostics and prognostics implementing condition-based maintenance. *Mechanical Systems and Signal Processing*, 20(7):1483 – 1510.

Jena, D. and Panigrahi, S. (2015). Automatic gear and bearing fault localization using vibration and acoustic signals. *Applied Acoustics*, 98:20 – 33.

Jing, J. and Meng, G. (2009). A novel method for multi-fault diagnosis of rotor system. *Mechanism and Machine Theory*, 44(4):697 – 709.

Kandepu, R., Foss, B., and Imsland, L. (2008). Applying the unscented Kalman filter for nonlinear state estimation. *Journal of Process Control*.

Khan, S. and Madden, M. (2010). A survey of recent trends in one class classification. In Coyle, L. and Freyne, J., editors, *Artificial Intelligence and Cognitive Science*, volume 6206 of *Lecture Notes in Computer Science*, pages 188–197. Springer Berlin Heidelberg.

Langone, R., Alzate, C., Ketelaere, B. D., Vlasselaer, J., Meert, W., and Suykens, J. A. (2015). LS-SVM based spectral clustering and regression for predicting maintenance of industrial machines. *Engineering Applications of Artificial Intelligence*, 37:268 – 278.

Leclère, Q., André, H., and Antoni, J. (2016). A multi-order probabilistic approach for instantaneous angular speed tracking debriefing of the CMMNO14 diagnosis contest. *Mechanical Systems and Signal Processing*, pages –.

Leclère, Q. and Hamzaoui, N. (2014). Using the moving synchronous average to analyze fuzzy cyclostationary signals. *Mechanical Systems and Signal Processing*, 44(1–2):149 – 159. Special Issue on Instantaneous Angular Speed (IAS) Processing and Angular Applications.

Lei, Y., He, Z., and Zi, Y. (2008). A new approach to intelligent fault diagnosis of rotating machinery. *Expert Systems with Applications*, 35(4):1593 – 1600.

Lei, Y., Kong, D., Lin, J., and Zuo, M. J. (2012). Fault detection of planetary gearboxes using new diagnostic parameters. *Measurement Science and Technology*, 23(5):055605.

Lei, Y., Liu, Z., Wu, X., Li, N., Chen, W., and Lin, J. (2015). Health condition identification of multi-stage planetary gearboxes using a mRVM-based method. *Mechanical Systems and Signal Processing*, 60–61:289 – 300.

Lei, Y., Zuo, M., He, Z., and Zi, Y. (2010). A multidimensional hybrid intelligent method for gear fault diagnosis. *Expert Systems with Applications*, 37(2):1419 – 1430.

Liu, J., Wang, W., Golnaraghi, F., and Liu, K. (2007). Wavelet spectrum analysis for bearing fault diagnostics. *Measurement Science and Technology*, 19(1):015105.

Lu, L., Yan, J., and de Silva, C. W. (2015). Dominant feature selection for the fault diagnosis of rotary machines using modified genetic algorithm and empirical mode decomposition. *Journal of Sound and Vibration*, 344:464 – 483.

McBain, J. and Timusk, M. (2009). Fault detection in variable speed machinery: Statistical parameterization. *Journal of Sound and Vibration*, 327(3-5):623 – 646.

McBain, J. and Timusk, M. (2011). Feature extraction for novelty detection as applied to fault detection in machinery. *Pattern Recognition Letters*, 32(7):1054 – 1061.

McFadden, P. and Smith, J. (1984). Vibration monitoring of rolling element bearings by the high-frequency resonance technique — a review. *Tribology International*, 17(1):3 – 10.

Obuchowski, J., Wyłomańska, A., and Zimroz, R. (2014a). The local maxima method for enhancement of time–frequency map and its application to local damage detection in rotating machines. *Mechanical Systems and Signal Processing*, 46(2):389 – 405.

Obuchowski, J., Wyłomańska, A., and Zimroz, R. (2014b). Selection of informative frequency band in local damage detection in rotating machinery. *Mechanical Systems and Signal Processing*, 48(1–2):138 – 152.

Olson, D. L. and Delen, D. (2008). *Advanced data mining techniques*. Springer Science & Business Media.

Pan, M. and Lin, Y. (2006). Further exploration of Vold-Kalman filtering order tracking with shaft-speed information-(i) theoretical part, numerical implementation and parameter investigations. *Mechanical systems and signal processing*, 20.

Pan, M. and Wu, C. (2007). Adaptive Vold-Kalman filtering order tracking. *Mechanical systems and signal processing*, 21.

Pan, Y., Chen, J., and Li, X. (2010). Bearing performance degradation assessment based on lifting wavelet packet decomposition and fuzzy c-means. *Mechanical Systems and Signal Processing*, 24(2):559 – 566.

Peled, R., Braun, S., and Zacksenhouse, M. (2005). A blind deconvolution separation of multiple sources, with application to bearing diagnostics. *Mechanical Systems and Signal Processing*, 19(6):1181 – 1195. Special Issue: Blind Source Separation.

Pimentel, M. A., Clifton, D. A., Clifton, L., and Tarassenko, L. (2014). A review of novelty detection. *Signal Processing*, 99:215 – 249.

Popescu, T. D. (2010). Blind separation of vibration signals and source change detection – application to machine monitoring. *Applied Mathematical Modelling*, 34(11):3408 – 3421.

Potter, R. (1990). A new order tracking method for rotating machinery. *Sound and Vibration*, 24(9):30–34.

Powers, D. M. (2011). Evaluation: from precision, recall and F-measure to ROC, informedness, markedness and correlation. *Journal of Machine Learning Technologies*, 2(1):37–63.

Randall, R., Antoni, J., and Chobsaard, S. (2001). The relationship between spectral correlation and envelope analysis in the diagnostics of bearing faults and other cyclostationary machine signals. *Mechanical Systems and Signal Processing*, 15(5):945 – 962.

Randall, R. B. (2011). *Vibration-based condition monitoring: industrial, aerospace and automotive applications*. John Wiley & Sons.

Randall, R. B. and Antoni, J. (2011). Rolling element bearing diagnostics—a tutorial. *Mechanical Systems and Signal Processing*, 25(2):485 – 520.

Renaudin, L., Bonnardot, F., Musy, O., Doray, J., and Rémond, D. (2010). Natural roller bearing fault detection by angular measurement of true instantaneous angular speed. *Mechanical Systems and Signal Processing*, 24(7):1998 – 2011. Special Issue: {ISMA} 2010.

Rodopoulos, K., Yiakopoulos, C., and Antoniadis, I. (2014). A parametric approach for the estimation of the instantaneous speed of rotating machinery. *Mechanical Systems and Signal Processing*, 44(1–2):31 – 46. Special Issue on Instantaneous Angular Speed (IAS) Processing and Angular Applications.

SAFRAN (2015). Safran contest, conference surveillance 8, october 20-21, roanne-france.

Scala, B. L. and Bitmead, R. (1994). Design of an extended Kalman filter frequency tracker. *IEEE trans. Signal processing*, 44.

Sejdic, E., Djurovic, I., and Jiang, J. (2009). Time-frequency feature representation using energy concentration: An overview of recent advances. *Digital Signal Processing*, 19(1):153 – 183.

Servière, C. and Fabry, P. (2005). Principal component analysis and blind source separation of modulated sources for electro-mechanical systems diagnostic. *Mechanical systems and signal processing*, 19(6):1293–1311.

Servière, C. and Fabry, P. (2004). Blind source separation of noisy harmonic signals for rotating machine diagnosis. *Journal of Sound and Vibration*, 272(1–2):317 – 339.

Sierra-Alonso, E. F., Cardona-Morales, O., Acosta-Medina, C. D., and Castellanos-Dominguez, G. (2014). *Progress in Pattern Recognition, Image Analysis, Computer Vision, and Applications: 19th Iberoamerican Congress, CIARP 2014, Puerto Vallarta, Mexico, November 2-5, 2014. Proceedings*, chapter Spectral Correlation Measure for Selecting Intrinsic Mode Functions, pages 231–238. Springer International Publishing, Cham.

Simon, D. and Chia, T. (2002). Kalman filtering with state equality constraints. *IEEE Transactions on Aerospace and Electronic Systems*, 38:128–136.

Smith, W. A. and Randall, R. B. (2015). Rolling element bearing diagnostics using the case western reserve university data: A benchmark study. *Mechanical Systems and Signal Processing*, 64–65:100 – 131.

Stephens, D. B. and Vold, H. (2014). Order tracking signal processing for open rotor acoustics. *Journal of Sound and Vibration*, 333(16):3818 – 3830.

Tan, A. C. C., Karimi, M., and Mathew, J. (2006). *Engineering Asset Management: Proceedings of the 1st World Congress on Engineering Asset Management (WCEAM) 11 – 14 July 2006*, chapter Blind Deconvolution using the Eigenvector Algorithm (EVA) Method for the Enhancement of Bearing Signal Through the Transmission Channel, pages 198–205. Springer London, London.

Tax, D. (2011). *One-class classification*. PhD thesis, Delft University of Technology.

Tax, D. and Juszczak, P. (2002). Kernel whitening for one-class classification. In Lee, S.-W. and Verri, A., editors, *Pattern Recognition with Support Vector Machines*, volume 2388 of *Lecture Notes in Computer Science*, pages 855–873. Springer Berlin / Heidelberg.

Tax, D. M. J. and Duin, R. P. W. (2004). Support vector data description. *Machine Learning*, 54(1):45–66.

Taylor, J. (1994). *The vibration analysis handbook*. Vibration Consultants.

Tse, P., Gontarz, S., and Wang, X. (2007). Enhanced eigenvector algorithm for recovering multiple sources of vibration signals in machine fault diagnosis. *Mechanical Systems and Signal Processing*, 21(7):2794 – 2813.

Ungarala, S., Dolence, E., and Li, K. (2007). Constrained extended Kalman filter for nonlinear state estimation. In *8th International IFAC Symposium on Dynamics and Control Process Systems, Cancun - Mexico*, volume 2, pages 63–68.

Urbanek, J., Barszcz, T., and Antoni, J. (2013). A two-step procedure for estimation of instantaneous rotational speed with large fluctuations. *Mechanical Systems and Signal Processing*, 38(1):96 – 102. Condition monitoring of machines in non-stationary operations.

Villa, L. F., nones, A. R., Perán, J. R., and de Miguel, L. J. (2012). Statistical fault diagnosis based on vibration analysis for gear test-bench under non-stationary conditions of speed and load. *Mechanical Systems and Signal Processing*, 29(0):436 – 446.

Wang, D. (2016). K-nearest neighbors based methods for identification of different gear crack levels under different motor speeds and loads: Revisited. *Mechanical Systems and Signal Processing*, 70-71:201 – 208.

Wang, D. and Tse, P. W. (2012). A new blind fault component separation algorithm for a single-channel mechanical signal mixture. *Journal of Sound and Vibration*, 331(22):4956 – 4970.

Wang, K. and Heyns, P. (2011). Application of computed order tracking, Vold-Kalman filtering and EMD in rotating machine vibration. *Mechanical Systems and Signal Processing*, 25(1):416 – 430.

Wang, S., Huang, W., and Zhu, Z. (2011a). Transient modeling and parameter identification based on wavelet and correlation filtering for rotating machine fault diagnosis. *Mechanical Systems and Signal Processing*, 25(4):1299 – 1320.

Wang, Y. and Liang, M. (2012). Identification of multiple transient faults based on the adaptive spectral kurtosis method. *Journal of Sound and Vibration*, 331(2):470 – 486.

Wang, Y., Xiang, J., Mo, Q., and He, S. (2015). Compressed sparse time-frequency feature representation via compressive sensing and its applications in fault diagnosis. *Measurement*, 68:70 – 81.

Wang, Z., Chen, J., Dong, G., and Zhou, Y. (2011b). Constrained independent component analysis and its application to machine fault diagnosis. *Mechanical Systems and Signal Processing*, 25(7):2501–2512.

Worden, K., Staszewski, W. J., and Hensman, J. J. (2011). Natural computing for mechanical systems research: A tutorial overview. *Mechanical Systems and Signal Processing*, 25(1):4 – 111.

Xiao, Y., Wang, H., Xu, W., and Zhou, J. (2013). L1 norm based KPCA for novelty detection. *Pattern Recognition*, 46(1):389 – 396.

Yang, Y. and Nagarajaiah, S. (2014). Blind identification of damage in time-varying systems using independent component analysis with wavelet transform. *mechanical systems and signal processing*, 47(1):3–20.

Ypma, A., Leshem, A., and Duin, R. P. (2002). Blind separation of rotating machine sources: bilinear forms and convolutive mixtures. *Neurocomputing*, 49(1–4):349 – 368.

Zhang, Y., Liu, X.-D., Xie, F.-D., and Li, K.-Q. (2009). Fault classifier of rotating machinery based on weighted support vector data description. *Expert Systems with Applications*, 36(4):7928 – 7932.

Zhang, Z., Chan, S.-C., and Tsui, K. M. (2008). A recursive frequency estimator using linear prediction and a Kalman-filter-based iterative algorithm. *Circuits and Systems II: Express Briefs, IEEE Transactions on*, 55(6):576–580.

Zhao, X., Kong, Q., and Guo, Q. (2008). Study of time-frequency order tracking of vibration signals of rotating machinery in changing state. *IEEE computer society*.

Zhou, H., Chen, J., Dong, G., and Wang, R. (2015). Detection and diagnosis of bearing faults using shift-invariant dictionary learning and hidden Markov model. *Mechanical Systems and Signal Processing*, pages –.

Zimroz, R., Urbanek, J., Barszcz, T., Bartelmus, W., Millioz, F., and Martin, N. (2011). Measurement of instantaneous shaft speed by advanced vibration signal processing-application to wind turbine gearbox. *Metrology and Measurement Systems*, 18(4):701–712.